AER/AGS Special Report 122

Alberta Energy Regulator

Airborne Geophysics Data Analysis and Interpretation, Northern Alberta

AGS
ALBERTA GEOLOGICAL SURVEY

AER/AGS Special Report 122

Airborne Geophysics Data Analysis and Interpretation, Northern Alberta

G.P. Lopez, A. Brem, D. McGill and J. McKenzie

Ronacher McKenzie Geoscience Inc.

December 2024

ISBN 978-1-4601-5723-7

Lopez, G.P., Brem, A., McGill, D. and McKenzie, J. (2024): Airborne geophysics data analysis and interpretation, northern Alberta; Alberta Energy Regulator / Alberta Geological Survey, AER/AGS Special Report 122, 153 p.

Authors address:
G.P. Lopez, A. Brem, D. McGill and J. McKenzie
Ronacher McKenzie Geoscience Inc.
6 – 2140 Regent Street
Sudbury, ON P3E 5S8
Canada

Tel: 705.419.1508
Email: info@rmgeoscience.com

Published December 2024 by:
Alberta Energy Regulator
Alberta Geological Survey
Suite 205
4999 – 98 Avenue NW
Edmonton, AB T6B 2X3
Canada

Tel: 780.638.4491
Email: AGS-Info@aer.ca
Website: ags.aer.ca

Contents

Appendices

Digital Appendix A – Interpretation – GIS files

The appendix is in the accompanying folder entitled 'Digital Appendix A – Interpretation – GIS files', located in the download zip file.

Digital Appendix B – Airborne magnetic and gravity map products

The appendix is in the accompanying folder entitled 'Digital Appendix B – Airborne magnetic and gravity map products', located in the download zip file.

Digital Appendix C – Automatic Detection – Fathom Geophysics – vector and raster products

The appendix is in the accompanying folder entitled 'Digital Appendix C – Automatic Detection – Fathom Geophysics', located in the download zip file.

Foreword

The Alberta Geological Survey (AGS) outsourced the geological interpretation of the 2021 to 2023 high-resolution airborne magnetic and gravity surveys conducted by the Alberta Energy Regulator (AER) / AGS in northern Alberta. This interpretation focused on modifying the boundaries of basement domains, dividing known domains into subdomains, distinguishing anomalies in the basement (intrusions, ductile structures, brittle faults, etc.), identifying late brittle faults in the Western Canada Sedimentary Basin (WCSB), and correlating geophysical anomalies with kimberlite pipes. Although this report does not identify any specific mineral occurrences, critical mineral potential is discussed and several potential controls on mineralization are suggested for various commodities (zinc, uranium, etc.).

All production of geophysical products and interpretation of data was conducted by Ronacher McKenzie Geoscience Inc. (RMG), as well as subcontractor Fathom Geophysics LLC, with oversight and approval by the AER and AGS. Using the 2021 to 2023 aeromagnetic and gravity data, RMG synthesized a selection of grid-based filter products to aid subsequent interpretation. Additionally, RMG commissioned Fathom Geophysics LLC to produce automatic structure and radial symmetry detection filters, and other geophysical products. By integrating this new information with existing geological data, the authors' interpretation included modifications to basement domain boundaries and, notably, division of known basement domains into smaller subdomains. In addition, the authors identified possible intrusions and ductile structures in the basement and delineated brittle faults and kimberlite pipes. Subsequently, a compilation map and report were produced by RMG to highlight all new geological interpretations in northern Alberta. RMG also included an array of new GIS and geophysical products in their deliverables.

This work was completed under the Mineral Grant provided by the Government of Alberta dated June 22, 2021.

Geological Interpretation of the 2021-2022 Aeromagnetic Data

Northern Alberta

Prepared For:

Alberta Geological Survey

Prepared By:

Gloria Lopez, PhD, P.Geo.
Arjan Brem, PhD, P.Geo.
Darcy McGill, P.L. (Geo.)
Jenna McKenzie, P.Geo.
Ronacher McKenzie Geoscience Inc.

29 March 2024

TABLE OF CONTENTS

FIGURES

TABLES

APPENDICES

DIGITAL APPENDICES

1.0 SUMMARY

The Alberta Geological Survey ("AGS") contracted Ronacher McKenzie Geoscience ("RMG") to provide a geological interpretation of the 2021-2022 high-resolution aeromagnetic and gravity surveys conducted over northern Alberta.

This report presents the results of the geological interpretation, which includes the northern Alberta basement and the overlying Western Canada Sedimentary Basin ("WCSB"). This report supplements the GIS files produced for this project.

The Alberta Energy Regulator ("AER") contracted EON Geosciences Inc., Sander Geophysics Ltd., and Xcalibur Multiphysics to fly aeromagnetic and gravity surveys covering the project area. RMG reviewed the digital data for completeness and data quality. Additional aeromagnetic data from legacy surveys were acquired to complete coverage of the Northern Alberta project area.

The new airborne magnetic and gravity data and derivative products enable improved understanding of the 3D architecture of the basement in northern Alberta. The observations were integrated with and calibrated against existing results of legacy geophysical studies, geological information, and regional structural interpretations. Care was taken to avoid mistaking potential cultural magnetic response for geology-related anomalies. The following conclusions can be made:

- Modifications to basement domains were made by editing tectonic domain boundaries of Ross et al (1994) and Pilkington et al. (2000) and by dividing known domains into subdomains.
- Basement anomalies potentially caused by intrusions were delineated. These range from small single lobe circular anomalies to larger multi-lobe rounded asymmetrical anomalies.
- Known ductile structures were recognized and new ductile structures were identified.
- New brittle faults were delineated in the basement and WCSB. Few faults of the WCSB reported in the literature show a spatial correlation with the magnetic and gravity lineaments.
- The axis of the Peace River Arch coincides with changes in direction of magnetic fabric observed in most subdomains that possibly relates to the original geometry of the continental margin. Therefore, the rise of the Peace River Arch relates to a basement feature.
- Overall, the known kimberlite fields are aligned perpendicular to the curvature of the magnetic fabric that dominates the south-central part of the project area.
- The Buffalo Head Hills kimberlite field is spatially related to a complex suite of overlapping features, including N- and NNW-trending faults, and a N-trending subdomain of variable magnetic fabric with evidence of remanence along the contact between Buffalo High and Buffalo Utikuma subdomains. The Birch Mountains kimberlite field is spatially related to a NW-trending basement fault crosscutting the sheared Taltson Athabasca subdomain. The Mountain Lake intrusions do not clearly show a relation with major structures in the Chinchaga terrane.

- A number of eighteen known kimberlites can be positively identified in the magnetic data as high-frequency circular anomalies. However, most of high frequency anomalies are related to culture and these cannot be used to infer kimberlites. Given the small size of Alberta kimberlites and abundant cultural footprint in the region, a higher resolution magnetic survey and correlation with datasets of infrastructure and imagery are needed to conduct kimberlite detection.
- A relationship between lithotectonic elements and mineral occurrences is proposed for helium, lithium, uranium and zinc.

The interpretation of the new high-quality aeromagnetic data for Northern Alberta resulted in corroboration of previous lithotectonic domains defined by previous authors, and facilitated the identification of new subdomains and structural lineaments that may help to refine current tectonic models. The interpretation also included the identification of equant or rounded anomalies of variable radius, and some larger rounded bodies that may correspond to intrusions. Kimberlite fields were correlated with new interpreted basement structure and trends. The interpretation of gravity survey data combined with aeromagnetic data resulted in the identification of brittle structures and some shallow lineaments that correlate with erosional edges of Cretaceous strata.

2.0 PROJECT OVERVIEW

The Alberta Geological Survey ("AGS") commissioned Ronacher McKenzie Geoscience ("RMG") to complete a geological interpretation of the 2021-2022 high-resolution aeromagnetic and gravity surveys over northern Alberta ("NAB") conducted by EON Geosciences Inc., Sander Geophysics Ltd., and Xcalibur Multiphysics with the following regional objectives:

- Define domains for regional tectonic interpretations of the crystalline basement (Western Laurentia).
- Delineate anomalies from granitoids to ductile structures in the basement.
- Examine delineated anomalies for correlation with known kimberlite fields to determine if similar anomalies could be used predictively for kimberlite detection, considering that detection is subject to the limitations of the acquisition parameters under which individual small intrusions may not be resolvable.
- Examine linear anomalies and lineament bands for correlation with brittle fracture zones such as the Hay River Fault and for alignment of kimberlites, whose locations are sometimes suspected to follow lithospheric zones of weakness.
- Identify late brittle faults that may have acted as pathways for fluids (e.g., helium, mineralizing fluids) or hydrocarbon traps.
- Integrate the airborne geophysical data within western Canada geophysical database and regional tectonic interpretation.

RMG completed parallel studies on geophysical data from the Canadian Shield (Lopez et al., 2024) and southern Alberta (Brem et al., 2024).

Universal Transverse Mercator ("UTM") coordinates were provided in the datum of WGS 84 zone 11N for all aeromagnetic digital files (vector and map files). Figures herein were projected to NAD 83 zone 11N.

2.1 Previous Regional Studies

Previous regional studies that involve geophysical acquisition and/or geological interpretations include:

- The pioneering work by Hoffmann (1988), Ross et al. (1989), and Villeneuve et al. (1993), in which aeromagnetic and gravity data were used to subdivide the basement in Alberta into tectonic domains.
- Burwash et al. (1994) provided geological interpretation of the basement rocks based on petrography, whole-rock geochemistry, and isotopic age determinations carried out on samples collected from oil and gas well cores that had penetrated the basement. Later this author provided a metamorphic evolution of the basement of Alberta based on historical and new U–Pb, Rb–Sr, K–Ar, $^{40}Ar/^{39}Ar$ and Sm–Nd geochronology (Burwash et al., 2000).
- Lithoprobe was a national research project that studied the 3D structure and evolution of the subsurface in Canada. Lithoprobe data for northern Alberta can be found in Eaton et al. (1995; 1999) and Ross and Eaton (2002), among others.
- Pilkington et al. (2000) used quantitative and anomaly enhancement methods to emphasize the internal character of domains and refined the basement subdivisions.
- Lyatsky et al. (2005; and references therein) used aeromagnetic and gravity data and applied quantitative methods to identify lineaments in central and southern Alberta. This work supported the conclusions by Eaton et al. (1995) that basement faults have a control on hydrocarbon traps in the Central Alberta basin.
- McKenzie et al. (2021) completed a regional interpretation of geophysical data for the Peace River Arch and southern Alberta areas as part of a helium and lithium prospectivity project by the AGS.

2.2 Recent Advances

Over the past two decades, advances in computing power have enabled new geophysical data processing methods and visualization techniques, particularly for large scale datasets, that would have been previously impossible to process, display, model and interpret. In addition, 3D integration and modelling of subsurface data is now commonplace, enabled by these same computing advances.

New state-of-the-art aeromagnetic and gravity surveys allow better and more accurate analysis and interpretation of the data, particularly since much of the legacy aeromagnetic and gravity data was acquired using very large line spacings and without the spatial accuracy made possible by satellite positioning and navigation systems.

2.3 RMG Qualifications

RMG is an international consulting company with offices in Toronto and Sudbury, Ontario, Canada. RMG's mission is to use intelligent geoscientific data integration to help mineral explorers focus on what matters to them. We help a growing number of clients understand the factors that control the location of mineral deposits.

With a variety of professional experience, our team's services include:

- Data Integration, Analysis, and Interpretation
- Geophysical Services
- Project Generation and Property Assessment
- Exploration Project Management
- Independent Technical Reporting
- Project Promotion
- Lands Management

The primary author of this report is Gloria Lopez, PhD, P.Geo., Senior Geologist at RMG and a geologist in good standing with the Association of Professional Engineers and Geoscientists of Alberta (#181673) and Professional Engineers and Geoscientists Newfoundland and Labrador (#11213). Dr. Lopez has over two decades of experience working as an economic geologist.

Co-author of this report is Mr. Darcy McGill, BSc, P.Geo. (Limited), P.L. (Geo). Mr. McGill is a Senior Geophysicist at RMG and a geophysicist in good standing with the Association of Professional Geoscientists of Ontario (APGO #2010 and Professional Licensee with the Association of Professional Engineers and Geoscientists of Alberta (#316505). Mr. McGill has worked in geophysical data acquisition, processing, and interpretation for mineral exploration since 1995.

A second co-author of this report is Arjan Brem, PhD, P.Geo., Associate Geologist at RMG and a geoscientist in good standing with the Association of Professional Geoscientists of Ontario (#3798) and with the Association of Professional Engineers and Geoscientists of Alberta (#289121). Dr. Brem has worked globally as a structural geologist in the petroleum industry since 2007.

A third co-author of this Report is Ms. Jenna McKenzie, Hons BSc, P.Geo. Ms. McKenzie is co-founder and Principal Geophysicist to RMG and a geoscientist in good standing with the Association of Professional Geoscientists of Ontario (APGO #1653) and the Association of Professional Engineers and Geoscientists of Alberta (#315719). Ms. McKenzie has worked as a geophysicist since 2001 in the exploration and mining industry on a variety of exploration properties with specific focus on geophysics surveying and interpretation.

Additionally, Fathom Geophysics completed the automatic structure, depth to basement and radial symmetry for intrusion detection on behalf of RMG.

3.0 PROJECT LOCATION

The project area is located in northern Alberta, adjoining British Columbia, Saskatchewan and the Northwest Territories (Figure 3-1). The survey area lies between latitudes 54° and 60'N, and longitudes 110° and 120'W, and is covered by NTS map sheets 73L, 73M, 74D, 74E, 74L, 74M, 83I, 83J, 83K, 83M to 83P, and 84A to 84P.

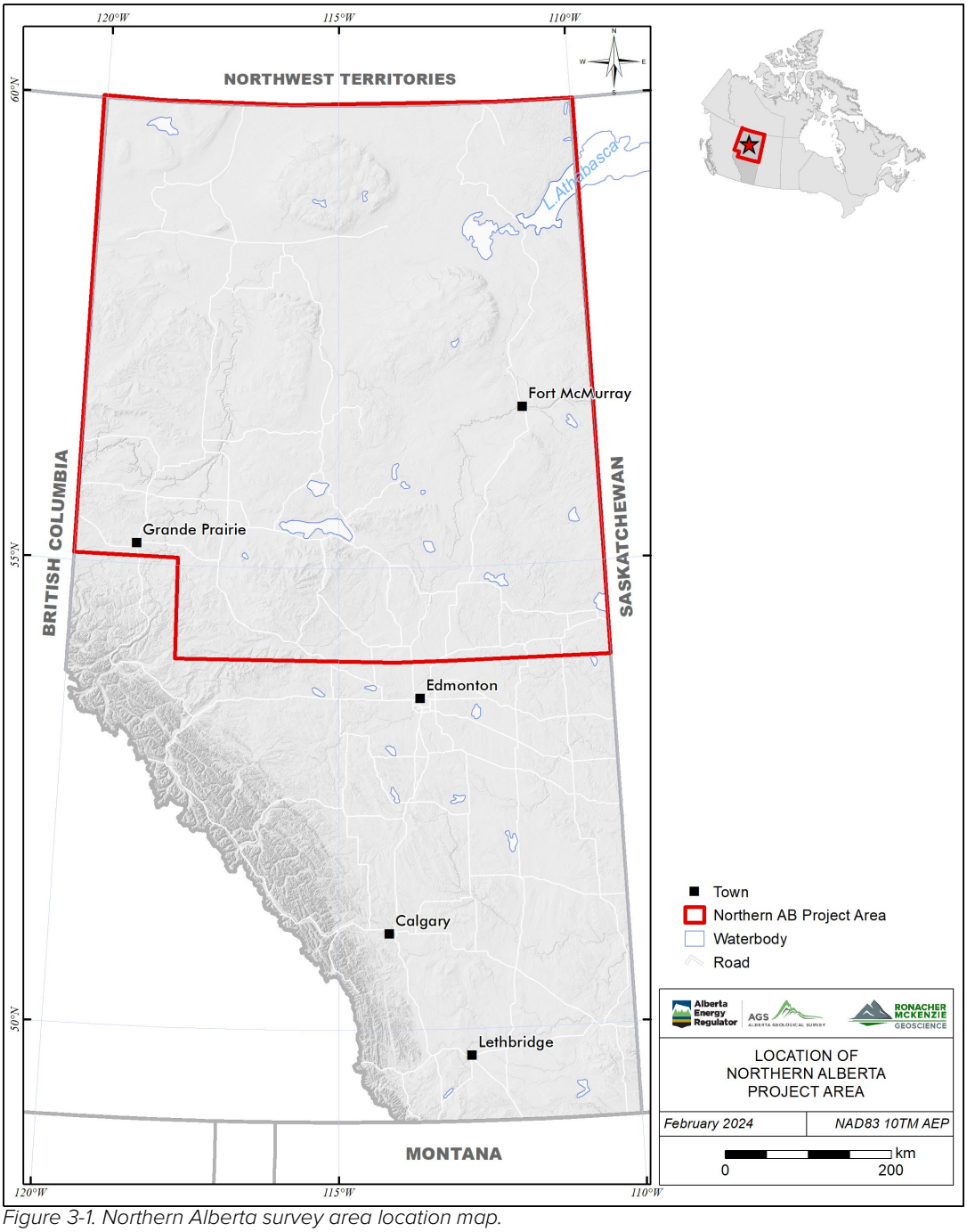

Figure 3-1. Northern Alberta survey area location map.

4.0 GEOLOGICAL SETTING

The northern Alberta project area encompasses the Northern Plains, plus the northern part of the Central Plains, as well as the Canadian Shield and the Athabasca Basin in the northeast corner of the province (Prior et al., 2013). Beneath the Northern and Central Plains, the Archean to Proterozoic crystalline basement is overlain by the Middle Cambrian to Cenozoic sedimentary succession of the Western Canada Sedimentary Basin (Figure 4-1). In addition, clusters of mafic to ultramafic igneous rocks, including kimberlites, occur in the Northern Plains.

4.1 Crystalline Basement

Crystalline basement in Alberta is comprised of Archean and Paleoproterozoic terranes (Figure 4-2) that were assembled into Laurentia during the Paleoproterozoic (e.g., Hoffmann, 1988; Villeneuve et al., 1993; Ross et al., 1994). The most recent definition of tectonic domains by Pilkington et al. (2000) used automated interpretation methods on magnetic and gravity data available at that time to map outlines of magnetic sources and to characterize the internal structure of the domains. In the project area, Pilkington's domains are: Hottah, Great Bear, Nova, Kiskatinaw, Ksituan, Chinchaga, Buffalo High, Buffalo Utikuma, Thorsby, Wabamun, Rimbey, Loverna, and Rae (Figure 4-3).

Lithological and geochronological controls on basement rocks are based on exposed units in the Canadian Shield and on core samples from oil and gas wells in the Northern Plains, which were compiled by Villeneuve et al. (1993) and Burwash et al. (1994) (Figure 4-1). Further characterization of the crustal architecture in 3D has benefitted from integration with Lithoprobe deep seismic reflection studies (e.g., Eaton et al., 1999; Ross and Eaton, 2002). Lastly, the Precambrian basement top picks and modeled basement topography surface are available from the AGS (Branscombe, 2017; Hauck and Corlett, 2017).

Major structural features of the basement of northern Alberta are the Great Slave Lake Shear Zone ("GSLSZ") in the northwest of the project area, the Charles Lake, Leland Lakes and Beatty River shear zones in the northeast, and the Snowbird Tectonic Zone ("STZ") in the southeast (Figure 4-3).

The GSLSZ is a major NE-trending Proterozoic tectonic element present in the northwestern corner of the project area (Figure 4-2, Figure 4-3). It is a distinct aeromagnetic lineament that extends more than 1000 km from Northwest Territories through Alberta into British Columbia (Hoffmann, 1988; Ross et al., 1994). The GSLSZ outcrops as a 25 km wide deformation zone in the Great Slave Lake area where it has been mapped and studied, however based on analysis of the geophysical data in the subsurface some authors have considered it as wide as 50-100 km (e.g., Davies et al., 2018; and references therein). The GSLSZ is interpreted as a continental transcurrent boundary which formed during the oblique convergence of the Archean Rae and Slave provinces accommodating up to 700 km of dextral ductile shearing, spanning ca. 1920–1740 Ma (e.g., Šilerová et al., 2023). The McDonald Fault mapped in the Great Slave area, NWT, is the northern boundary of GSLSZ separating less deformed rocks from ultramylonites (Cutts et al., 2022), and the Hay River Fault is its extension to the southwest into Alberta (Pană et al., 2021). However, this last distinction between GSLSZ, McDonald and Hay River Faults is not well established for northern Alberta as ambiguity among publicly

available reports exists. In this report, we refer to the GSLSZ as the main name of the shear zone, including all fault branches and deformed rocks, whereas the Hay River Fault is considered to represent the northern branch of the GSLSZ.

The Charles Lake Shear Zone consists of a NNE to N-trending system of anastomosing subvertical splays of mylonites, known as Goldschmidt Lake, Mercredi Lake, Charles Lake and Bayonet Lake shear zones, in the Taltson Magmatic Zone (McDonough et al., 2000; Pană, 2007).

The Leland Lakes Shear Zone consists of a NE to N-trending system of two parallel subvertical mylonitic zones in the Taltson Magmatic Zone.

The Beatty River Shear Zone or Beatty River Fault is an SW-trending shear zone in Saskatchewan that extends into Alberta south of the Athabasca Basin (e.g., Ramaekers, 2004; Post, 2004).

The STZ separates the Archean Rae and Hearne cratons of the Canadian Shield and has been interpreted either as an Archean or Paleoproterozoic intracontinental transform or as a Paleoproterozoic suture zone (Hoffmann, 1988). Pană et al. (2021; Figure 4-3) outlined the STZ as a main NE-trending shear zone in the Thorsby Domain, plus a northern splay separating Wabamun from Buffalo High and Chinchaga domains.

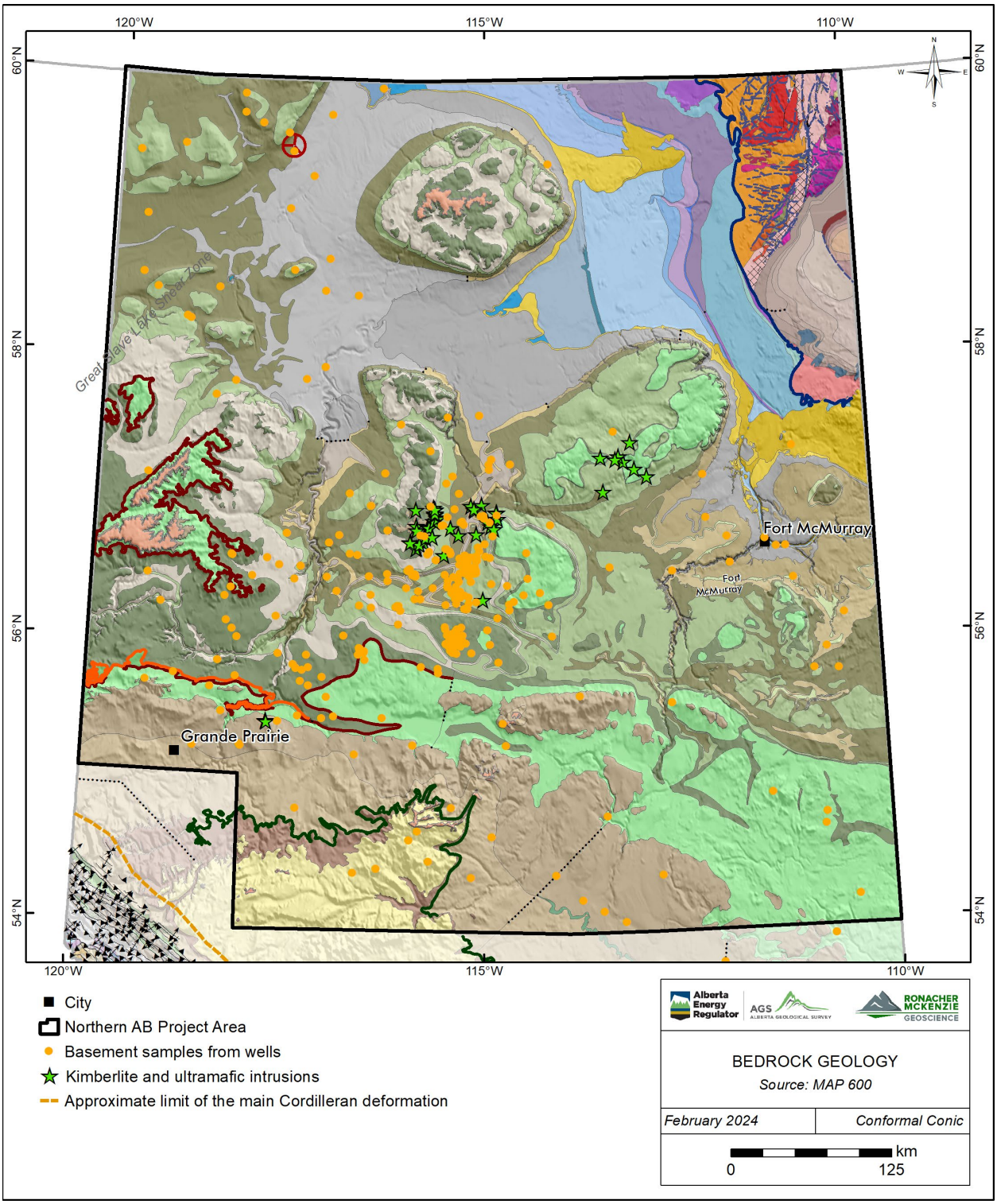

Figure 4-1. Geological map of northern Alberta (from Prior et al., 2013).

Figure 4-1b: Legend of Figure 4-1.

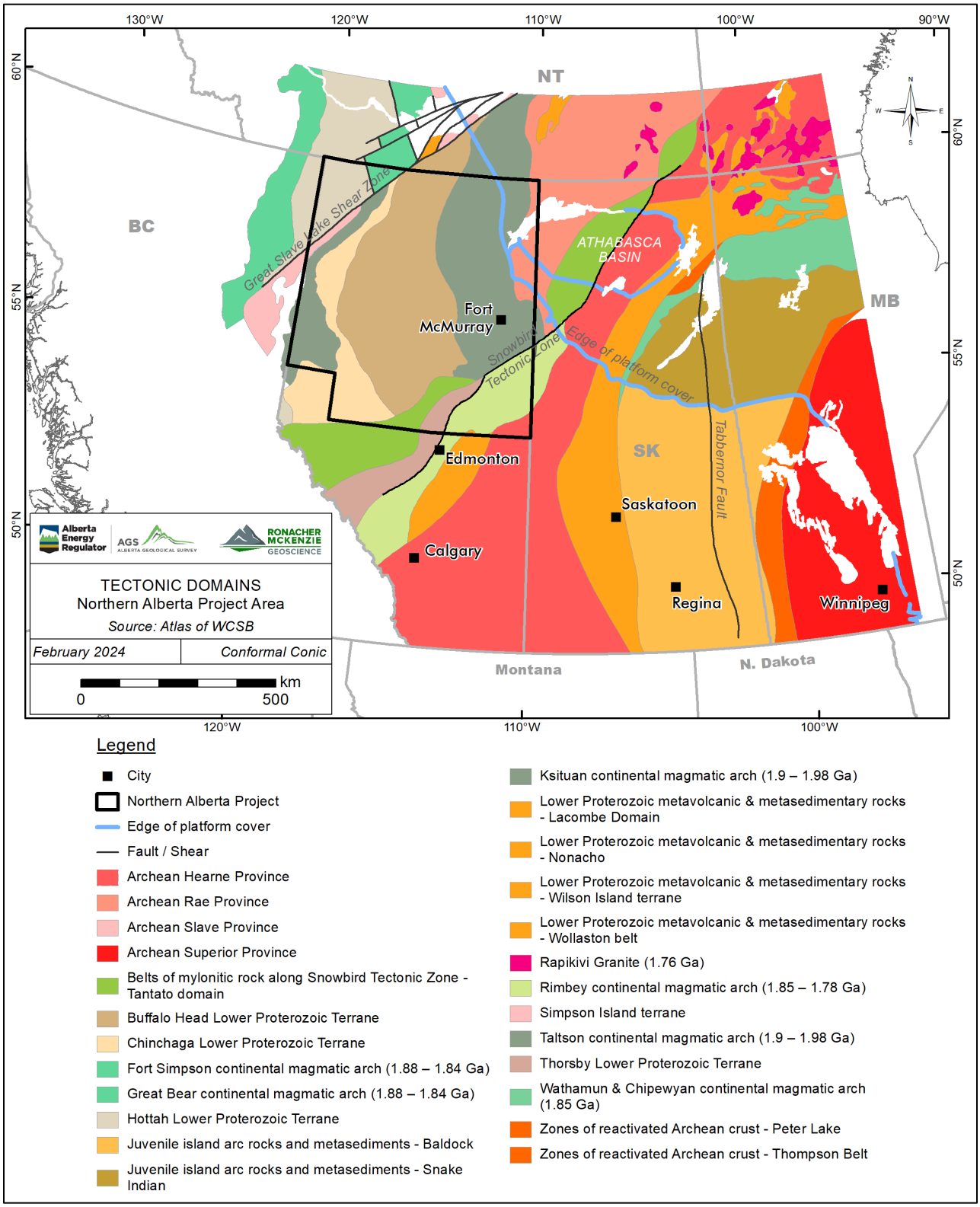

Figure 4-2. Tectonic domains in Western Canada (modified from Ross et al., 1994).

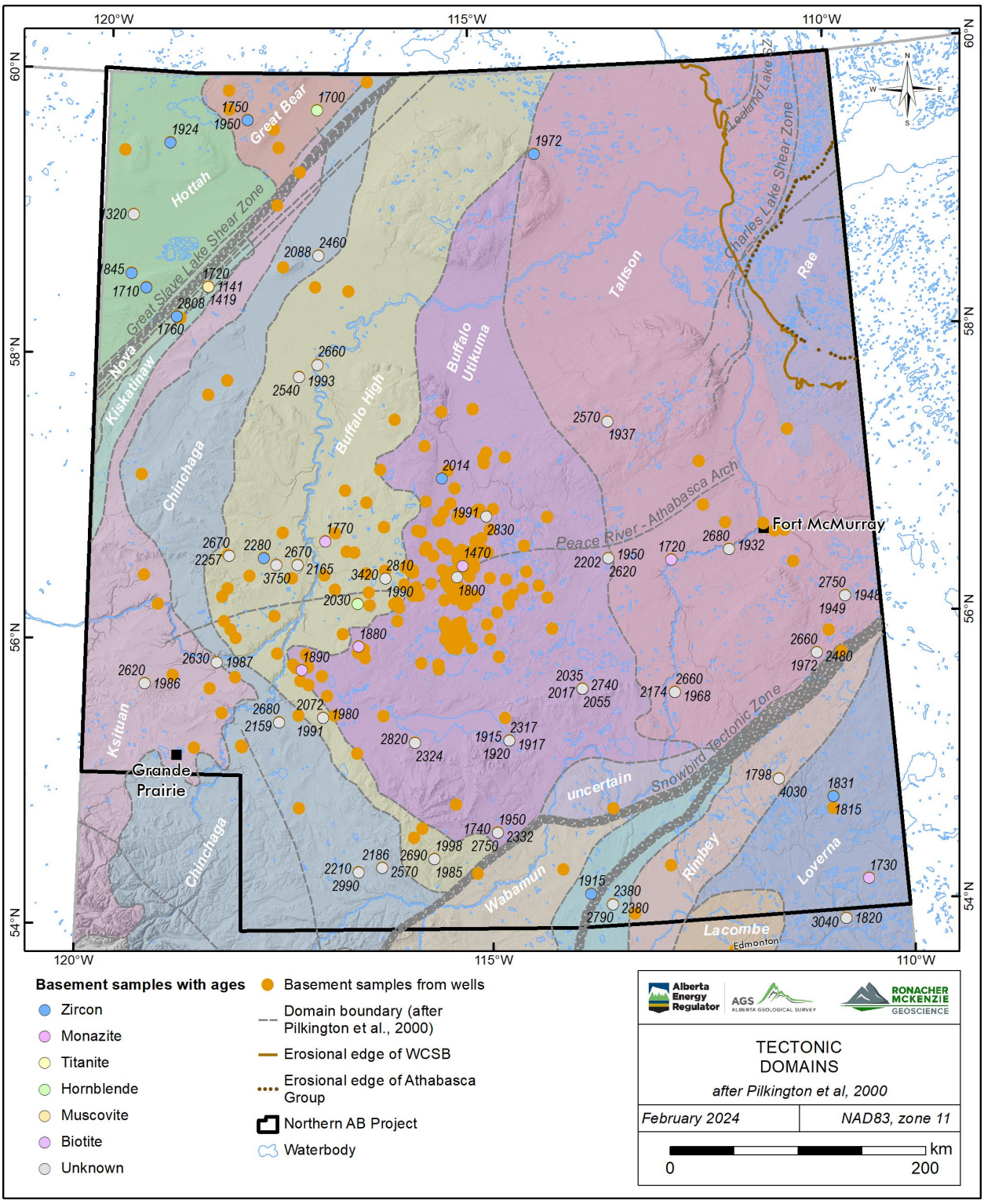

Figure 4-3 Tectonic domains of northern Alberta after Pilkington et al. (2000). Selected structural lineaments from Pană et al (2021). Radiometric ages from Ross et al. (1991), Villeneuve et al. (1993), and Burwash et al (unpublished data 1994).

4.2 Athabasca Basin

About ten percent of the western Athabasca Basin is present in northeastern Alberta, overlying the Taltson Magmatic Zone ("Taltson") and possibly the Rae Craton (Figure 4-2). The late Paleoproterozoic to early Mesoproterozoic (ca. 1760 Ma and 1500 Ma) Athabasca Group comprises four quartzose fluvial sequences, bounded by unconformities, and deposited in distinct stacked NE-trending sub-basins with a total preserved aggregate thickness estimated at 1150 m (e.g., Ramaekers et al., 2007). Descriptions of Athabasca Group units in Alberta can be found in Post (2004) and Pană and Olson (2009).

Major structural features in the Athabasca Basin of Alberta include the Charles Lake Shear Zone, which bounds the basin along its the western edge, and the Black Bay Fault a basement shear zone that may have controlled the formation of the Black Bay Trough. Other interpreted faults, troughs, and highs as well as internal features of the basin strata are described in Ramaekers et al., (2007).

4.3 Western Canada Sedimentary Basin

In Alberta, the basement is covered by the Phanerozoic Western Canada Sedimentary Basin ("WCSB"). The thickness of the sedimentary strata increases towards the Rocky Mountains, from its erosional edge in the northeast in the Canadian Shield region to a maximum of approximately 6 km in the west.

In the project area, the WCSB stratigraphy reflects deposition in two different tectonic settings (Mossop and Shetsen, 1994).

- Cambrian to Middle Jurassic passive continental margin, dominated by carbonates, mudstones and minor evaporites; and
- Middle Jurassic to Oligocene foreland basin dominated by clastic sequences.

The WCSB deposition was controlled by the presence and reactivation of the cratonic Tathlina Arch (located in the Northwest Territories) and the Peace River Arch (located in Alberta).

The Peace River Arch ("PRA"), also named Peace River – Athabasca Arch, is an east-northeasterly trending subsurface structure that developed perpendicular to the western edge of the North American craton along the lower Paleozoic passive margin. The PRA has a history of uplift during the Neoproterozoic through the Devonian and subsidence from the Late Devonian to the Cretaceous. Uplift, onlap and burial resulted in the formation of unconformities and influenced the distribution of Cambrian and Devonian siliciclastic and carbonate sediments around the arch. Later subsidence resulted in the formation of the Dawson Creek Graben Complex, which includes a group of horsts and grabens with bounding faults such as the Tangent and Dunvegan faults. Fracture-associated hydrothermal karst and dolomitization in WCSB strata occurred in the vicinity of the PRA. Such structures have been mapped using downhole geophysical well logs and seismic sections.

The Hay River Fault is spatially coincident with the GSLSZ and has been described as the southern extension of the McDonald Fault in NWT. The Hay River Fault has been reported as active during the Phanerozoic,

controlling Devonian and Cretaceous strata deposition (Wright et al., 1994; Davies et al., 2018). There is ambiguity between public reports on the definition and timing of the Hay River Fault; the names Hay River, McDonald and Great Slave Lake appear to be used interchangeably.

Other localized structures in the WCSB include astroblemes, the (eroded) remnants of meteorite impact craters. In northern Alberta, these include the Steen River astrobleme (Molak et al., 2001; Walton et al., 2017; McGregor et al., 2020) and the Hotchkiss astrobleme (Mazur, 1999).

4.4 Kimberlite Fields

Two kimberlite fields and an ultrabasic intrusion are known in Alberta: Mountain Lake, Buffalo Head Hills, and Birch Mountains (Figure 4-1; Eccles, 2011). These fields are aligned on an ENE-trend that has not been adequately explained.

- The Mountain Lake intrusion (76-75 Ma) consists of two uneconomic, ultrabasic volcanic bodies discovered in 1990.

- The Buffalo Head Hills kimberlite field (88 -81 Ma and ~64 Ma) consists of 41 kimberlites discovered between 1997 and 2008, including 28 diamondiferous kimberlites with the highest grade reported in the province so far (K252 with 55 carats per hundred tons (Skelton and Willis, 2002). Four of the kimberlites crop out (K2, K5, K6 and K14), whereas two thirds of the remaining kimberlites are covered by less than 40 m of overburden (Eccles, 2011).

- The Birch Mountains kimberlite field (78-70 Ma) consists of eight kimberlites discovered between 1998 and 2000, two of which were reported to have low diamond contents (Eccles, 2011).

The Buffalo Head Hills and Birch Mountains kimberlites occur as pipe-like and tabular layers. The majority occur as pyroclastic, re-sedimented volcaniclastic and intrusive dikes or sills in complex volcanic fields without apparent feeders.

Abundant literature exists about these kimberlites fields and comprehensive summaries are provided by Dufresne et al. (1996), Eccles (2011) and Banas (2016).

4.5 Surficial Geology

The Northern Plains are blanketed by Neogene fluvial deposits, glaciogenic materials and postglacial sediments of variable thickness and distribution overlying the bedrock surface. Modelled overburden values in the project area range from less than 1 m to as much as 360 m (Alberta Geological Survey, 2020). Maximum thicknesses occur in the northwest corner, and in the central and east-central parts of the project area between Lesser Slave Lake and the Caribou Mountains.

5.0 AEROMAGNETIC SURVEY DATA

5.1 Data Review

RMG reviewed the digital data available in the AER's archives for both completeness and data quality. It was determined that the AER data repository was missing final databases; replacement copies were obtained from the airborne contractors. New data for the Northen Alberta dataset was collected by EON Geosciences, Sander Geophysics Limited, and Xcalibur Multiphysics between February 2021 and May 2022 (Alberta Geological Survey, 2023; Figure 5-1).

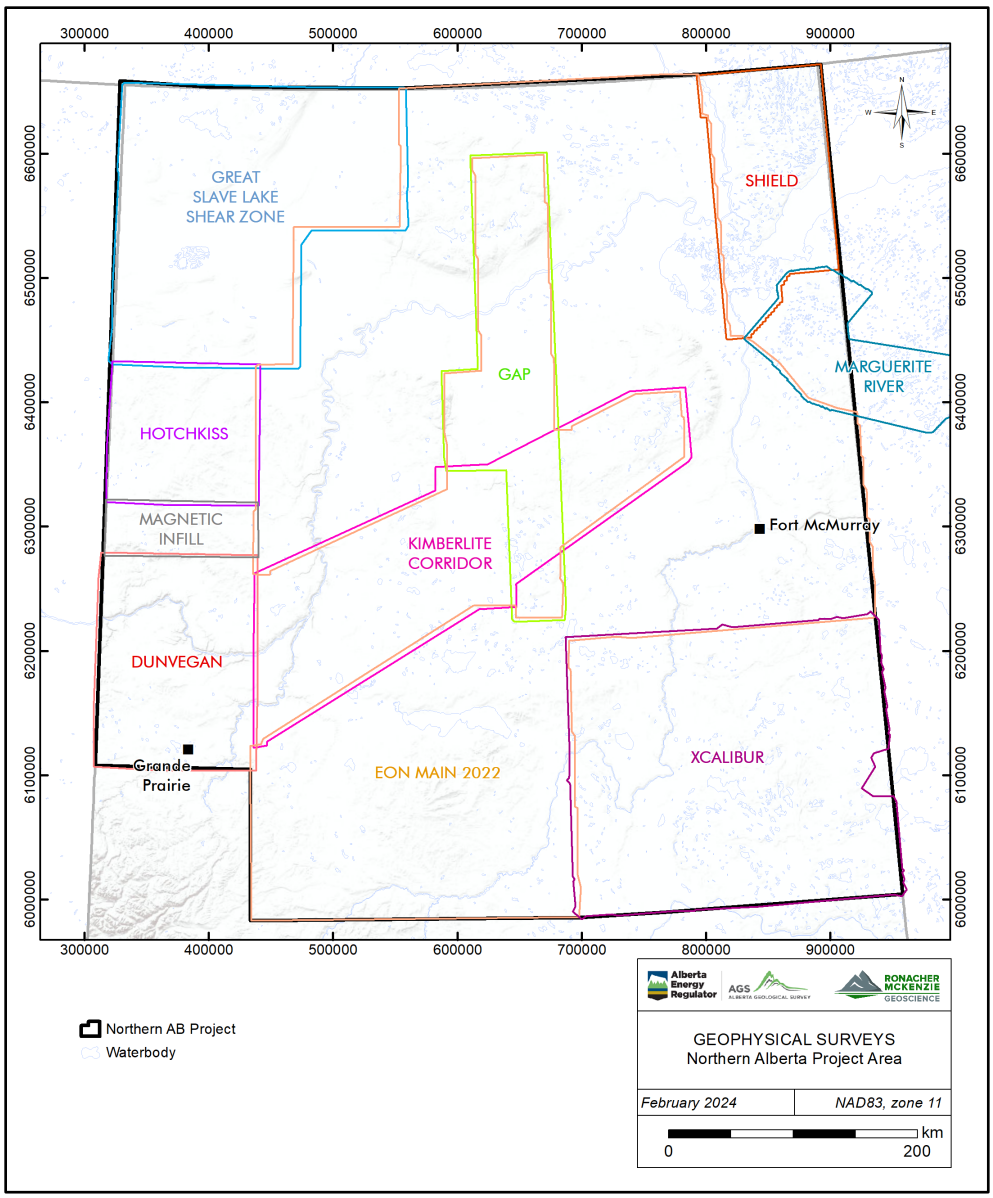

Figure 5-1. Northern Alberta airborne survey blocks.

Additional survey data from prior surveys (Dunvegan, Hotchkiss, Marguerite River) was acquired to fill gaps in coverage. EON Geosciences merged these multiple survey areas to create a contiguous magnetic grid for Northern Alberta (Figure 5-1).

The final processed data were reviewed with reference to the raw measured data to identify any potential data processing and levelling problems. No significant issues were identified.

The airborne contractors performed editing to attenuate cultural effects in the measured data. Cultural effects may not be completely removed but have been attenuated sufficiently to avoid significant problems with calculated filter products.

Flight specifications for each block are summarized in Table 5-1.

Table 5-1. Aeromagnetic survey flight specifications.

Area Name	Contractor	Date	Flying Height (m AGL*)	Survey Line Direction	Survey Line Spacing (m)	Tie Line Direction	Tie Line Spacing (m)
EON Main 2022	GDS-EON	2021-2022	200	90°	800	0°	2500
Gap	GDS-EON	2021	200	87.75°	800	357.75°	2500
Shield	GDS-EON	2021	200	90°	400	0°	2500
Great Slave Lake Shear Zone	Sander Geophysics Limited	2021-2022	200	120°	800	30°	2500
Kimberlite Corridor	Sander Geophysics Limited	2021-2022	200	90°	800	0°	2500
Magnetic Infill	Sander Geophysics Limited	2021-2022	200	90°	800	0°	2500
Xcalibur Block 1	Xcalibur Multiphysics	2021-2022	200	92°	800	2°	2500
Xcalibur Block 2	Xcalibur Multiphysics	2021-2022	200	131°	800	41°	2500
Marguerite River A	GDS-EON	2017	100	44.9°	250	134.9°	1200
Marguerite River B	GDS-EON	2017	100	99.9°	250	9.9°	1200
Marguerite River C	GDS-EON	2017	100	99.9°	400	9.9°	2400
Dunvegan	Sander Geophysics Limited	1995-1996	150	0°	800	90°	2400
Hotchkiss	Sander Geophysics Limited	1996	125	90°	600	0°	1800

**AGL: Above ground level.*

5.2 Derivative and Filter Products

Grid-based filter products were calculated from the total magnetic intensity ("TMI") and International Geomagnetic Reference Field ("IGRF") -removed residual magnetic intensity ("RMI") grids (Table 5-2). The various filter products are used to enhance and highlight different features in the measured data to aid in geologic interpretation. RGB ternary images were also created from selected filter products to produce pseudo-structure and pseudo-geology maps.

Table 5-2. Magnetic Filter Products.

Product	Abbreviation	Description
Total Magnetic Intensity	TMI	Measured data.
Residual Magnetic Intensity	RMI	Measured data, IGRF removed.
TMI/RMI, Pole Reduced	RTP	Transform to vertical magnetic field, simplifies anomaly shapes.
X Horizontal Derivative	DX	Highlights near surface features in N-S direction.
Y Horizontal Derivative	DY	Highlights near surface features in E-W direction.
1st Vertical derivative	VD1	Highlights near surface features.
2nd Vertical derivative	VD2	Enhances subtle near surface features.
Analytic Signal (Total Gradient)	AS	Highlights discrete magnetic bodies and zones of high gradients.
Total Horizontal Derivative	THD	Highlights horizontal changes in the total field.
1st Vertical Derivative of Total Horizontal Derivative	THD_VD1	Enhances THD.
Tilt Derivative	TD	Tilt angle between vertical and horizontal derivatives, highlights magnetic contacts, amplitude independent.
Total Horizontal Derivative of Tilt Derivative	TD_THD	Used with TD to estimate depth of discrete magnetic sources.
Area	AREA	Highlights discrete areas.
Edge	EDGE	Highlights edges of discrete areas.
Geology	GEOLOGY	Pseudo-geology map. Ternary image (RMI/RTP, VD1, VD2) only, no grid data.
Structure	STRUCTURE	Pseudo-structure map. Ternary image (DX, DY, VD1) only, no grid data.
Differential Upward Continuation	DIF_XXX_YYY	Highlights features at selected approximate depths.

Selected filter products are presented in Figure 5-2 through Figure 5-10. All filter products are included in the Digital Appendix B.

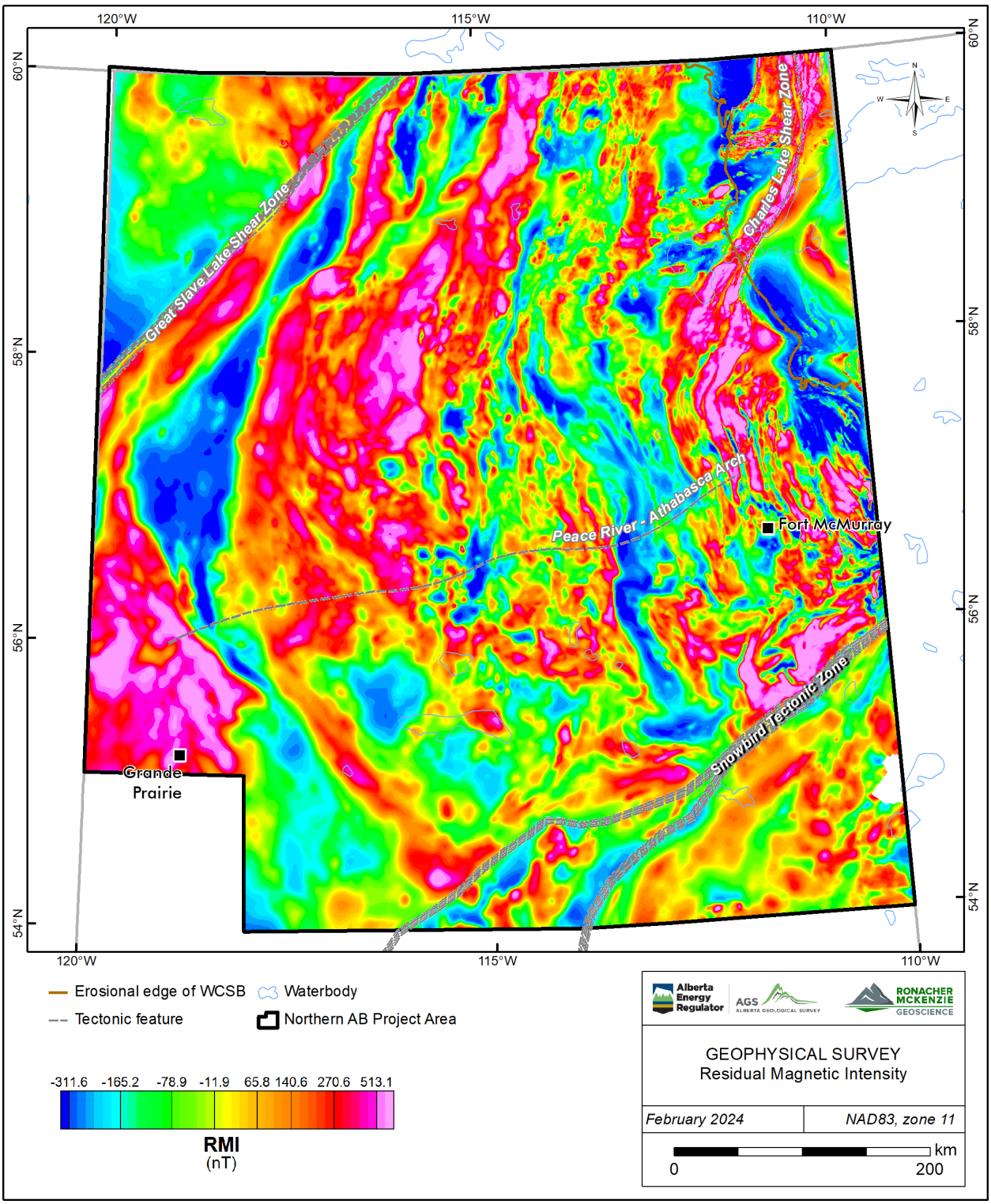

Figure 5-2. Residual Magnetic Intensity ("RMI").

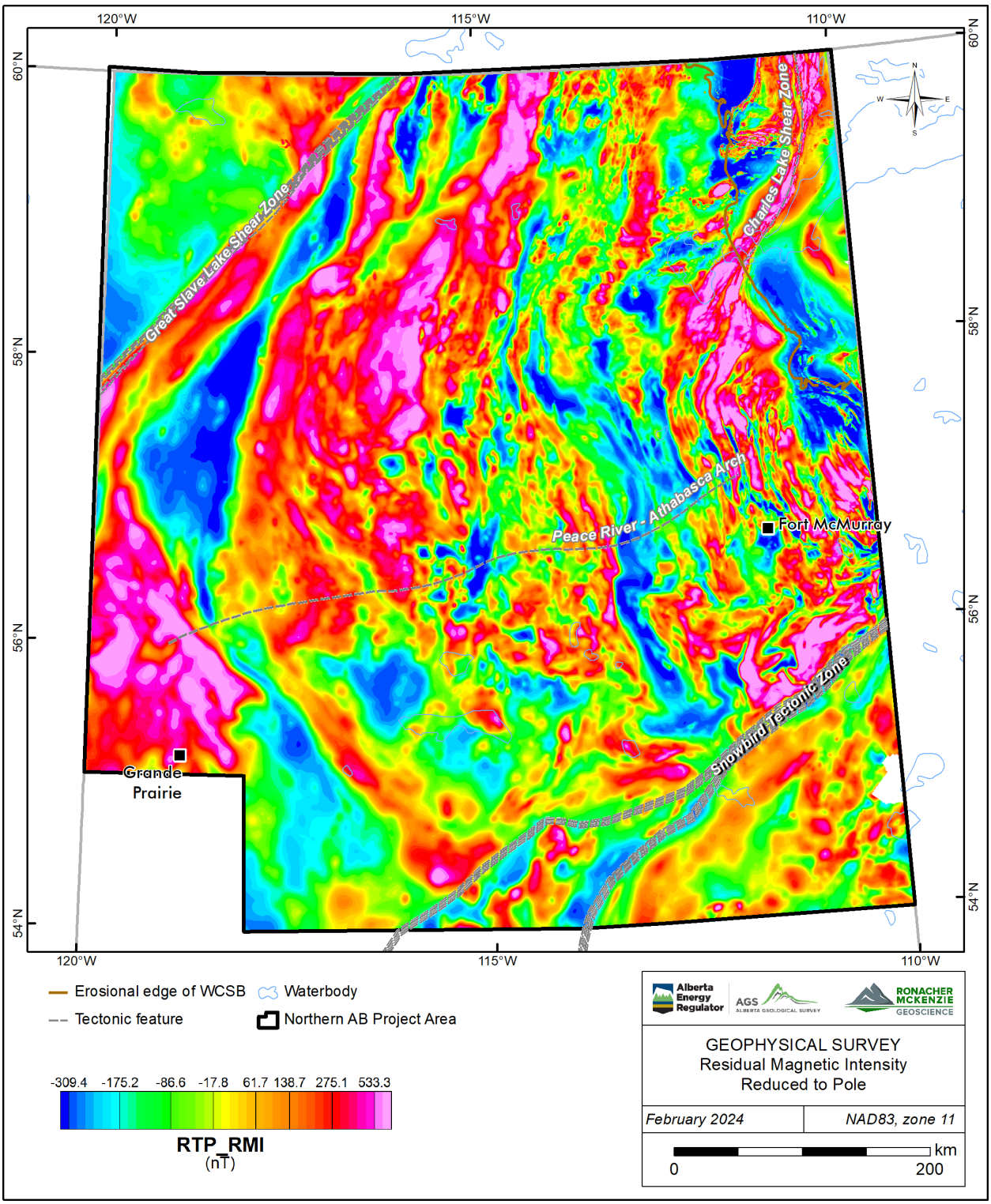

Figure 5-3. RMI, reduced to pole

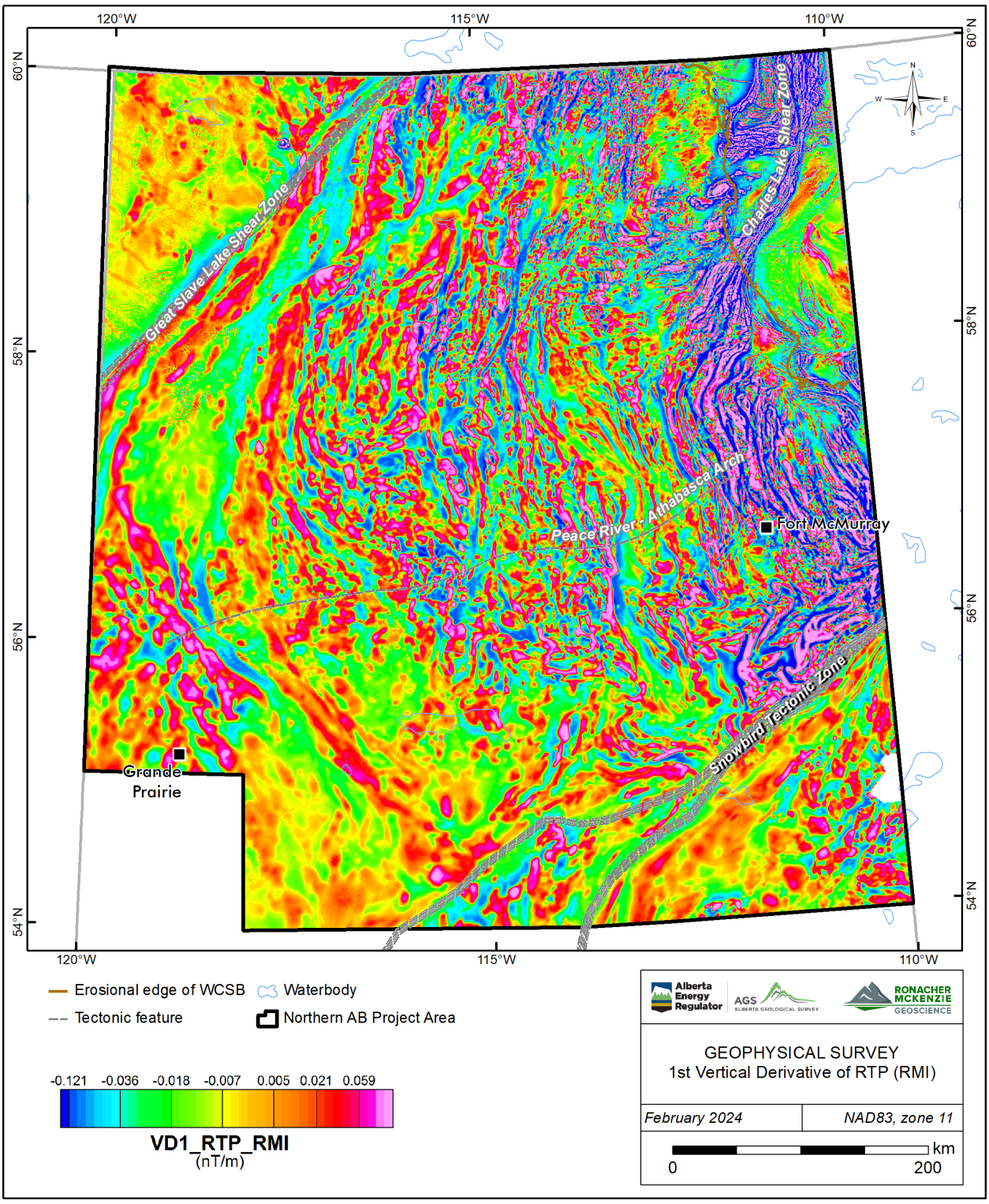

Figure 5-4. RMI, reduced to pole, 1st vertical derivative.

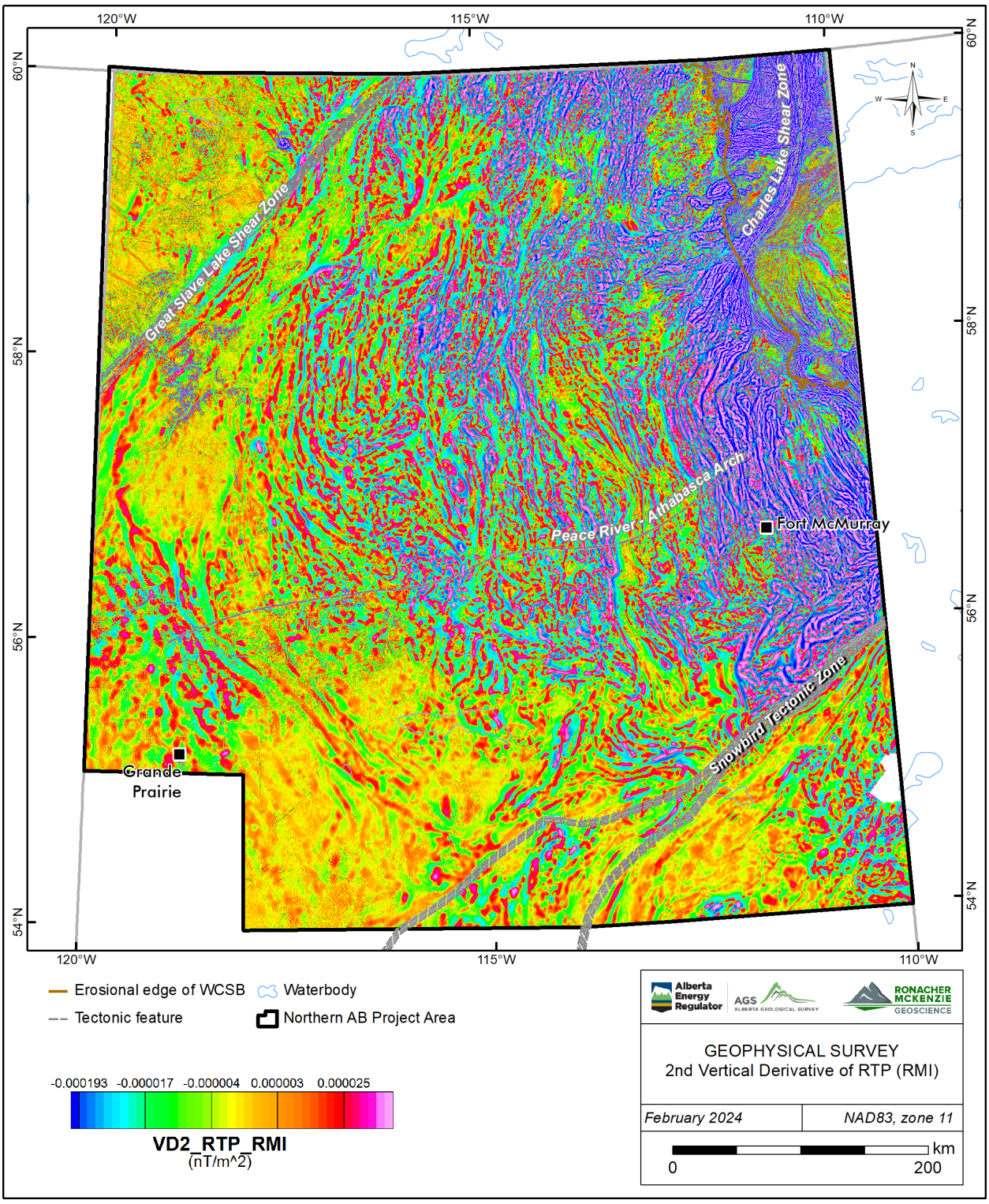

Figure 5-5. RMI, reduced to pole, 2nd vertical derivative.

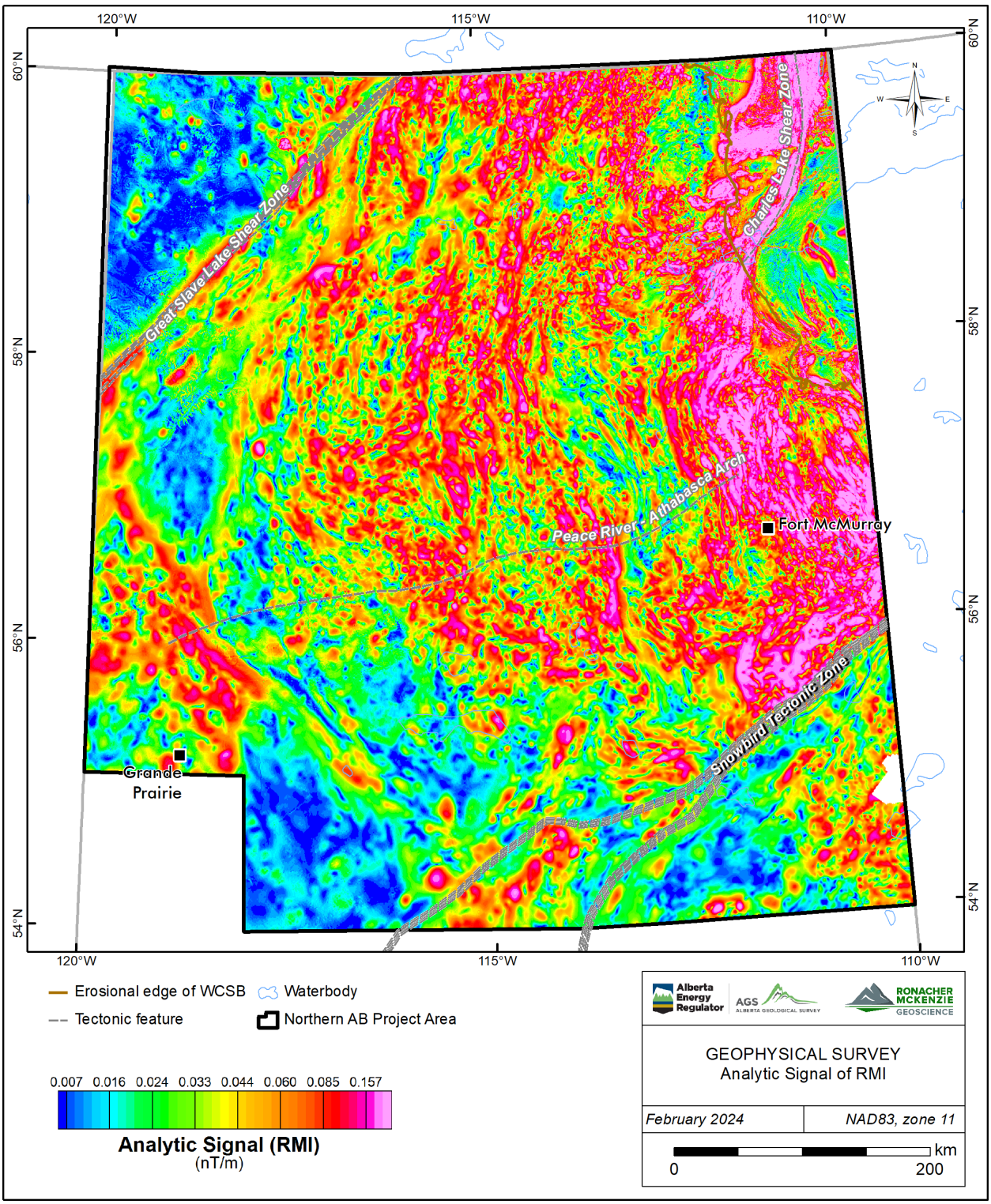

Figure 5-6. RMI, Analytic Signal.

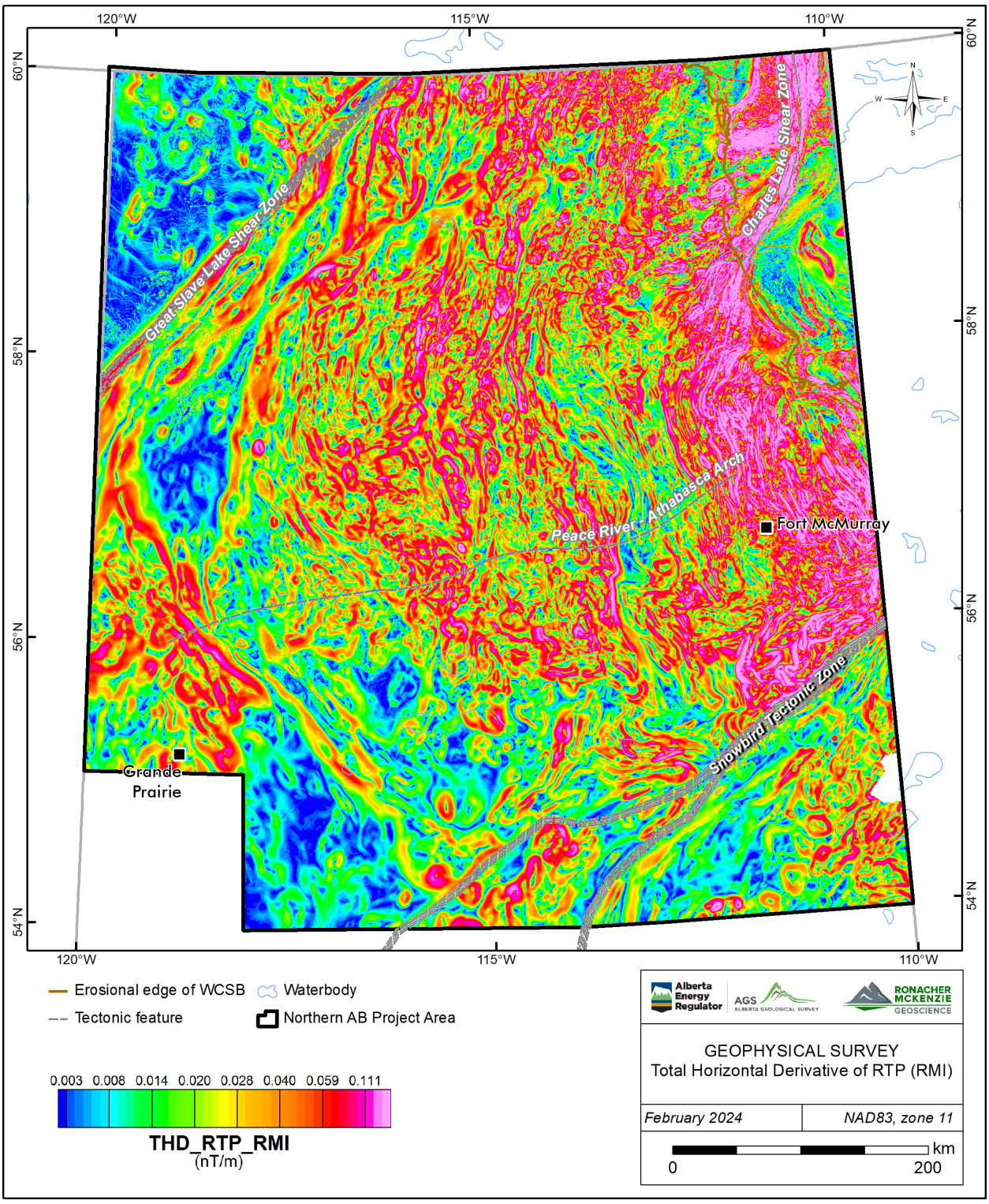

Figure 5-7. RMI, reduced to pole, total horizontal derivative.

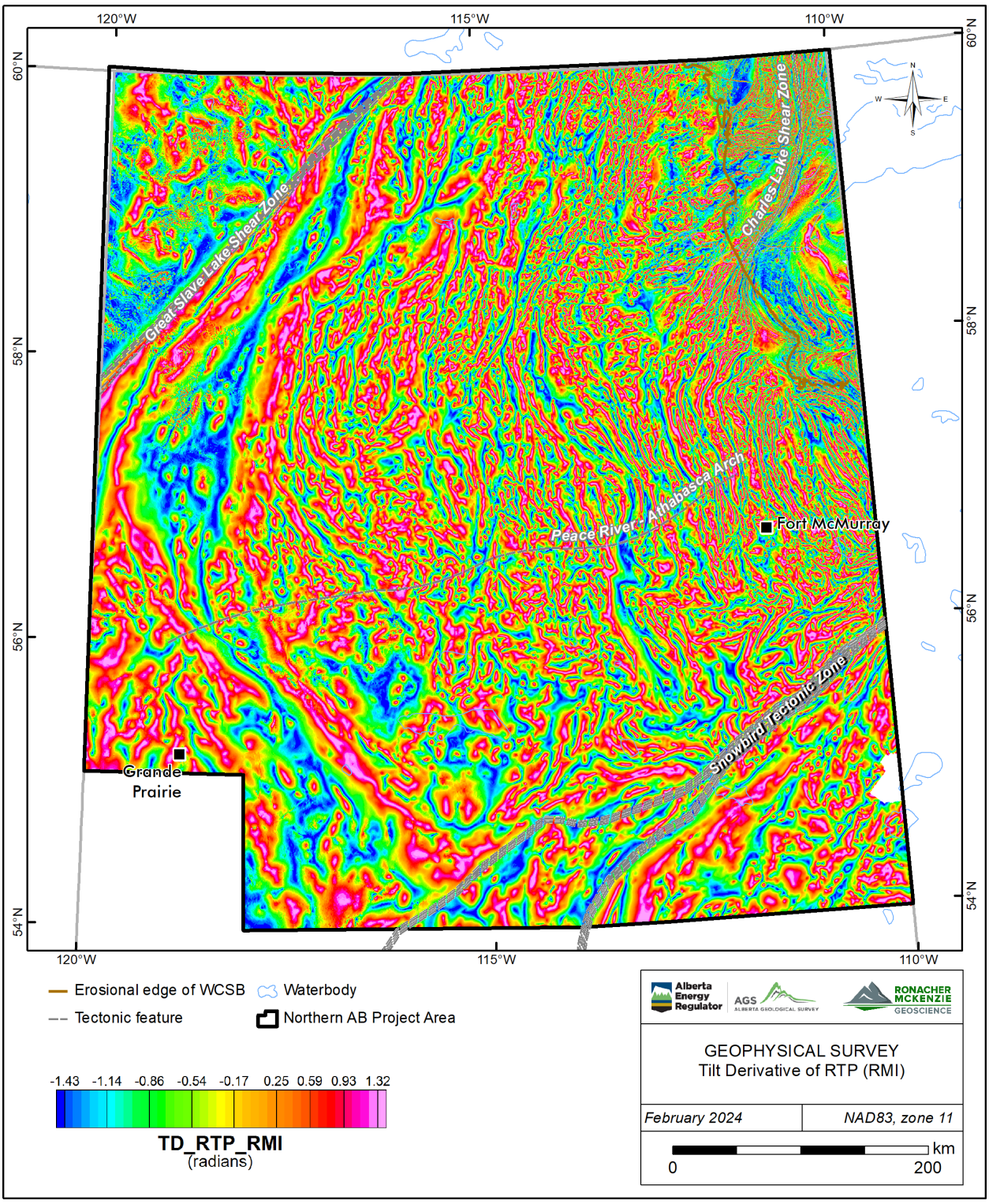

Figure 5-8. RMI, reduced to pole, tilt derivative.

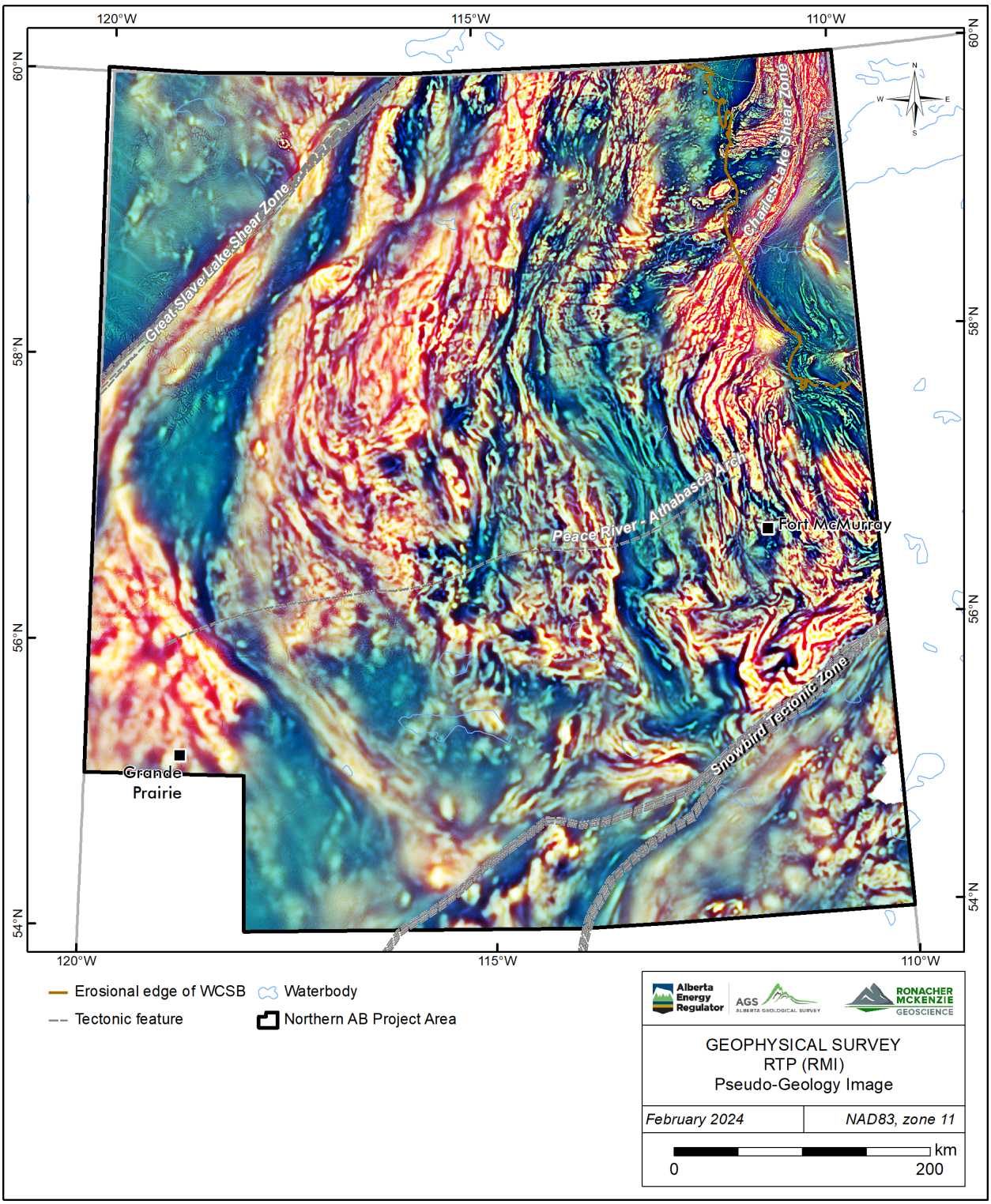

Figure 5-9. RMI, reduced to pole, pseudo-geology ternary image.

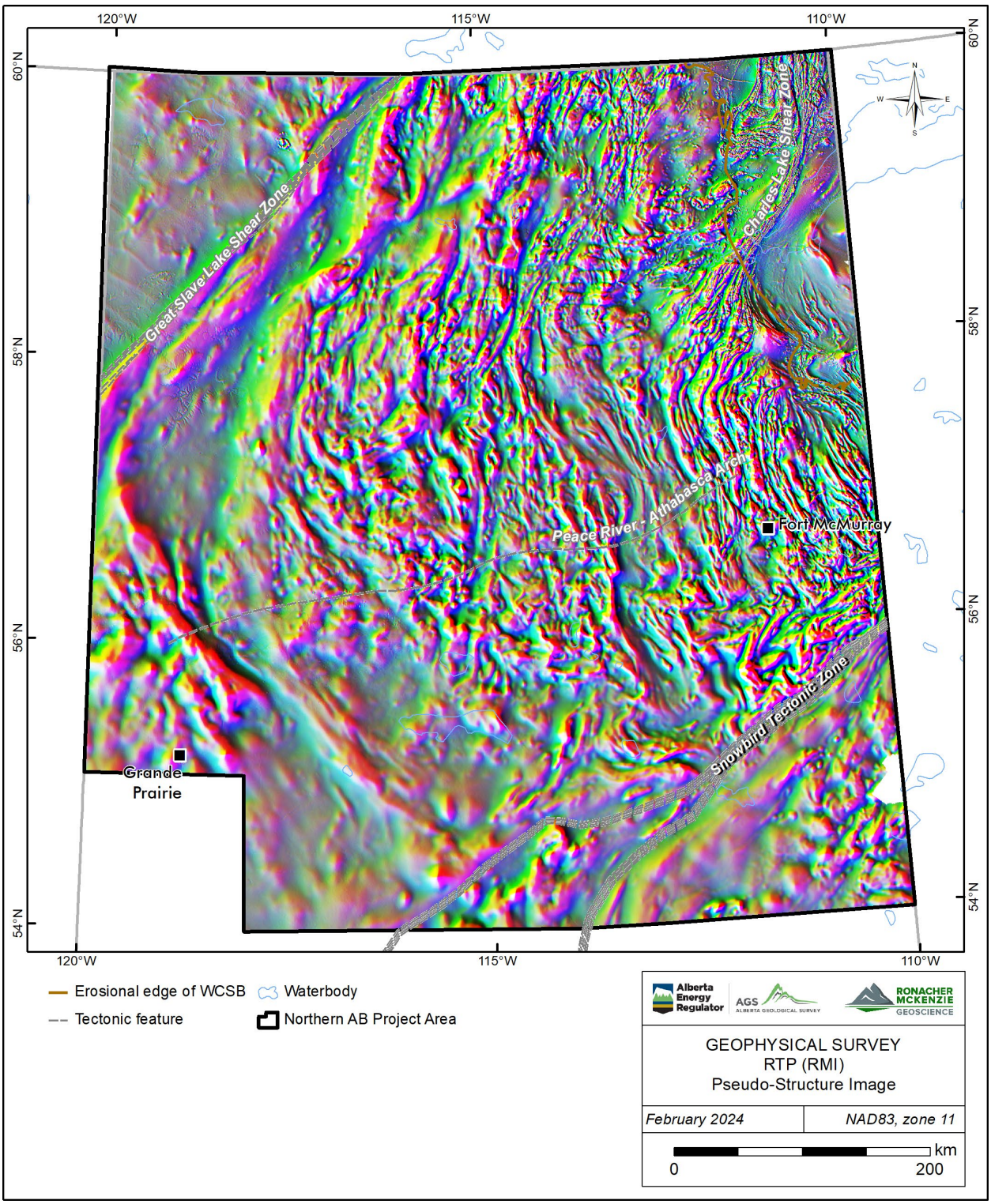

Figure 5-10. RMI, reduced to pole, pseudo-structure ternary image.

Differential upward continuation grids were created to extract information from selected approximate depths. Differential grids show information from an approximate depth range equal to half of the upward continuation distances (e.g., the 3000-5000 m differential grid will show information from approximately 1500 to 2500 m depth). Selected differential maps are presented in Figure 5-11 and Figure 5-12.

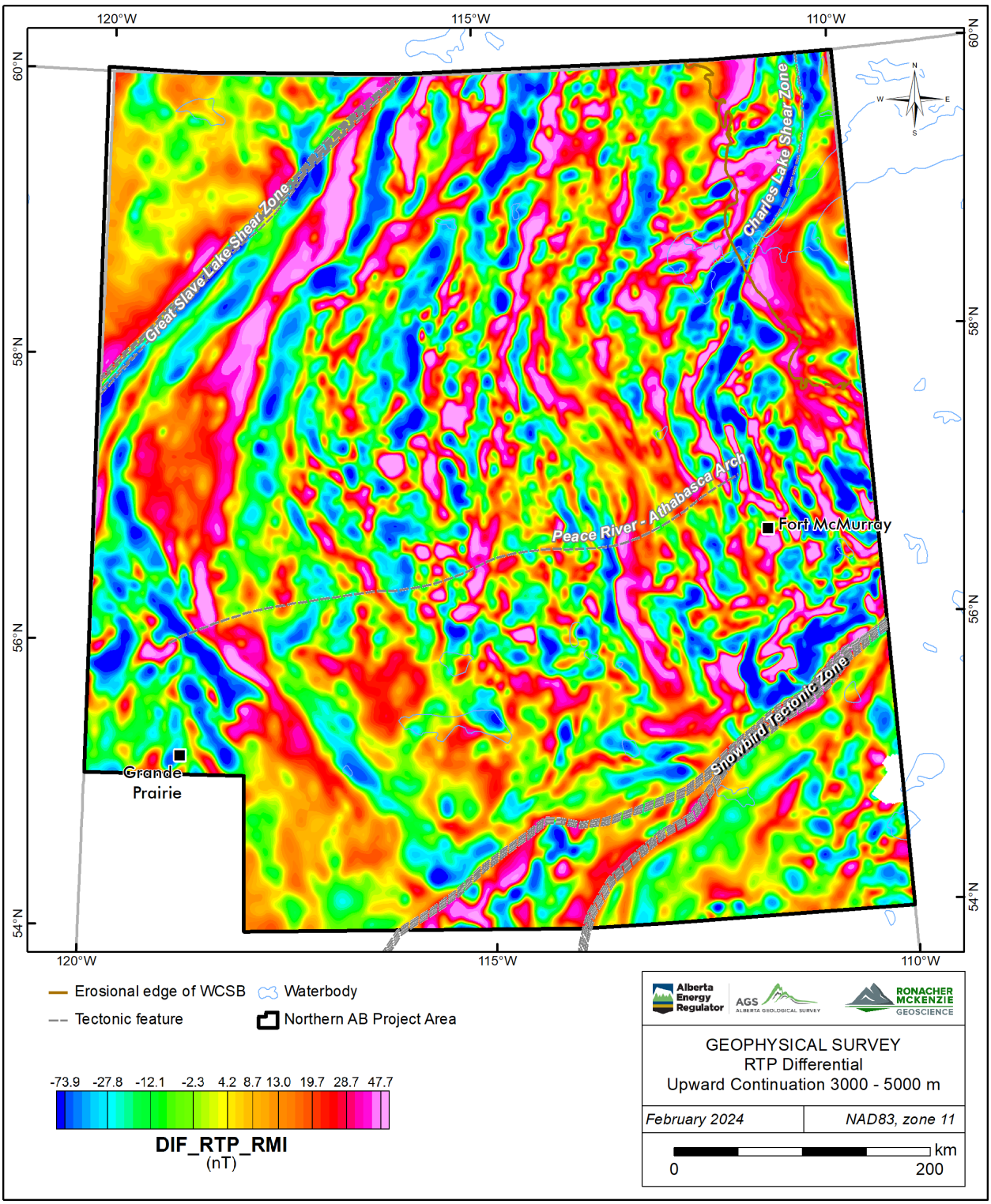

Figure 5-11. Differential upward continuation, 3000-5000 m (1500-2500 m approximate depth).

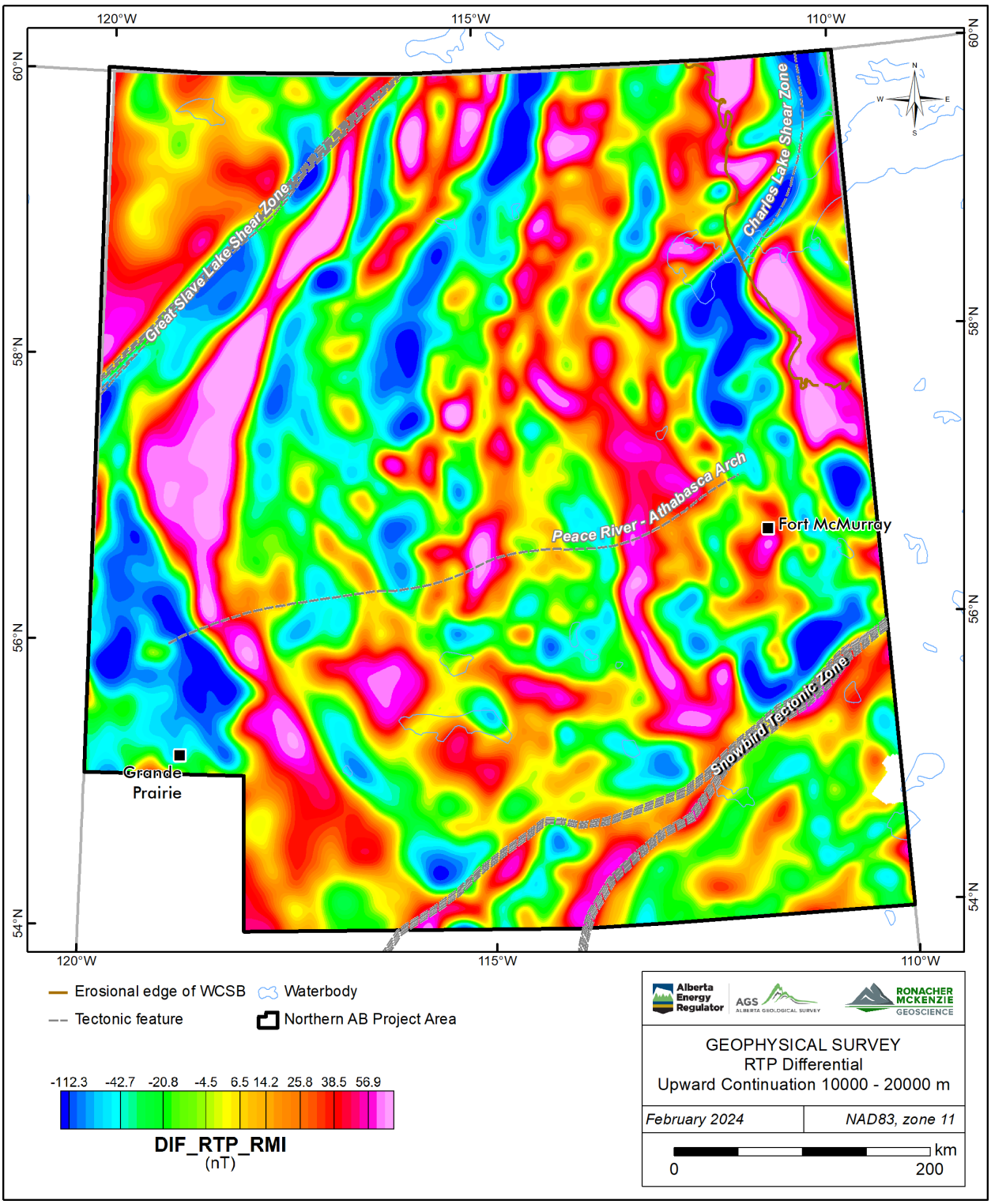

Figure 5-12. Differential upward continuation, 10000-20000 m (5000-10000 m approximate depth).

The gridded magnetic data are also displayed using alternate colour distributions to aid in data interpretation (Table 5-3). Different colour distributions are used to help identify structures in the interpretation process. For example, greyscale maps are useful for highlighting high and low areas while minimizing the effects of local amplitudes, and isoluminant palettes (e.g., CET i1 described in Kovesi 2015) mitigate artificial highlighting caused by perceived brighter colours in commonly used rainbow palettes, particularly in the yellow and green ranges.

Table 5-3. Colour palettes applied to geophysical datasets.

Colour Distribution	Abbreviation	Description
Rainbow	(none)	Standard blue through purple colour palette.
Greyscale	BW	Black to white colour range, often easier to see structures.
Centre for Exploration Targeting (I1)	CET	Isoluminant colour range developed by University of Western Australia. No 'bright spots' in the spectrum to artificially attract the eye.

Selected examples of alternate colour distributions are shown in Figure 5-13 through Figure 5-15.

A complete set of georeferenced gridded data including alternate colour distributions is included in the Digital Appendix B.

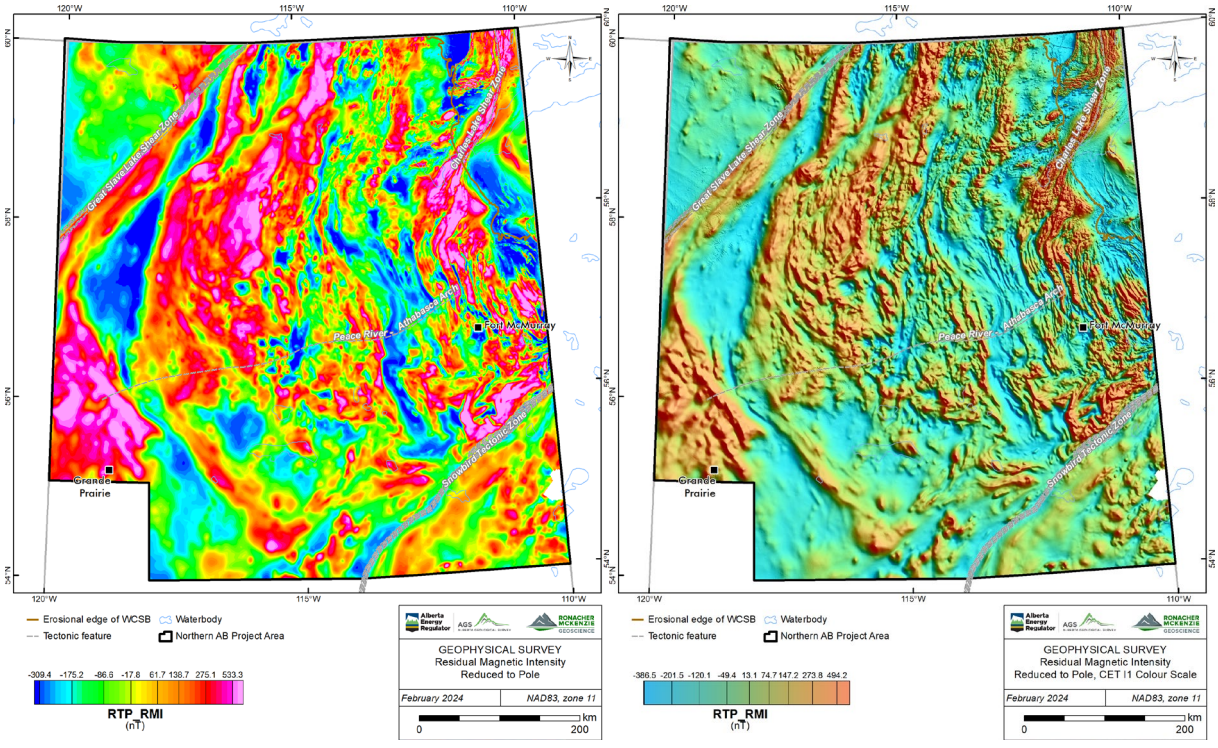

Figure 5-13. RMI, reduced to pole, standard rainbow (left) and CET i1 isoluminant (right) colour distributions.

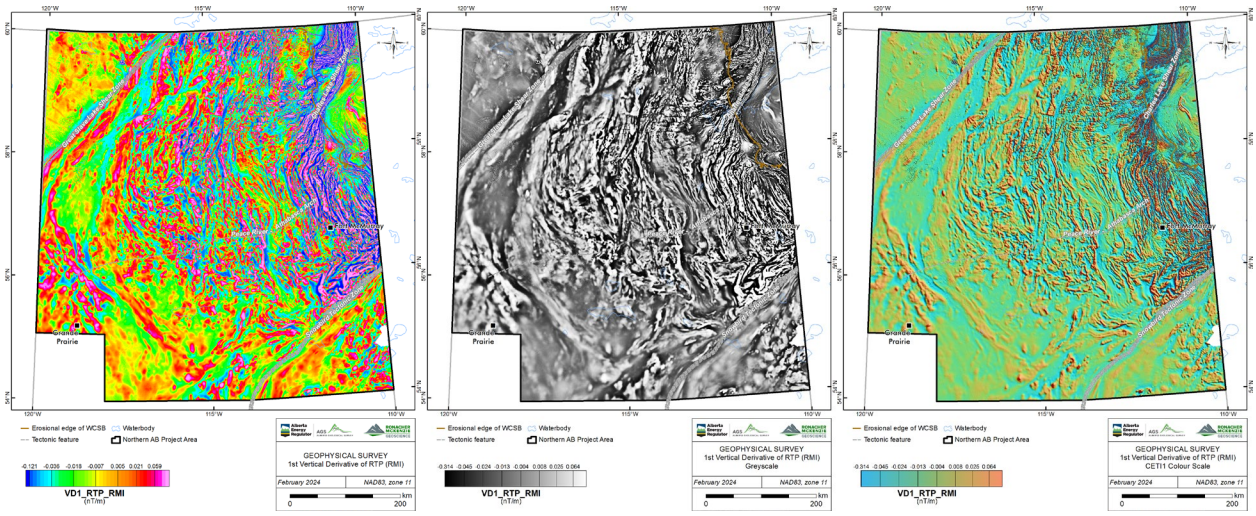

Figure 5-14. 1st vertical derivative (RTP), standard rainbow (left), greyscale (centre), and CET i1 isoluminant (right) colour distributions.

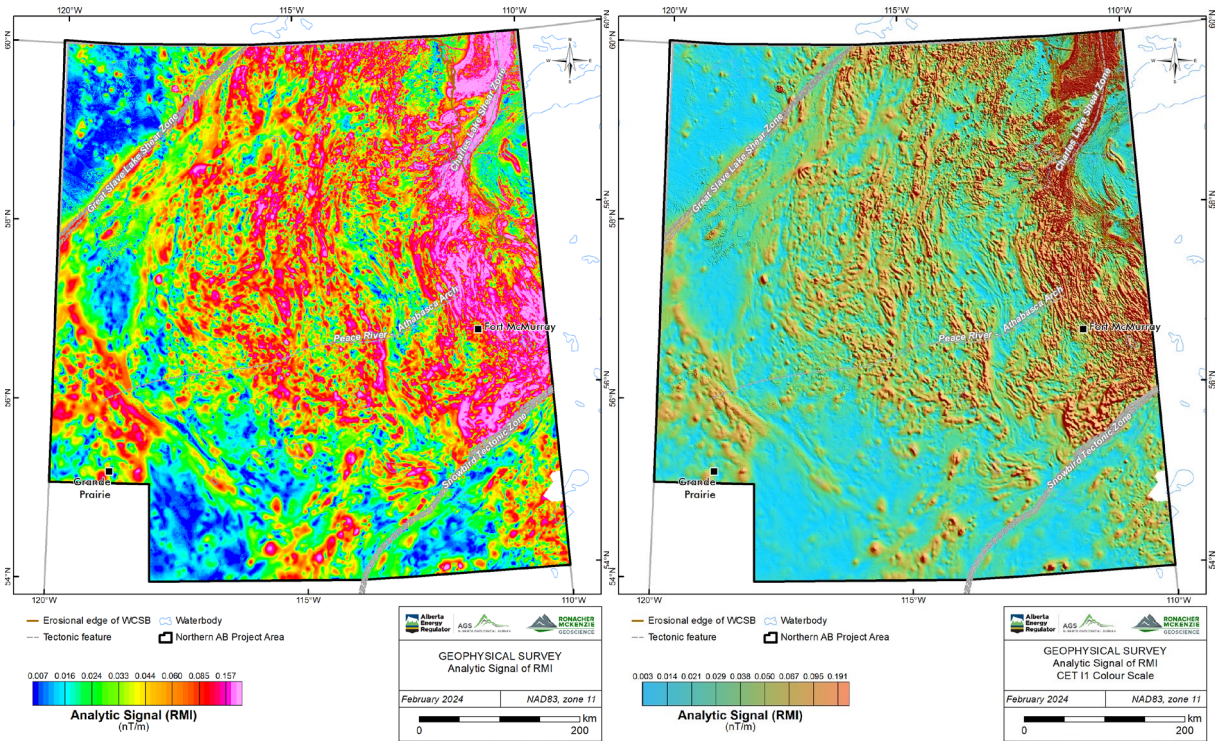

Figure 5-15. RMI, Analytic Signal, standard rainbow (left) and CET i1 isoluminant (right) colour distributions.

5.3 Automatic Structure Detection

RMG collaborated with Fathom Geophysics to perform automatic structure detection and to generate additional magnetic products to assist with the geological interpretation of the magnetic basement in northern Alberta. Automatic structure detection was applied to the gridded magnetic data; the processing included application of standard filters as well as application of Fathom Geophysics' structure detection and radial symmetry filters. The methodology and results of this work are presented in Appendix 1 – Automatic Detection – Fathom Geophysics Report. The related final digital products are in the Digital Appendix C.

The additional filter and image processing products created by Fathom Geophysics are listed in Table 5-4. An example of an image processing product, a ternary image of 1VD, tilt angle, and horizontal gradient magnitude ("HGM"), is shown in Figure 5-16.

Automatic structure detection filter is a linear feature detection algorithm used to highlight ridges, valleys, or edges in gridded data. Automated structure detection is a multi-scale phase congruency algorithm in which features are highlighted either in areas of low or high magnetic contrast, irrespective of amplitude. The method also allows inference of the estimated depth of structures between 0.5 and 1 times the filter wavelength, assuming shorter wavelengths are related to shallow structures and longer wavelengths are related to deeper structures (which may not always be the case). Structure detection products are listed in Table 5-5.

Radial symmetry is a filtering process that identifies equant discrete features in the data. The algorithm seeks locations around which data values either decrease or increase in all directions. These features may be related to stocks, batholiths, cupolas, alteration haloes, kimberlites, diatremes, steeply plunging mineralized zones, and breccia pipes. Radial symmetry products were calculated using wavelengths from 500-2000 m, starting from a number of different residuals. Radial symmetry products are listed in Table 5-6.

Table 5-4. Additional filter and image products.

Product	Abbreviation	Description
Filter Products		
Automatic Gain Control (standard deviation = 30)	AGC30	Evens anomaly amplitudes to make subtle features more visible, longer wavelengths are suppressed.
Pseudogravity	PGrav	Useful for highlighting large scale features.
Pseudogravity residual	PGravRes	Difference between 0-2000 m upward continued pseudogravity. Longest wavelength features suppressed to highlight intermediate scale features.
Horizontal gradient of PGravRes	PGravResHGM	Highlights edges of intermediate scale features.
Small-scale residual	Res500_2000	Differential upward continuation residual, 500-2000 m. Highlights sources at 250-1000 m depth.

Product	Abbreviation	Description
Medium-scale residual	Res2000_5000	Differential upward continuation residual, 2000-5000 m. Highlights sources at 1000-2500 m depth.
Large-scale residual	Res5000_10000	Differential upward continuation residual, 5000-10000 m. Highlights sources at 2500-5000 m depth.
Vertical derivative minus horizontal derivative	VDMHGM	Accentuates contrast in 1st vertical derivative, aids in highlighting shallow features.
Vertical integral	VINT	Vertical integral of total field.
Analytic signal of vertical integral.	VIAS	Produces a result with similar amplitudes and wavelengths to total field, with reduced effects of magnetization direction and remanence.
Image Products		
Ternary of directional derivatives	X_Y_Z	Ternary images (CMY+RGB) of 1st X, Y, and vertical derivatives.
Ternary of 1VD, Tilt, HGM	1VD_Tilt_HGM	Ternary images (CMY+RGB) of 1VD, tilt angle, horizontal gradient.
Ternary of residuals	SmRes_MedRes_LgRes	Ternary images (CMY+RGB) of small, medium, large-scale residuals.
Ternary of RTP, VIAS, Asig	RTP_vias_asig	Ternary images (CMY+RGB) of RTP, analytic signal of vertical integral, and analytic signal. Helps identify remanent zones.
Ternary of pseudogravity	Prav_PGravRes_PGravRes HGM	Ternary images (CMY+RGB) of Pseudogravity, pseudogravity residual, and horizontal gradient of pseudogravity residual.

Table 5-5. Structure detection products.

Product	Abbreviation	Description
Fabric Orientation (RTP and AGC)	Fabric_Orientation	Reflects the orientation of long-wavelength features.
Total Structure (RTP and AGC)	StructX_Total	Total structure detected. X = filter wavelength (100 to 3200 m).
Oriented Structural Domains	StructX_OriDom_Th	Total structure (X = filter wavelength), thresholded into orientation domains.
Vectorized Structure	StructX_Total_Vec	Vectorized total structure (X = filter wavelength).
Belt-parallel structure	StructX_Para	Structure parallel to major belts (X = filter length).
Vectorized belt-parallel structure	StructX_Para_Vec	Vectorized structure parallel to major belts (X = filter length).
Belt-crossing structure	StructX_Cross	Structure crossing major belts (X = filter length).
Vectorized belt-crossing structure	StructX_Cross_Vec	Vectorized structure crossing major belts (X = filter length).

Table 5-6. Radial Symmetry products

Product	Code	Description
Radial Symmetry Lows	Res_X_Y_RSymZ_mi_Lows	Magnitude-independent radial symmetry at wavelength Z from X to Y residual, lows. Also vectorized.
Radial Symmetry Highs	Res_X_Y_RSymZ_mi_Highs	Magnitude-independent radial symmetry at wavelength Z from X to Y residual, highs. Also vectorized.
Radial Symmetry Highs and Lows	Res_X_Y_RSymZ_mi_Highs_and_Lows	Magnitude-independent radial symmetry at wavelength Z from X to Y residual, highs and lows. Also vectorized.

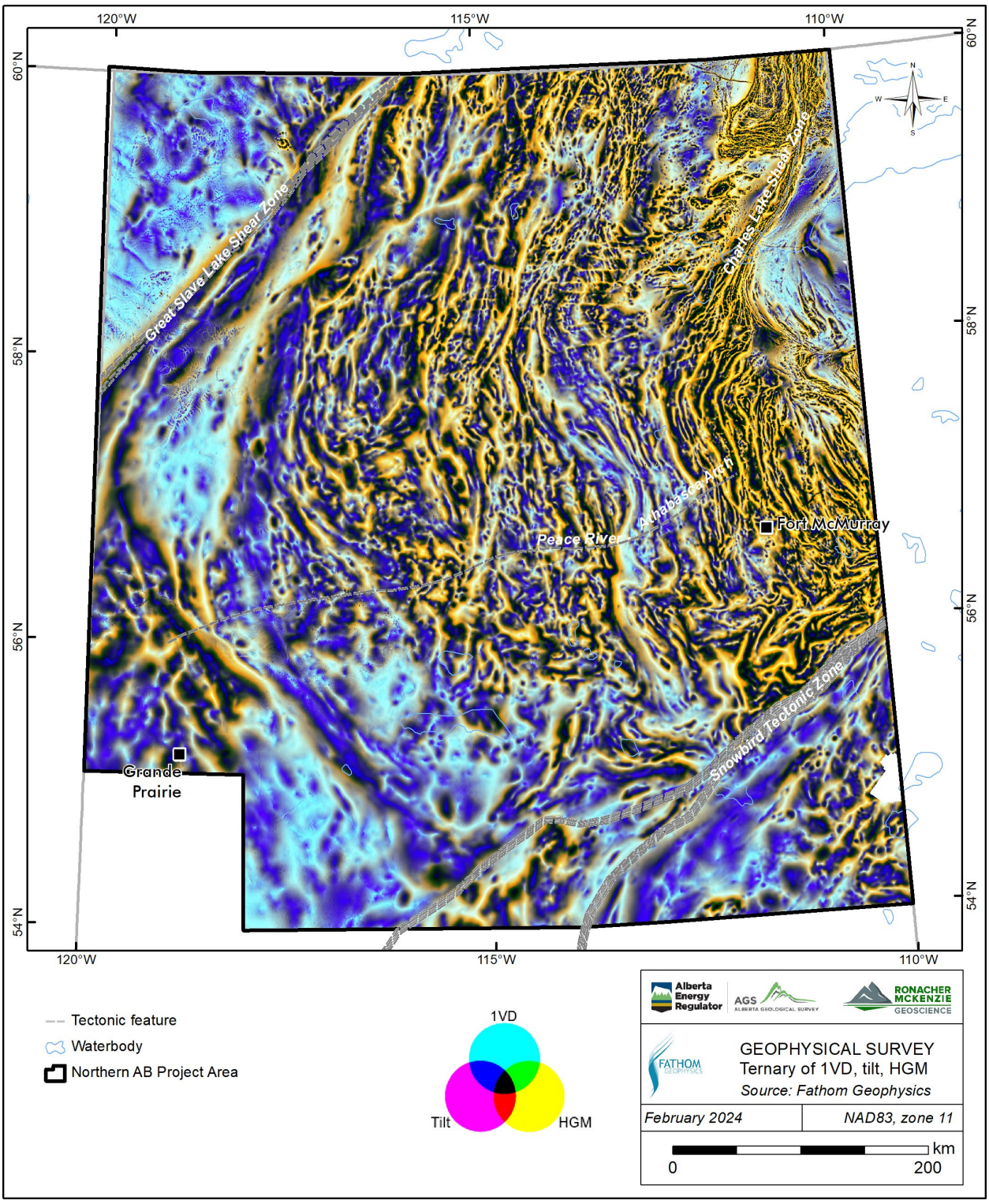

Figure 5-16. CMY ternary image displaying the 1VD, tilt angle, and HGM results from the RTP.

6.0 GRAVITY SURVEY DATA

6.1 Data Review

RMG reviewed the digital gravity data available in the AER's archives for both completeness and data quality. It was determined that the AER data repository was missing final databases; replacement copies were obtained from the airborne contractors. Sander Geophysics Limited (SGL) flew two survey areas for gravity as well as magnetics using the SGL AIRGrav system, the Great Slave Lake Shear Zone (GSLSZ) and Kimberlite Corridor (KC). Flight specifications for the gravity surveys are summarized in Table 6-1.

Table 6-1. Gravity survey flight specifications.

Area Name	Contractor	Date	Flying Height (m AGL)	Survey Line Direction	Survey Line Spacing (m)	Tie Line Direction	Tie Line Spacing (m)
Great Slave Lake Shear Zone	Sander Geophysics Limited	2021-2022	200	120°	800	30°	2500
Kimberlite Corridor	Sander Geophysics Limited	2021-2022	200	90°	800	0°	2500

6.2 Derivative and Filter Products

Grid-based filter products were calculated from the complete Bouguer anomaly grid for each area (Table 6-2). The various filter products are used to enhance and highlight different features in the measured data to aid in geologic interpretation.

The SGL AIRGrav system records gravity data in each of 3 axes: Z (vertical), X (East), and Y (North). The same set of filters was applied to each of the three gravity components (Gx, Gy, Gz). Table 6-2 lists the filter products using Gz as the example; identical filter products were calculated for Gx and Gy as well.

Table 6-2. Gravity Filter Products.

Product	Abbreviation	Description
Bouguer Anomaly (Z)	Gz	Corrected measured data.
Trend Removed Bouguer Anomaly	Gz_TRND3	Gz with 3rd order regional trend removed to highlight local anomalies.
1st Vertical derivative	Gzz	Highlights near surface features.
2nd Vertical derivative	Gzz2	Enhances subtle near surface features.
X Horizontal Derivative	Gzx	Highlights near surface features in E-W direction.

Product	Abbreviation	Description
Y Horizontal Derivative	Gzy	Highlights near surface features in N-S direction.
Analytic Signal (Total Gradient)	Gz_AS	Highlights discrete bodies and zones of high gradients.
Total Horizontal Derivative	Gz_THD	Highlights horizontal changes in the total field.

Selected filter products are presented in Figure 6-1 through Figure 6-10. All filter products are included in the Digital Appendix B.

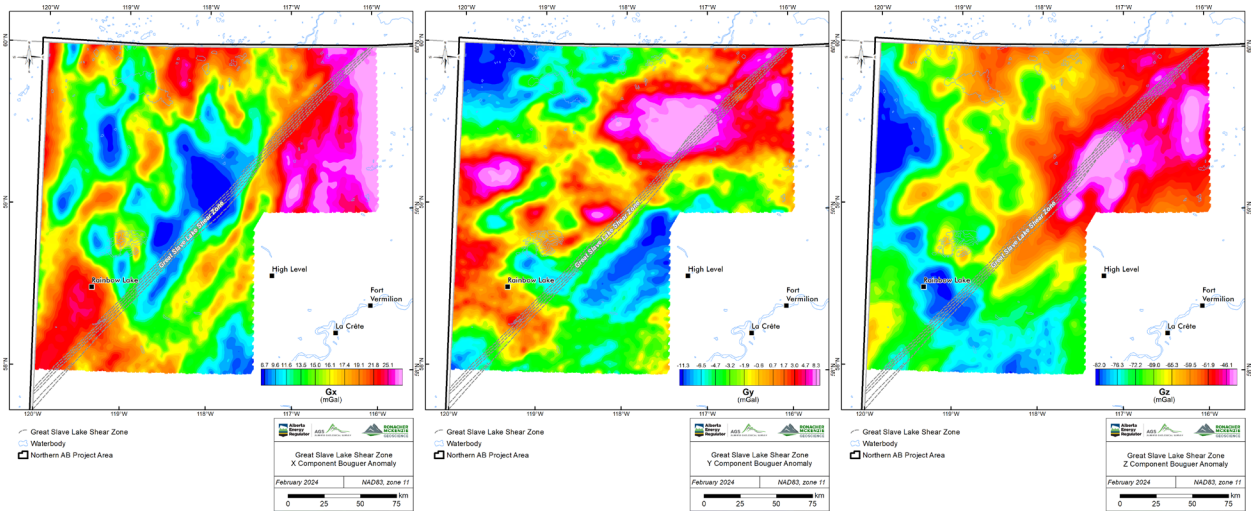

Figure 6-1. Great Slave Lake Shear Zone Bouguer Anomaly. Gx (left), Gy (centre), Gz (right).

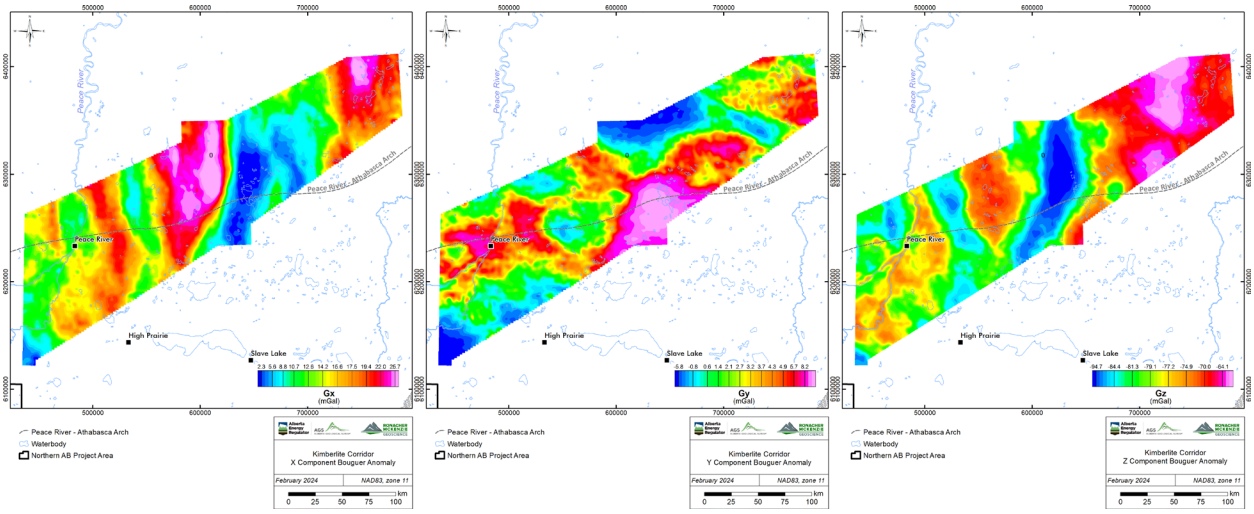

Figure 6-2. Kimberlite Corridor Bouguer Anomaly. Gx (left), Gy (centre), Gz (right).

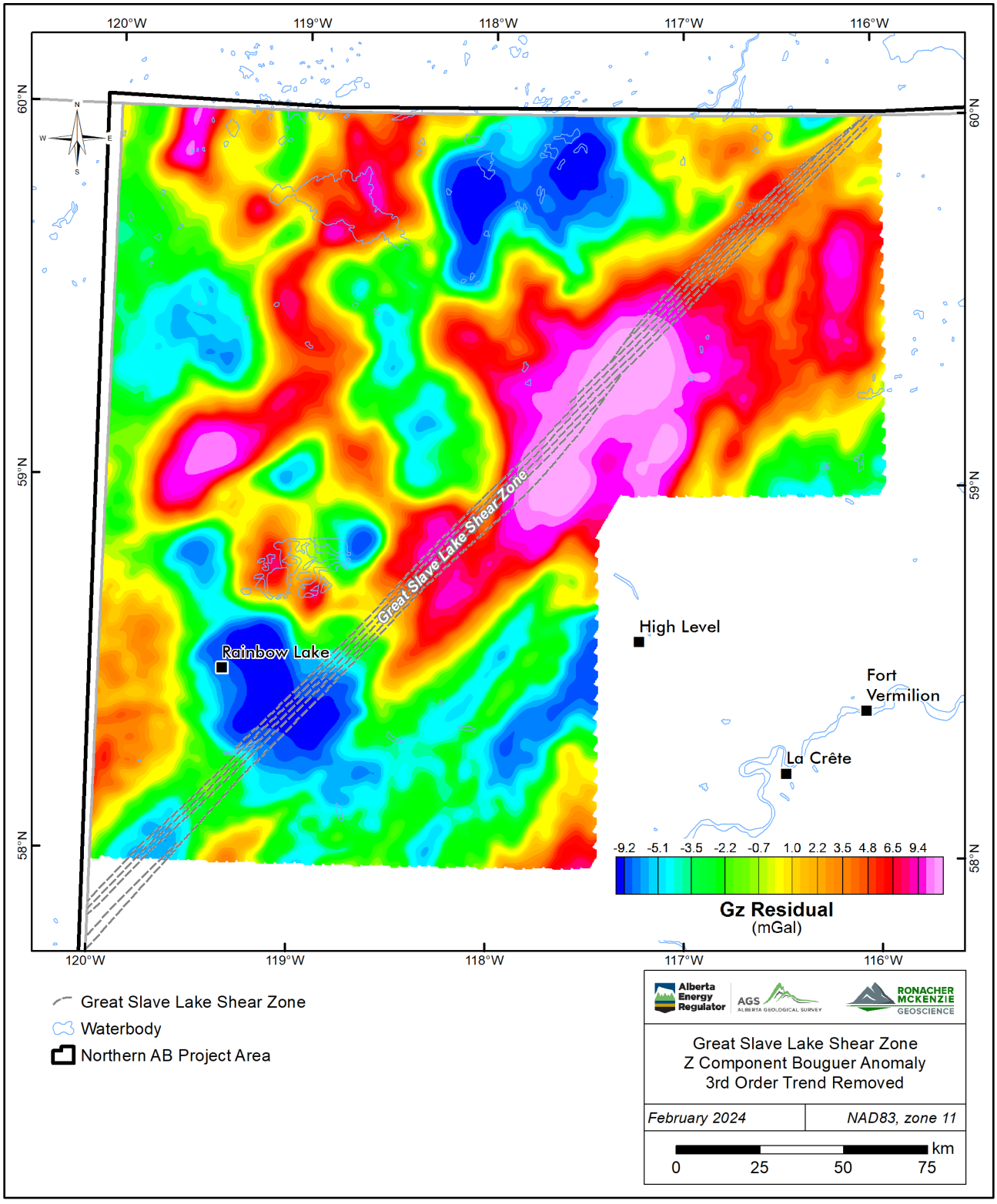

Figure 6-3. Great Slave Lake Shear Zone Gz Bouguer Anomaly, 3rd order trend removed.

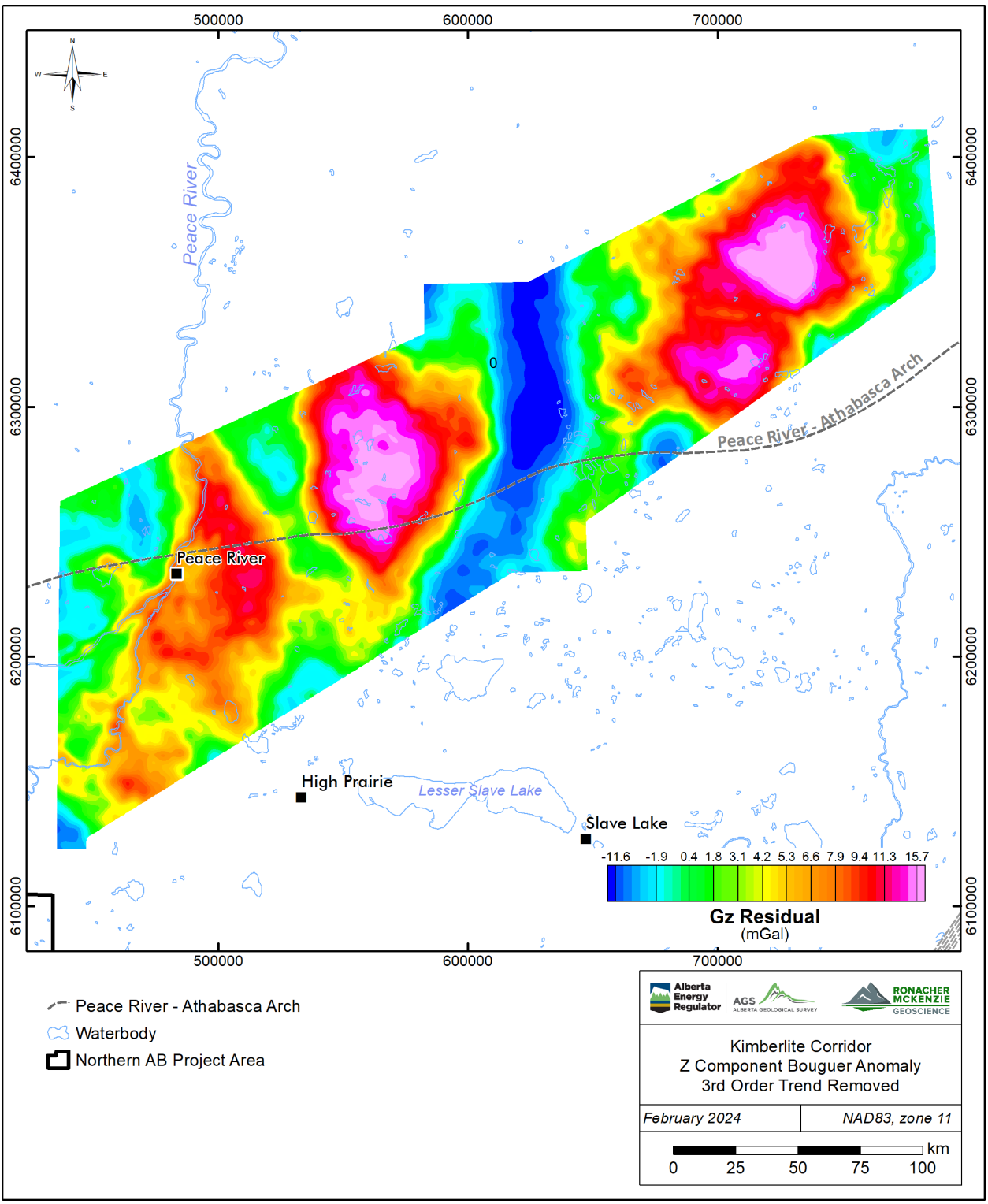

Figure 6-4. Kimberlite Corridor Gz Bouguer Anomaly, 3rd order trend removed.

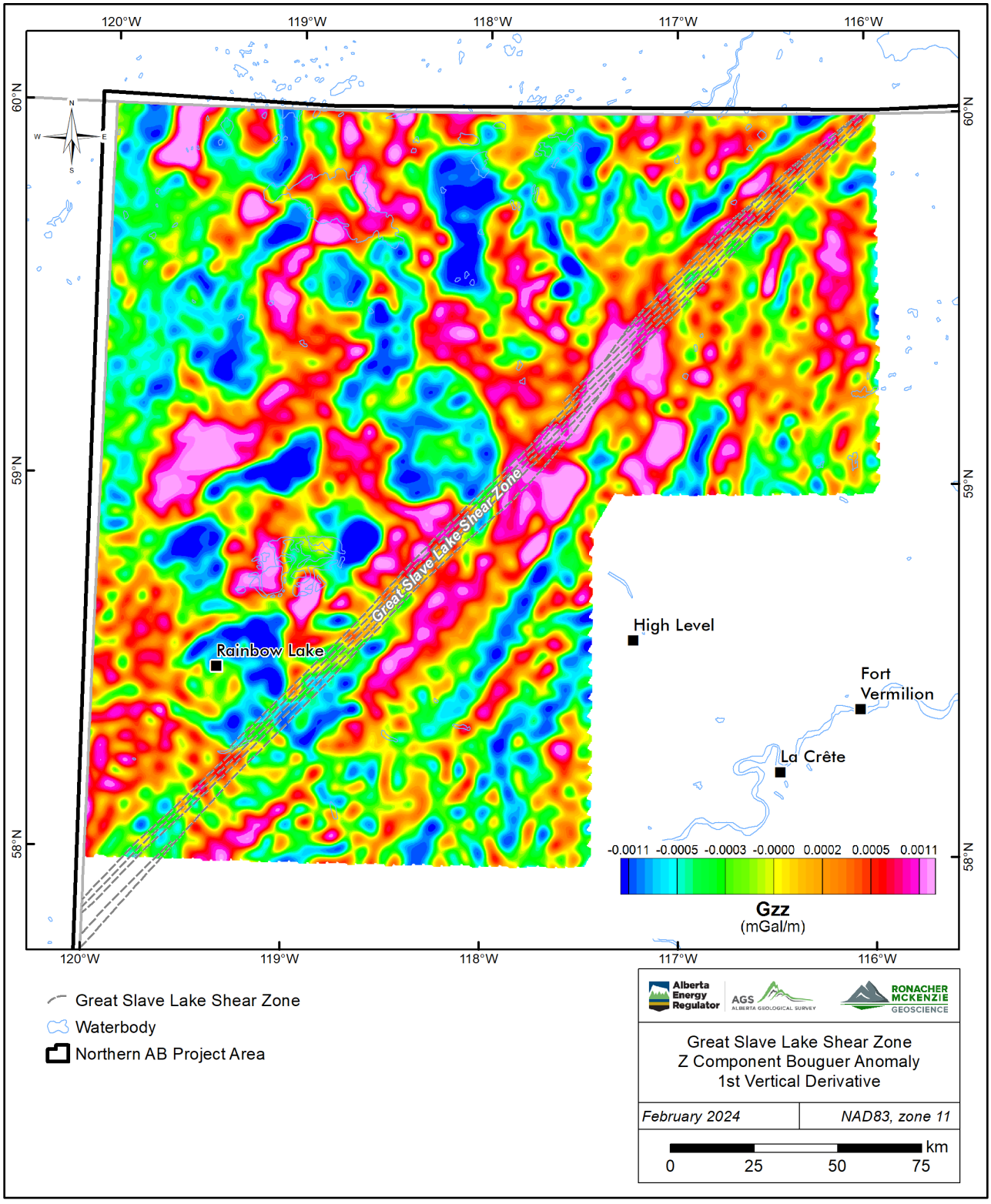

Figure 6-5. Great Slave Lake Shear Zone 1st vertical derivative of Bouguer anomaly (Gzz).

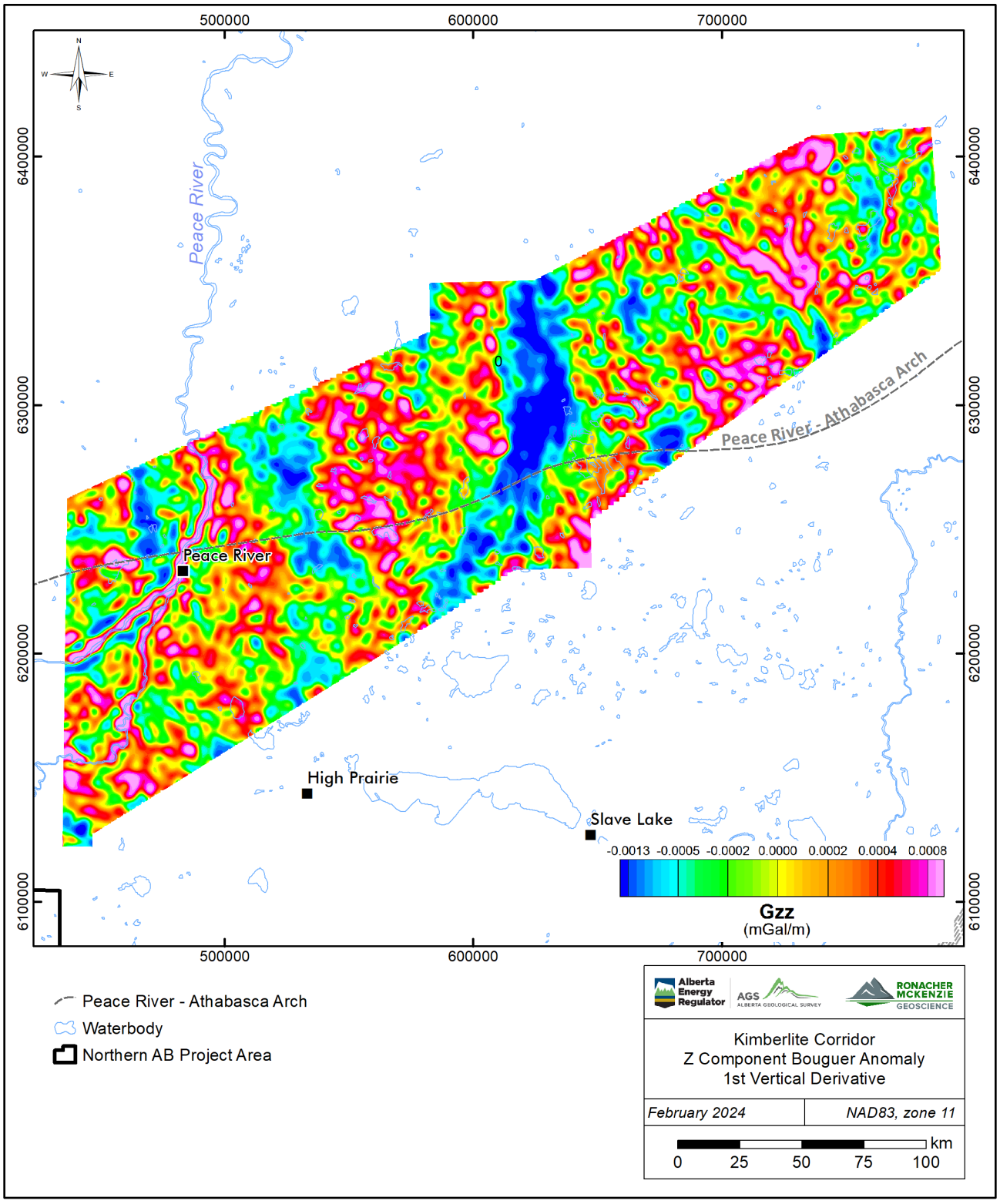

Figure 6-6. Kimberlite Corridor 1st vertical derivative of Bouguer anomaly (Gzz).

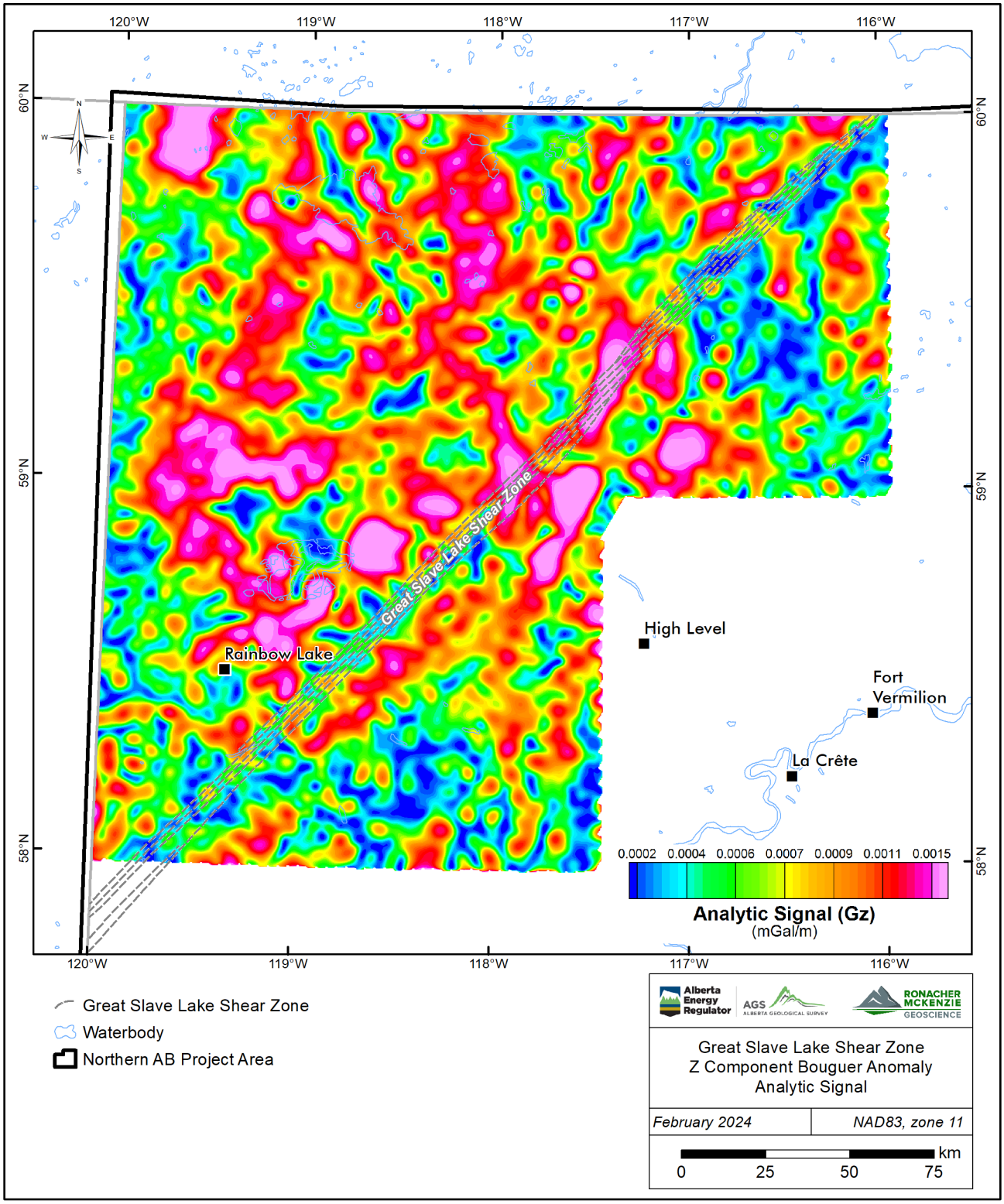

Figure 6-7. Great Slave Lake Shear Zone Analytic Signal (Gz).

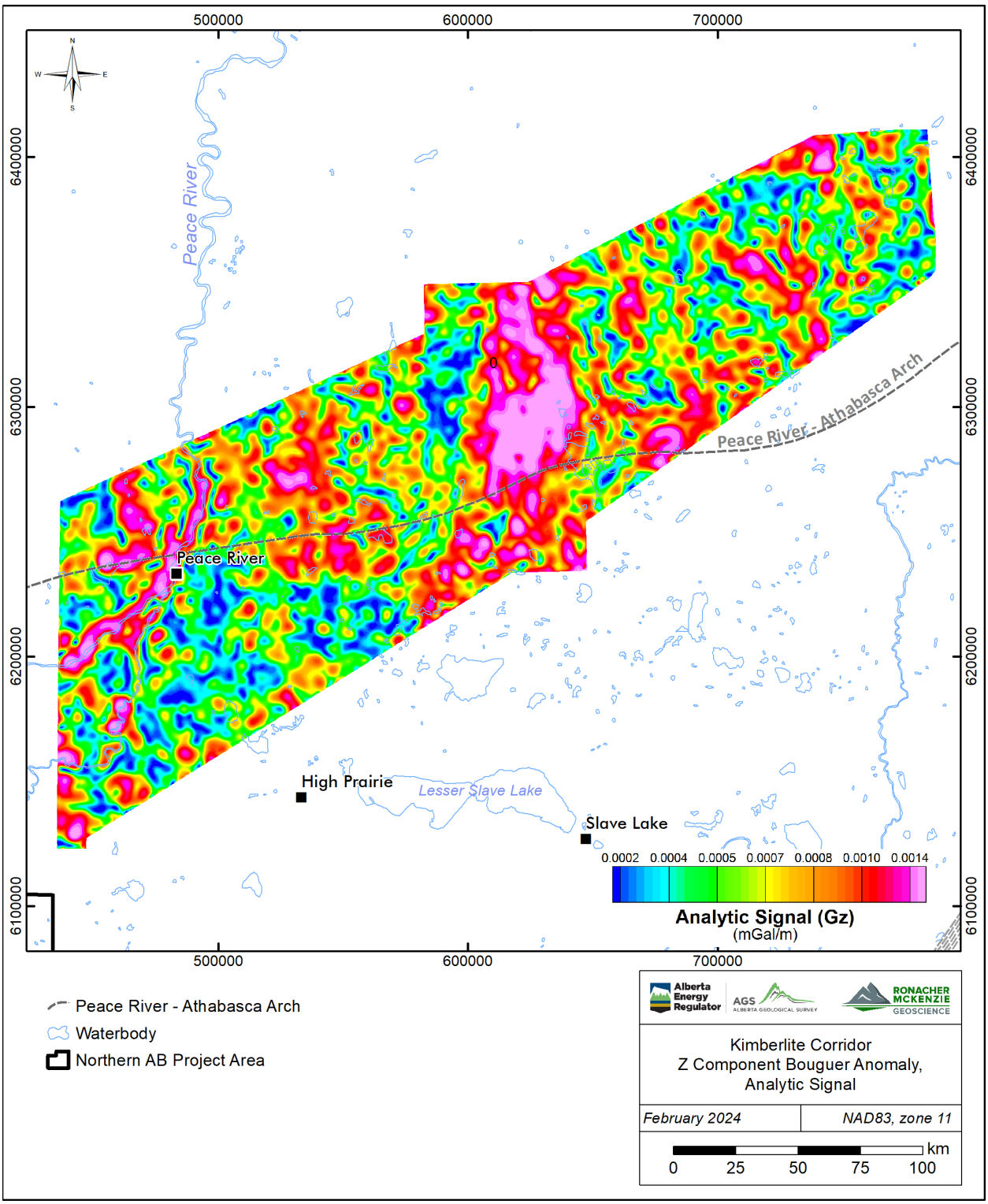

Figure 6-8. Kimberlite Corridor Analytic Signal (Gz).

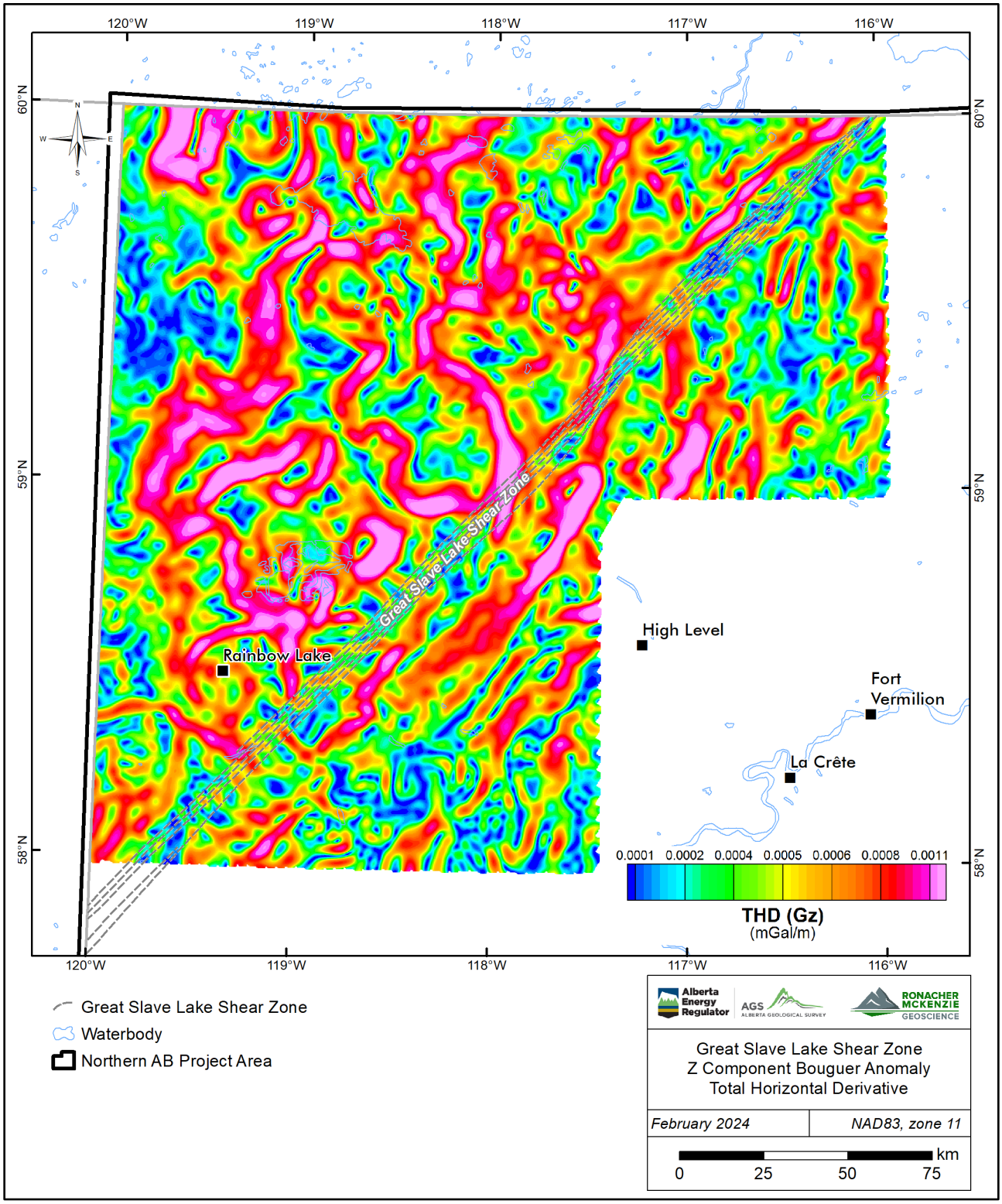

Figure 6-9. Great Slave Lake Shear Zone Total Horizontal Derivative (Gz).

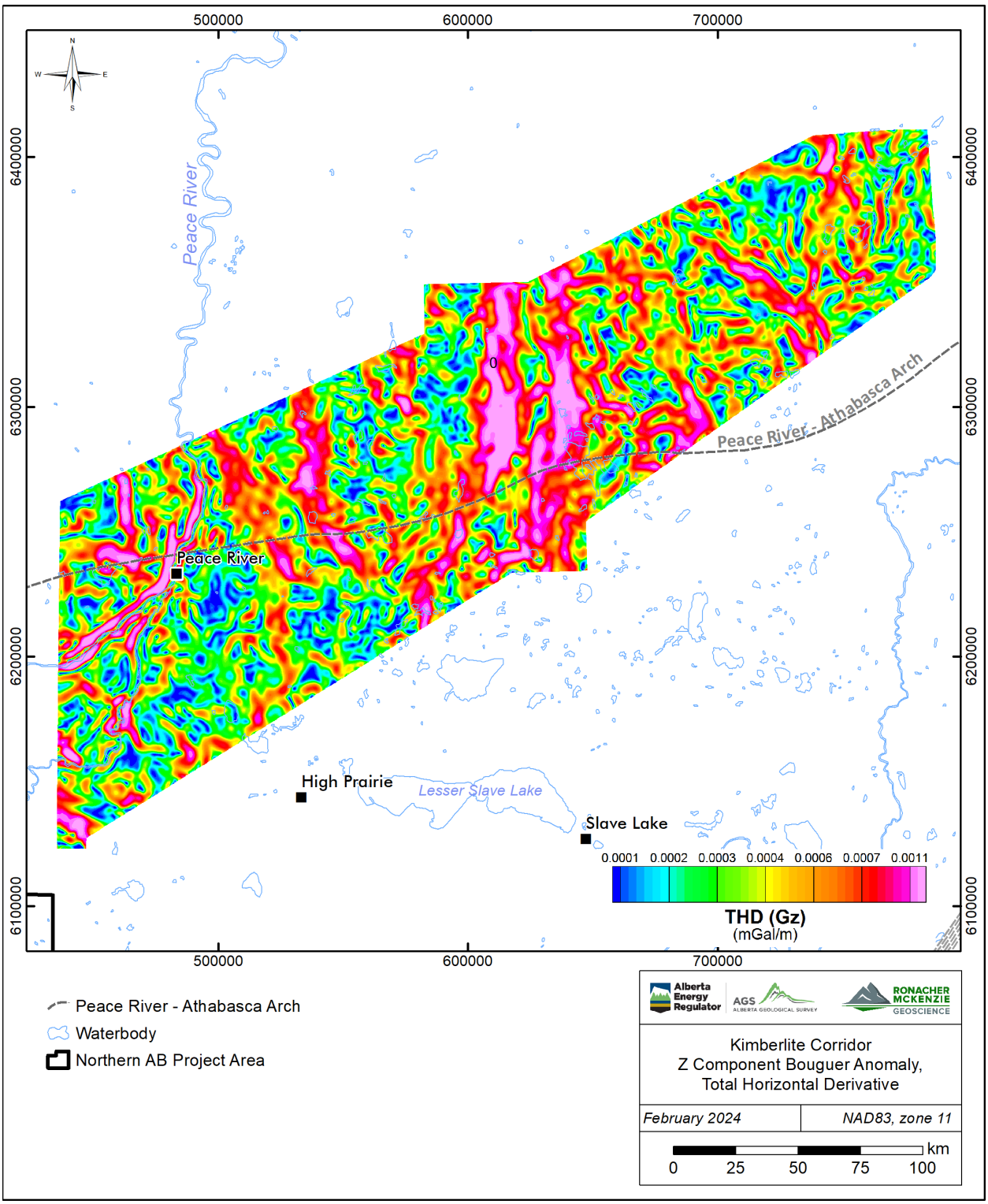

Figure 6-10. Kimberlite Corridor Total Horizontal Derivative (Gz).

The gridded data are also displayed using alternate colour distributions, to aid in data interpretation (Table 5-3). Different colour distributions are used to help identify structures in the interpretation process. For example, greyscale maps are useful for highlighting high and low areas while minimizing the effects of local amplitudes, and isoluminant palettes (e.g., CET i1 described in Kovesi 2015) mitigate artificial highlighting caused by perceived brighter colours in commonly used rainbow palettes, particularly in the yellow and green ranges.

Selected filter products are presented in Figure 6-11 through Figure 6-16. A complete set of georeferenced gridded data including alternate colour distributions is included in the Digital Appendix B delivered with this report.

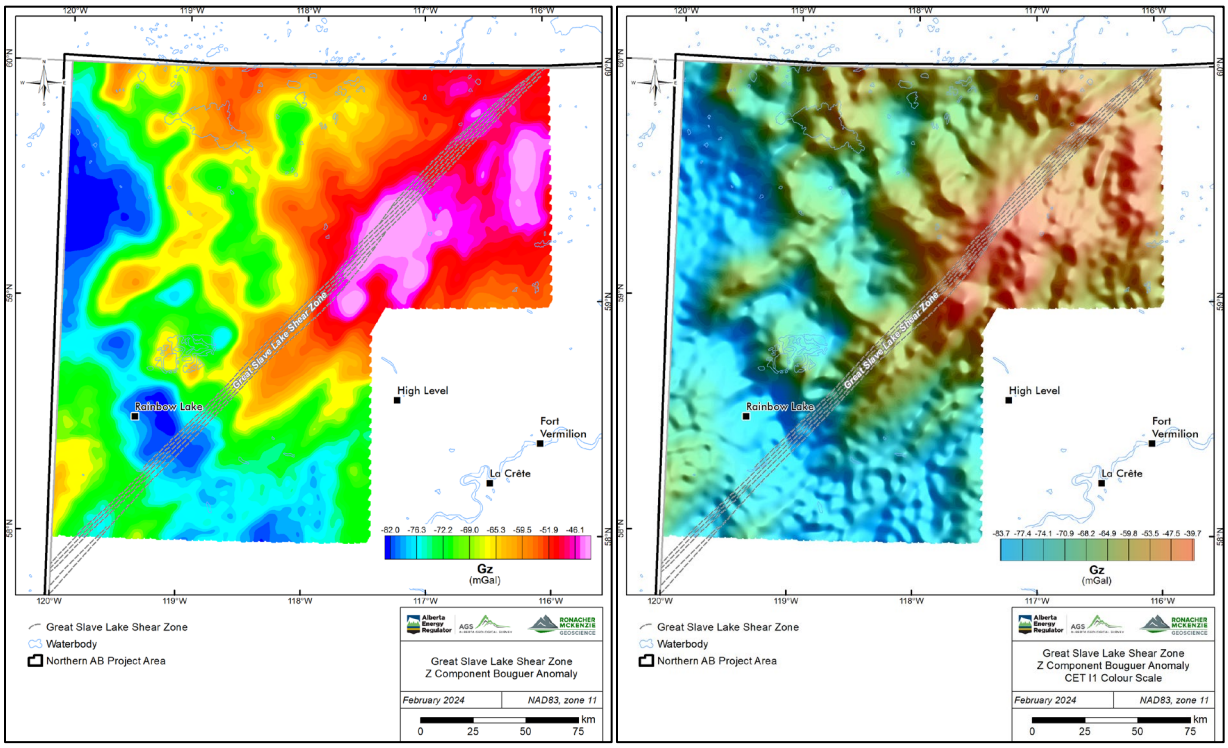

Figure 6-11. Great Slave Lake Shear Zone Bouguer anomaly (Gz), standard rainbow (left) and CET i1 isoluminant colour distributions.

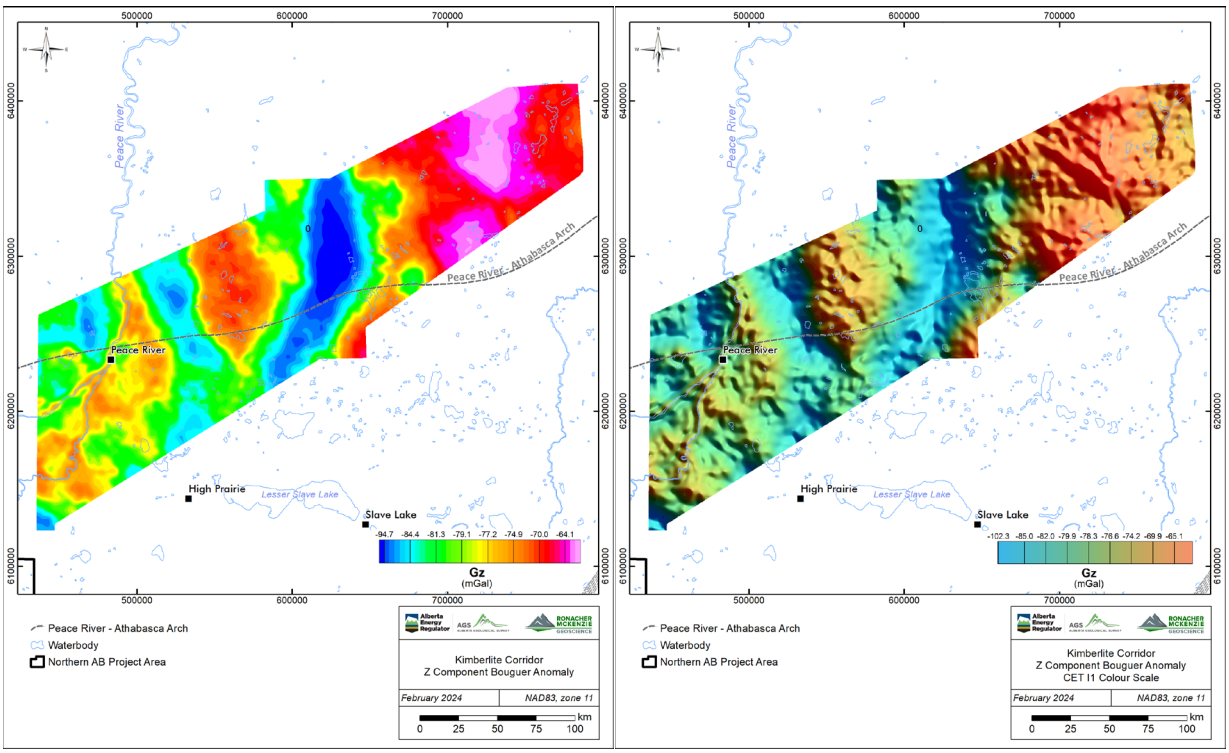

Figure 6-12. Kimberlite Corridor Bouguer anomaly (Gz), standard rainbow (left) and CET i1 isoluminant colour distributions.

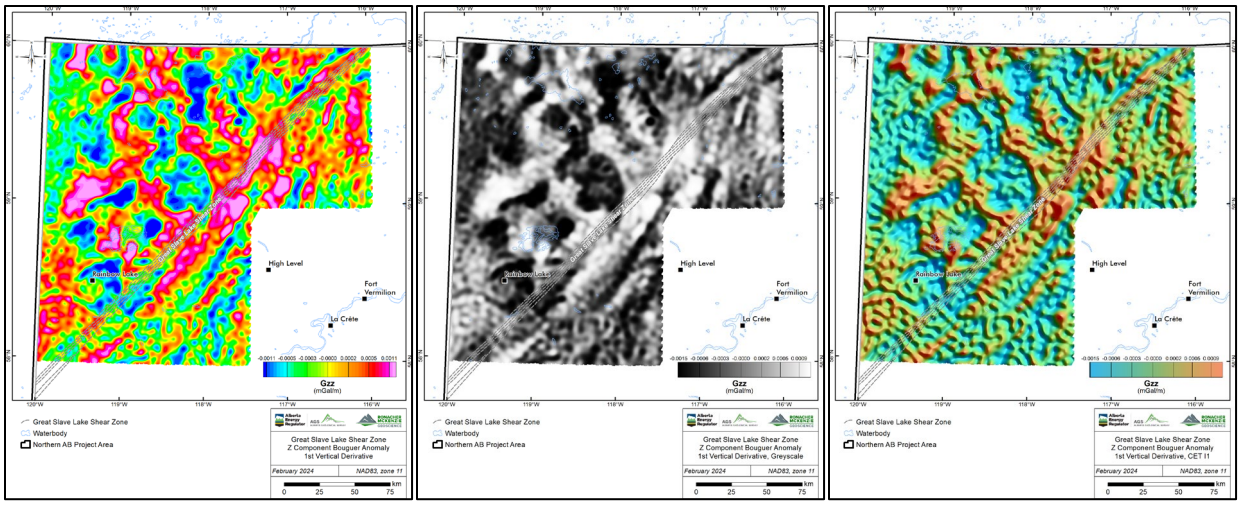

Figure 6-13. Great Slave Lake Shear Zone 1st vertical derivative (Gzz), standard rainbow (left), greyscale (centre) and CET i1 isoluminant (left) colour distributions.

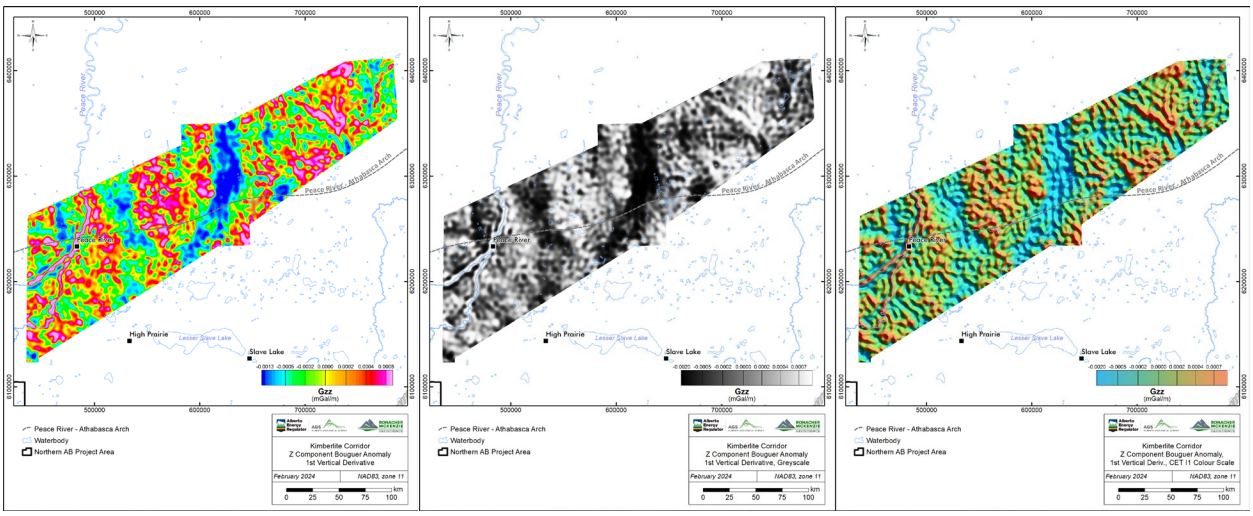

Figure 6-14. Kimberlite Corridor Zone 1st vertical derivative (Gzz), standard rainbow (left), greyscale (centre) and CET i1 isoluminant (left) colour distributions.

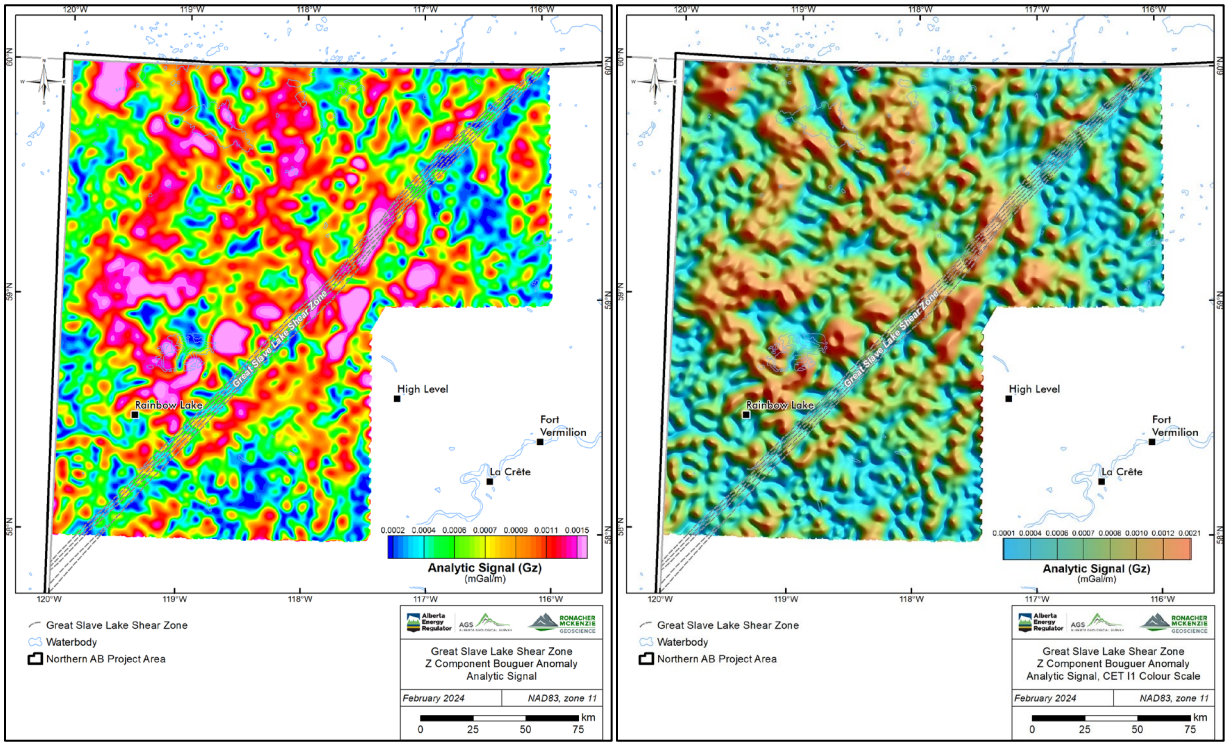

Figure 6-15. Great Slave Lake Shear Zone analytic signal (Gz), standard rainbow (left) and CET i1 isoluminant colour distributions.

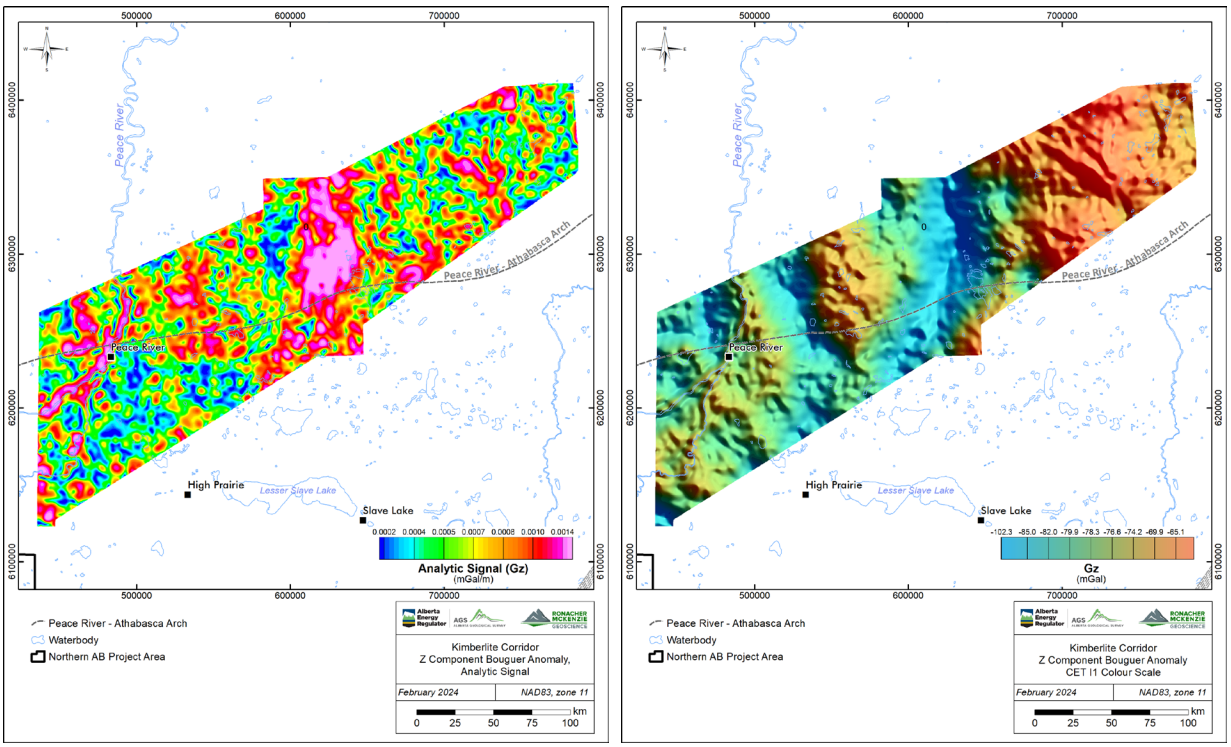

Figure 6-16. Kimberlite Corridor analytic signal (Gz), standard rainbow (left) and CET i1 isoluminant colour distributions.

7.0 METHODOLOGY

7.1 Overview

The airborne magnetic and gravity derivative and filter products (Sections 5.0 and 6.0) allow for new observations to be made and added to existing studies. Subsequent integration of specific elements allows for new insights in the subsurface in the region, which can steer structural interpretations, tectonic models, and subsurface exploration activities.

7.2 Workflow

The analysis follows the methodology developed by (Isles and Rankin, 2013), where the interpretation of aeromagnetic data process is broken down in three main stages: observations, integration, and interpretation. This method is also employed in the associated reports (Lopez et al., 2024; Brem et al., 2024). A similar approach is followed for the interpretation of gravity data.

The observation stage is focused on observing features directly from the aeromagnetic filter products (Appendix B) and automatic detection results (Appendix C). The interpreter records linear trends and discontinuities as form line features, and magnetic domains from the anomalies that cause them as polygons. Form lines may represent either stratigraphic or structural trends, and line breaks or juxtapositions may represent a structural element (e.g., fault, shear zone, unconformity or intrusive contact). This stage also includes the definition of domains that outline magnetic characteristics of different regions based on combined form line and magnetic rock unit observations.

The integration stage combines observations with existing geological and other types of data. This stage includes identification and definition of structural elements, magnetic domains, and changes or disruptions in domains with coherent structural or form line trends. Cross-referencing of the observations with other datasets, including Lithoprobe seismic (e.g., Ross et al., 1995; Ross and Eaton, 2002) , geology (e.g., Pană, 2003, 2010; Okulitch, 2006; and Prior et al., 2013), geochronology (Ross et al., 1991; Villeneuve et al., 1993; Burwash et al., 1994; Burwash et al., 2000; and Pană, 2010), and structural lineament compilations (e.g., Pană et al., 2001; Pană and Waters, 2016; and Pană et al., 2021) were done in this stage.

The interpretation stage involves the revision or creation of a structural framework that includes inferences of structural and lithotectonic history. This is the final step in generating an integrated geologic and geophysical interpretation of an area to present a final geological interpretation map. The compilation of the domains and structure layers is the basis of the structural framework interpretation.

7.3 Brittle faults and ductile shear zones

High-pass filter products such as second derivative, tilt, and automatic gain control, and the results for short wavelengths from the structure automatic detection for cross structures were used to emphasize shallow and detailed brittle structures in the project area. Criteria to identify brittle structures included the following:

- juxtaposition of different form line orientations.
- linear features, with angular margins.
- angular fault jogs or steps.
- short subtle curvilinear linear features (for sub-horizontal sedimentary strata).
- narrow zones of demagnetization (due to low temperature oxidation of magnetic minerals).
- offsets of magnetic rock units.

Offsets and sense of movement were recorded in the accompanying GIS vector files where possible. Because of the 2D plan nature of aeromagnetic data, interpreted offsets are apparent offsets.

Filters such as vertical and horizontal derivatives and tilt angle (tilt derivative) combined with results from the structure detection for parallel structures completed by Fathom Geophysics were used to identify deeper basin structure and shear zones. The wavelength separation results, particularly the separation of long wavelengths, allows for the interpretation of deeper structure. Furthermore, differential upward continuation magnetic products were useful for discriminating deeper from shallower structures Figure 5-11 and Figure 5-12.

Shear zones in the project area are characterized by the following:

- broad zones of anastomosing surfaces, with curvilinear margins.
- bending of magnetic units or contacts into the shear zone.
- magnetic mineral alteration that may be destructive, additive, or both; or
- offsets of units associated with deflection or thinning of magnetic markers as they enter the shear zone.

8.0 INTERPRETATION AND RESULTS

8.1 Cultural Artefacts

Northern Alberta is a populated region, including widely distributed infrastructure associated with the oil and gas industry, and cities and towns, such as Grande Prairie, Fort McMurray, and Peace River. The survey contractor applied filtering and manual editing to attenuate the effects of culture in the data, but cultural artefacts are still present throughout the survey area. The following cultural features were evaluated against the aeromagnetic images: (1) municipal areas, (2) railways, (3) pipelines, and (4) oil and gas related infrastructure. As these features are all near surface, expected signatures include small wavelength anomalies and/or distortion of larger magnetic anomalies.

The area of Ft McMurray presents regional high amplitude and high frequency elongated magnetic features in which oil sands infrastructure does not interrupt the regional magnetic fabric and therefore, the impact of culture appears minimal (Figure 8-1). In contrast, the area around the town of Peace River presents a general moderate to low amplitude magnetic signature with local high-amplitude and high-frequency rounded anomalies, some of them related to industrial sites or oil and gas facilities (e.g., gathering stations or processing plants). These anomalies may be misinterpreted as small intrusions if they are not correlated with infrastructure vector files or imagery (Figure 8-2). Numerous small (< 5 km^2) rounded anomalies are present throughout the project area that are cultural in nature. Some small anomalies are not overlain by any cultural feature; for these, a geologic explanation should be sought.

The regional railroad and powerlines networks do not show on any of the aeromagnetic images. The impact of these cultural components is considered negligible.

Finally, pipelines do not represent a major challenge in the interpretation of the magnetic images, except in the west of the project area where the magnetic intensity variations are lower. Most pipelines do not show a magnetic signature, most likely due to survey filtering completed by the survey contractor. Where there is a pipeline expression, it usually occurs locally in zones of low magnetic intensity and appearing as subtle straight or wiggly lineaments (Figure 8-3). Overall, the impact of pipelines on the aeromagnetic image is moderate in the west and low in the rest of the project area. Calibration of lineaments with cultural vector files and imagery is still recommended.

In summary, there are numerous interference patterns on the aeromagnetic images of which the most impactful are high frequency rounded anomalies. Many such anomalies correspond to some sort of industrial site, but some represent geological features. It is recommended that smaller rounded magnetic anomalies are carefully evaluated and calibrated with cultural data on a case-by-case basis.

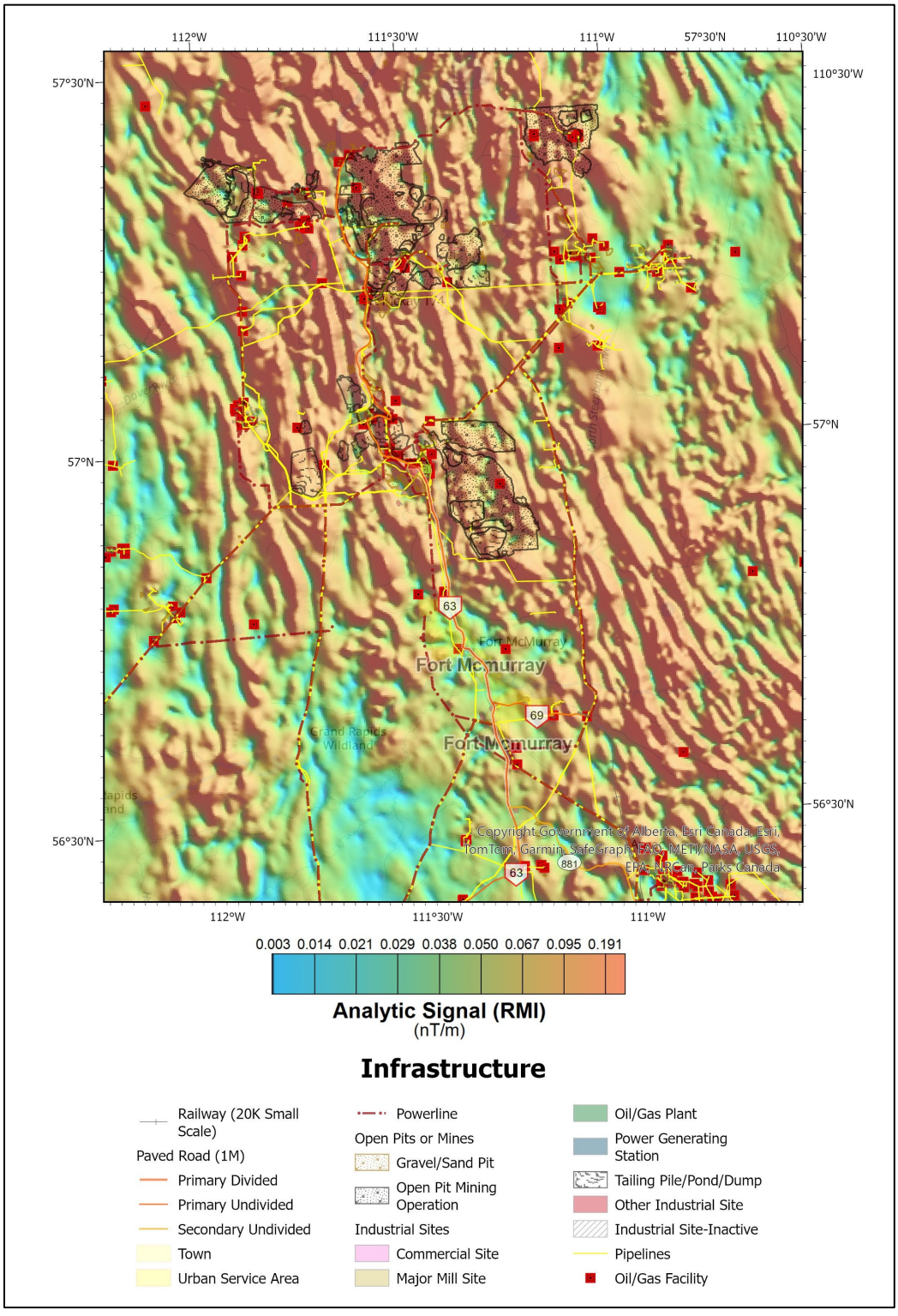

Figure 8-1. Impacts of infrastructure (urban, utility, access, and oil sand mines, facilities and pipelines) of the Ft. McMurray area on magnetic images.

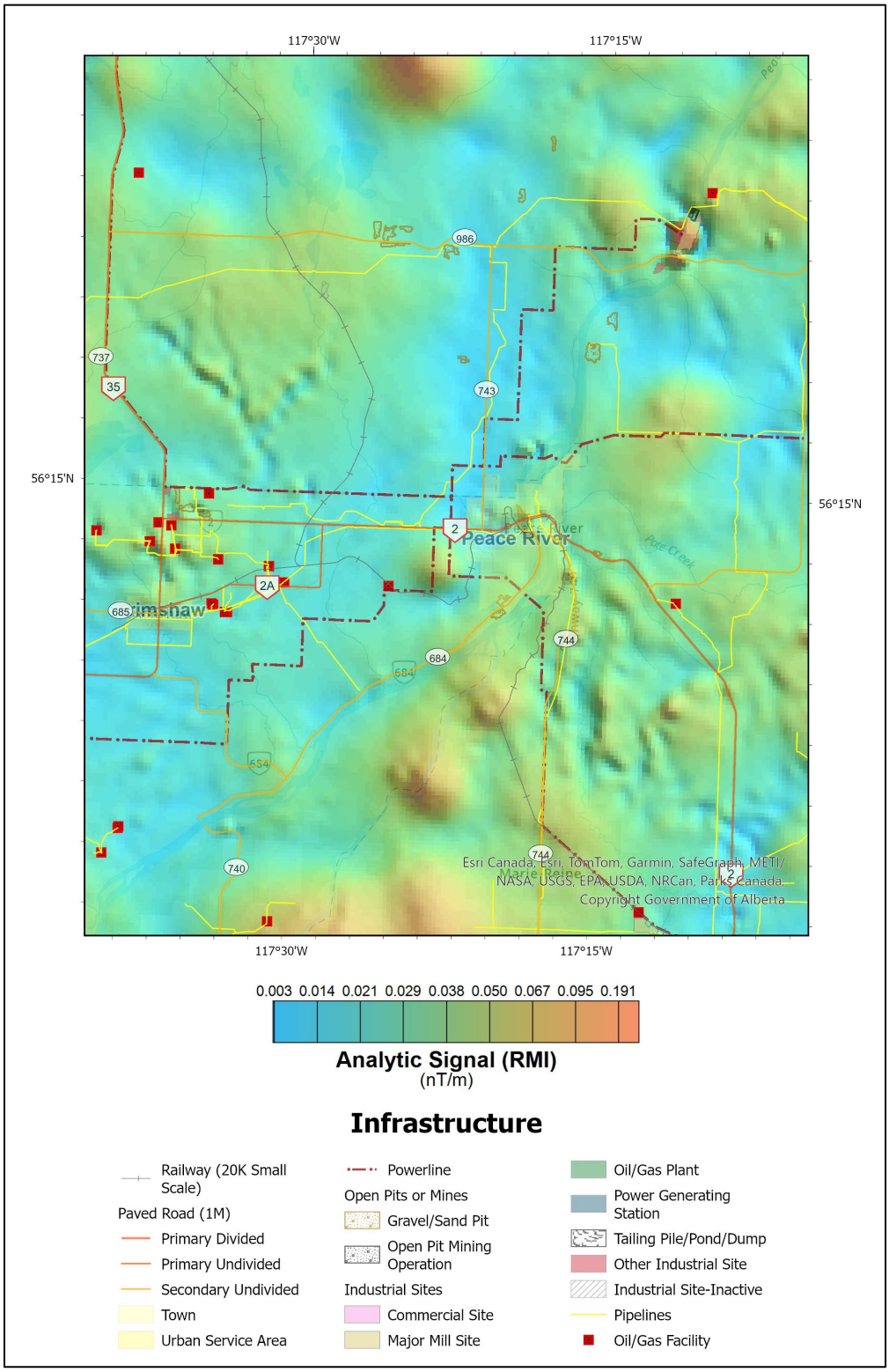

Figure 8-2. Impacts of infrastructure (urban, utility, access, pipelines, and industrial facilities) of the Peace River area on magnetic images.

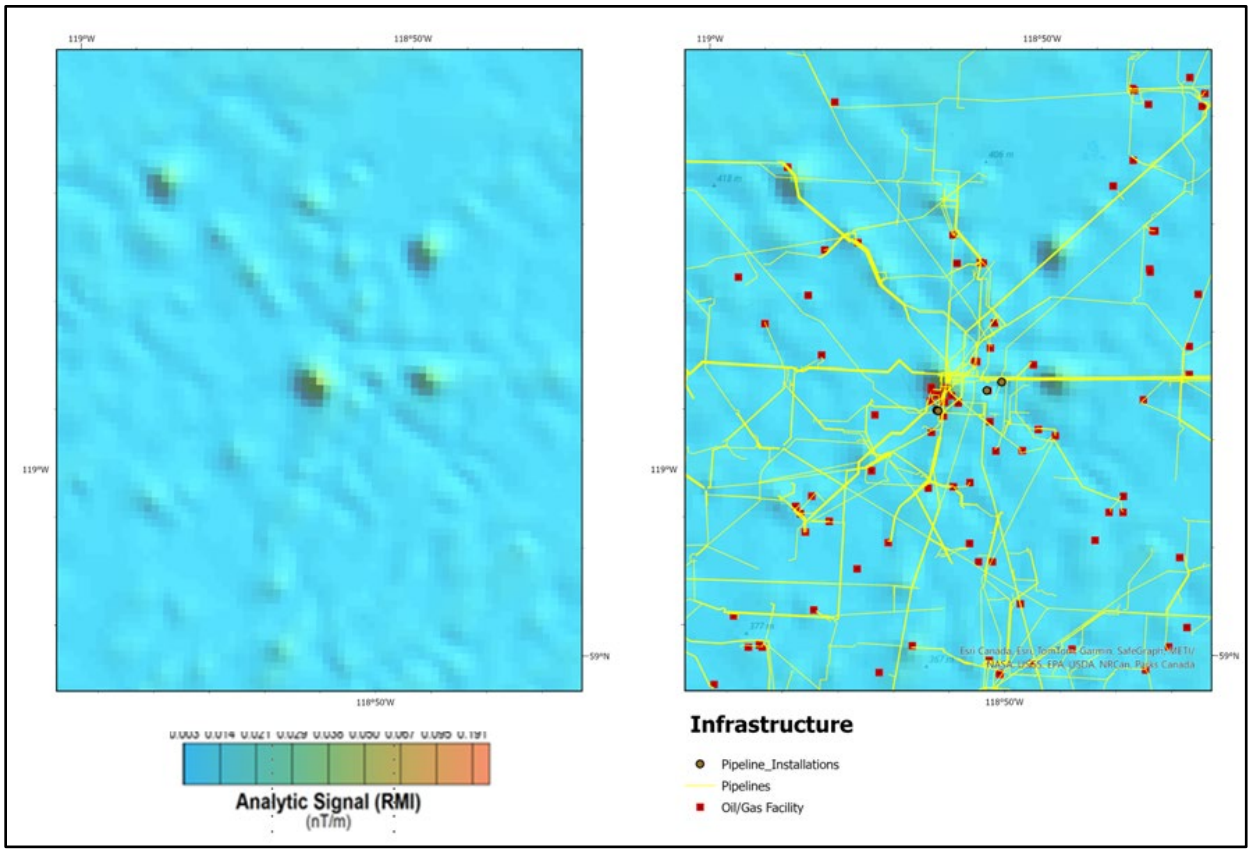

Figure 8-3. Illustration of the impact of pipelines and pipelines installation sites on aeromagnetic images.

8.2 Domain Boundaries

The interpretation of the magnetic and gravity derivative and filter products conducted for the project area resulted in the modification of published domain boundaries. Many modifications are minor adjustments to the original boundary due to the higher quality of the data, whereas some other modifications are significant and involve a major relocation of a domain boundary.

The reduced to pole residual magnetic intensity, analytic signal, first vertical derivative, total horizontal derivative, and ternary magnetic images that highlight geological affinity, for example pseudo-geology (Figure 5-9) and pseudogravity (Appendix 1 page 31), are used to outline domains and subdomains. Existing domain interpretations are used to identify and classify domains and subdomains in the interpretation. In particular, the tectonic domains defined by Ross et al (1994; Figure 4-2) and Pilkington et al (2000; Figure 4-3) are used as a main guide to identify and correlate tectonic domains in our interpretation. Classification follows known domains wherever possible, whereas subdomains are defined here for the first time. Boundaries between subdomains are not necessarily tectonic in nature as they represent an internal magnetic variant within a known tectonic domain. The geophysical and chronological characteristics of the interpreted domains and subdomains are tabulated (Table 8-1).

The boundaries of tectonic domains defined by Ross et al (1994) and Pilkington et al. (2000) were slightly modified and these are shown on Figure 8-4 and Figure 8-5. Furthermore, these tectonic domains were divided into subdomains based on distinct magnetic character within certain domains (Figure 8-6 and *Figure 8-7*). Subdomains may be related to primary heterogeneous magnetic fabric or secondary geologic processes that create, introduce, or destroy magnetic minerals.

The most relevant changes to domain boundaries include:

- Minor adjustments were made to the following domain boundaries: Hottah, Great Bear, Nova, Kiskatinaw, Chinchaga, Rae, Wabamun, Thorsby, Rimbey and Loverna.

- A small subdomain, called Hottah/Great Bear subdomain, was identified between the Hottah and Great Bear domains because it was possible to distinguish overlapping characteristics of these two domains in the Hottah/Great Bear subdomain. It is suspected that the Great Bear magmatic imprint is built over the Hottah terrane in this region.

- Two small subdomains labeled as unknown were identified. In the northwest, a north-trending domain of distinct fabric is interpreted between Chinchaga and Buffalo Head domains. This subdomain could represent an internal variation within the Chinchaga domain, or a separate terrane between Chinchaga and Buffalo Head domains. In the southwest, the Chinchaga domain displays a second variation distinct from the overall character of this domain.

- Redefinition of the boundary between the Buffalo Head domain and the Taltson Magmatic Zone ("Taltson") (Figure 8-4 and Figure 8-5), and new subdivisions within both domains (Figure 8-6 and Figure 8-7; Table 8-1).

- Major modifications of the outline of the Buffalo Head domain of Ross et al. (1994), and Buffalo High and Buffalo Utikuma domains of Pilkington et al. (2000). Variations in magnetic character allow the interpretation of contrasting subdomains ((Figure 8-6 and Figure 8-7). Pilkington's Buffalo High and Buffalo Utikuma domains are considered as subdomains of Buffalo Head domain in this report. The Buffalo Head domain was subdivided into six subdomains based on magnetic amplitude, general trend, and internal character in relation to the surrounding units (Table 8-1). The newly defined Buffalo Central subdomain is a major N-trending unit along the western margin of the original Buffalo Utikuma domain of Pilkington et al (2000); thus, the extension of the original Buffalo Utikuma subdomain was reduced. The Buffalo Central subdomain separates the Buffalo High from the Utikuma subdomains, displaying either structural or fuzzy irregular contacts with these domains. It coincides with a known N-trending Trout Mountain gravity low (e.g., Eccles et al., 2002) and shows evidence of remanence throughout (Figure 8-7).

- Major modifications of the outline and extensive subdivision were conducted for the Taltson domain. The Taltson domain was subdivided into nine subdomains based on variations in magnetic amplitude, general trend, and internal character in relation to the surrounding units. The Taltson subdomains

(Taltson Charles Lake, Taltson Athabasca, and Taltson Birch) display penetrative linear fabric related to shearing that ranges in direction from NNW to NE. The Taltson Slave, Taltson Arch Lake, Taltson Wood Buffalo, and Taltson South subdomains display limited to weakly defined fabric as follows. ((Figure 8-6 and Figure 8-7).

- ❖ The Taltson Slave subdomain lacks linear trends (except locally), whereas Arch Lake is dominated by general E and N-trending linear fabrics (Table 8-1). The Taltson's Slave and Arch Lake subdomains contain collision-related, peraluminous (S-type) Slave (1934 Ga; McDonough et al., 2000)) and Arch Lake (1938 Ga; McDonough et al., 2000) igneous complexes described in Pană (2010).

- ❖ The Taltson's Wood Buffalo subdomain displays weakly defined linear N trends of its wide form lines, and it is affected by E- to ENE-trending brittle faults (Table 8-1). The fabric resembles a rift structure, with a general N-trending ridge and perpendicular transform and fracture zones. This structure may represent either a remnant rift basin or more probably an intra-arc rift in the TMZ.

- ❖ The Taltson/Rae subdomain lacks linear trends (except at the boundary with Rae domain) and presents characteristics of both Taltson and Rae domains, such as the low magnetic intensity of Rae domain and internal fabric of Taltson's intrusion complexes. The Taltson/Rae subdomain contains 1.974–1.959 Ga, subduction-related, weakly peraluminous to metaluminous (I-type) intrusion complexes described in Pană (2010).

- ❖ The Taltson South subdomain displays a dominant EW-trending refolding fabric (Figure 8-6; Table 8-1), is bound by major shear zones in the north and west, and aligns with the Thorsby and STZ in the south. Either the Taltson South subdomain is a refolded Taltson block affected by the adjacent STZ or it belongs to a possibly Archean terrain.

- The outline of the "uncertain" subdomain defined by Pilkington et al. (2000) of Figure 4-3 was redrawn and subdivided into four small subdomains based on magnetic amplitude, general trend, and internal character in relation to the surrounding units. These subdomains were all labeled as unknown, and they appear to represent broken deformed pieces of adjacent domains, possibly from the Wabamun domain ((Figure 8-6 and Figure 8-7).

According to Pilkington et al. (2000), the Thorsby and Kiskatinaw narrow low magnetic domains may be the result of demagnetization due to deformation and metamorphism during terrane collision, whereas the wider Chinchaga and Hottah domains' low magnetic intensity may result from originally less magnetic metasedimentary or volcanic rocks. Metasedimentary or volcanic lithologies might be the magnetic source in the Chinchaga domain, however all basement samples from cored oil wells in the Hottah domain (n=10) correspond to mafic, intermediate or felsic intrusions, suggesting that the low magnetization might be the result of demagnetization. Similarly, the Buffalo Low subdomain shows dominantly low magnetic intensity that can

be interpreted as an originally metasedimentary or volcanic terrane. The Rae Craton is also characterized by magnetic lows and displays a penetrative high-frequency linear (layered?) fabric that has been sheared and folded, suggesting a basement consisting of metasedimentary rocks.

The magnetic characteristics of the Buffalo Arch subdomain are similar to both the Ksituan and Rimbey domains of Pilkington et al. (2000), and therefore the Buffalo Arch subdomain is interpreted here as a possible magmatic arc at the boundary of the Buffalo High and Buffalo Low subdomains with the Chinchaga Domain.

In summary, the higher quality of the new magnetic data and its products allow for the definition of subdomains within known tectonic domains. Reduction of uncertainties to resolve the architecture of the crystalline basement requires further integration with available geological, petrological, chronological, and magnetic susceptibility data.

The GIS files containing the outlines and details of the new interpreted lithotectonic domains and subdomains are included in the Digital Appendix A.

Figure 8-4. Interpreted domain boundaries in northern Alberta modified from Pilkington et al. (2000). Background image: pseudo-geology ternary.

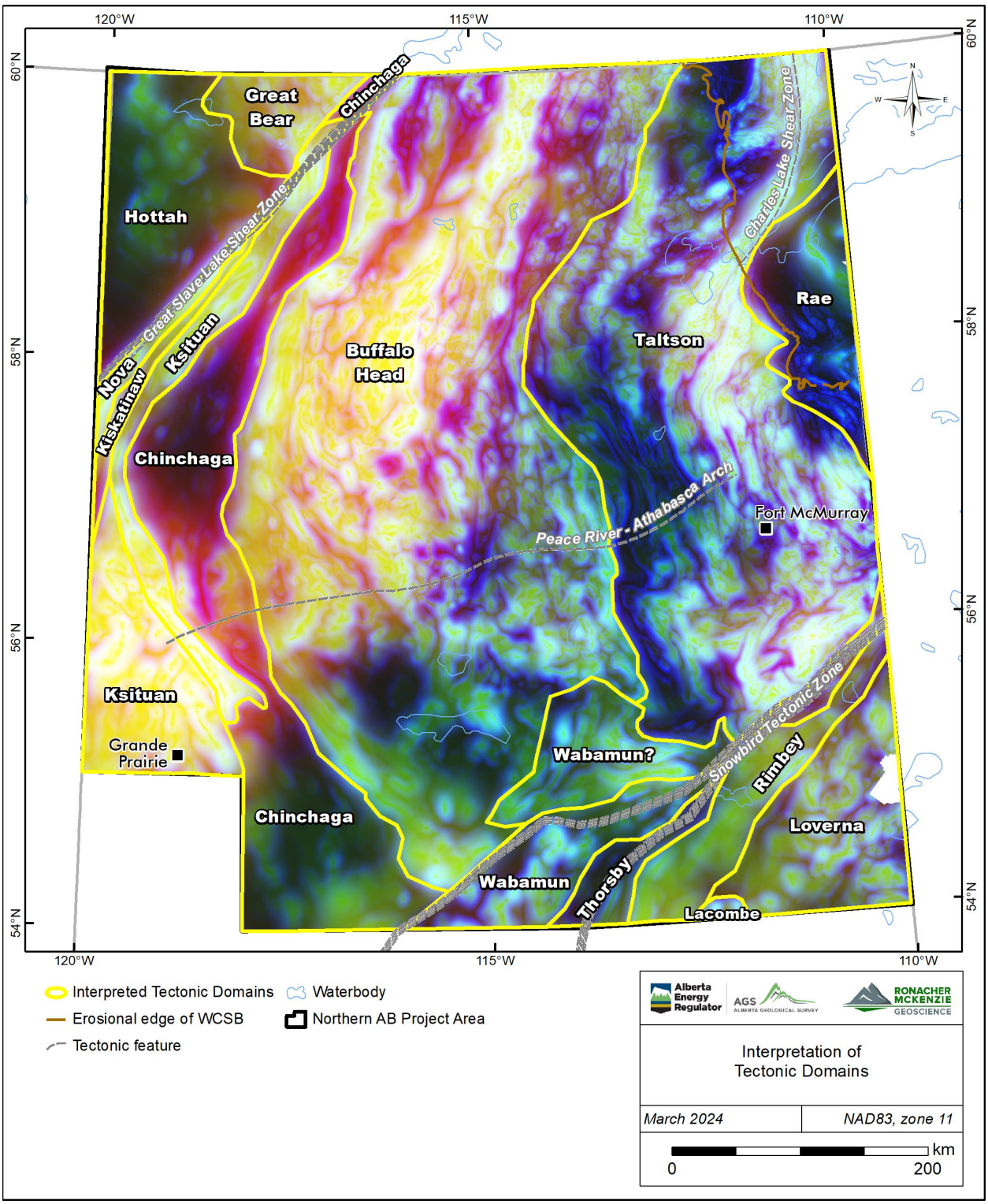

Figure 8-5. Interpreted domain boundaries in northern Alberta modified from Pilkington et al. (2000). Background image: pseudo-gravity ternary by Fathom Geophysics.

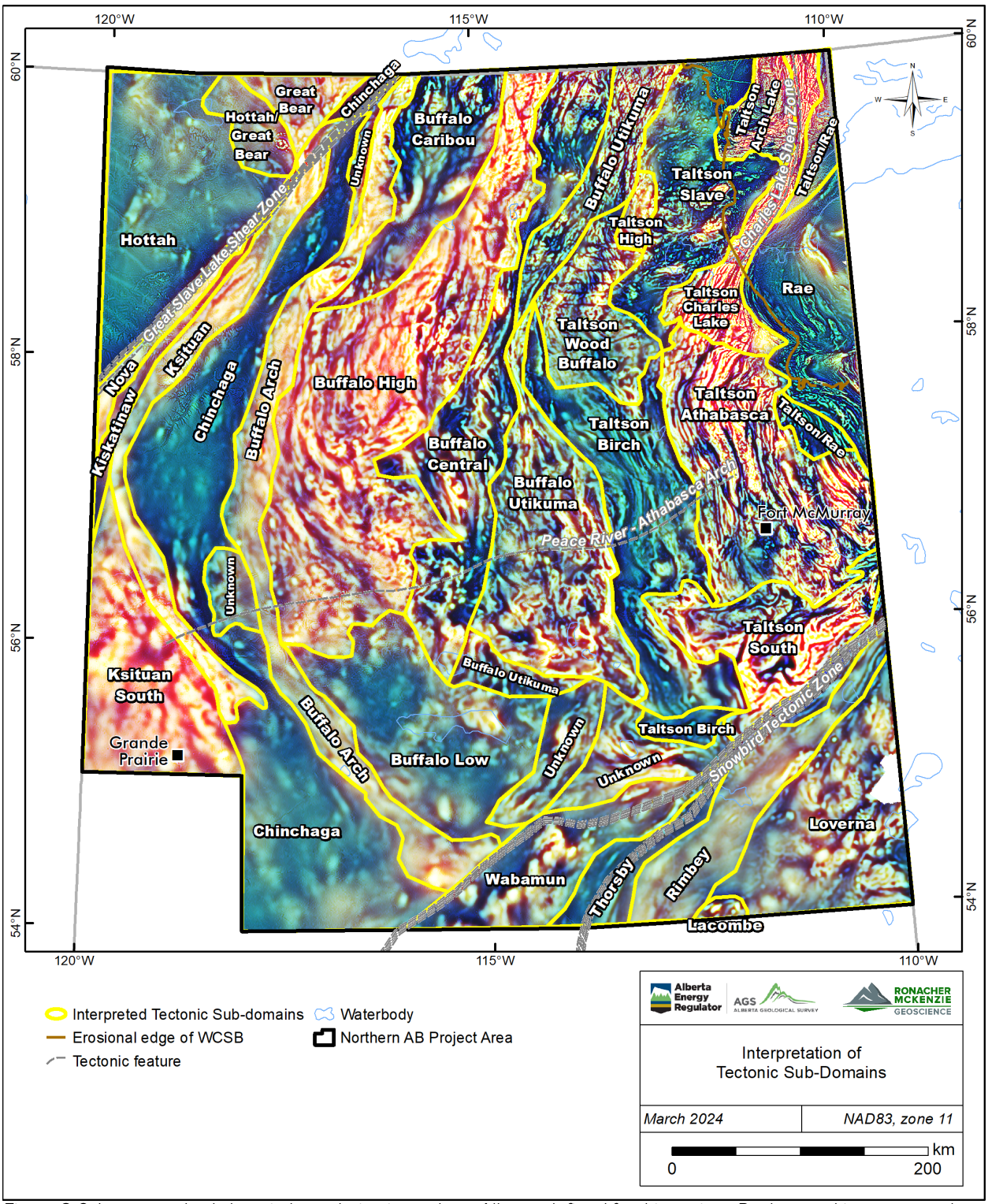

Figure 8-6. Interpreted subdomain boundaries in northern Alberta defined for this project. Background image: pseudo-geology ternary.

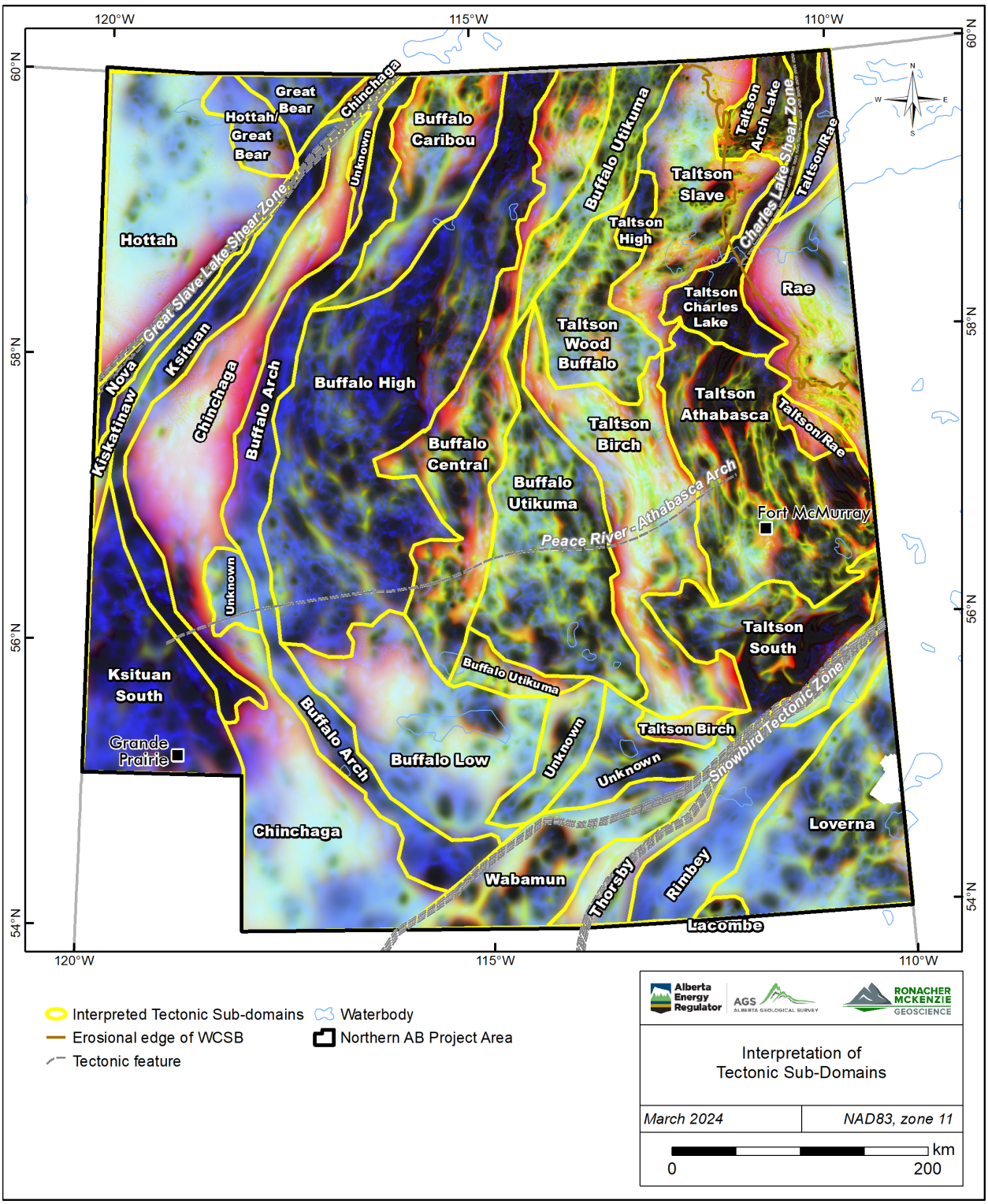

Figure 8-7. Interpreted subdomain boundaries in northern Alberta defined for this project. Background image: ternary of RTP, analytic signal of vertical integral, and analytic signal by Fathom Geophysics. Red colour indicates areas most affected by magnetic remanence.

Table 8-1 Characteristics of basement subdomains defined in this work.

Domain[1]	Subdomain[2]	Age (Ga)[3]	Type[4]	Amplitude	General Trend	Magnetic character
Hottah		1.8–1.9	Proterozoic accreted terrane	Moderate	NW	Few broad subcircular anomalies, locally grainy with high frequency subcircular moderate anomalies. High frequency broadly spaced NW linear trends.
Great Bear	Great Bear		Continental magmatic arc	Variable, moderate to low	NNW	Broad NNW trends.
	Hottah/Great Bear		Hottah overprinted by Great Bear	Moderate	NW and NNW	Broad NNW and NW trends, grainy with high frequency subcircular moderate anomalies.
Nova		2.0–2.8	Archean	High	NE	Elongate NNE trends.
Kiskatinaw		1.9–2.0	?	Low	None	Few broad subcircular to oblate anomalies, locally grainy.
Ksituan	Ksituan	1.9–2.0	Continental magmatic arc	High	NW to NE	N to NE trends in north, broad amplitude NW trend in the south.
	Ksituan South	1.9–2.0	Continental magmatic arc	Variable, high to low	NW and NE	Subcircular and NW elongate anomalies.
Chinchaga	Chinchaga	2.1–2.2	Proterozoic accreted terrane	Variable, moderate to low	NW to NNE	NW to NNE low-amplitude trends.
Buffalo Head	Buffalo Arch	2.0–2.3	Magmatic arc?	High	NW to NNE	Broad NW to NNE trends and locally without linear trends.
	Buffalo Caribou		Subdomain of Proterozoic accreted terrane	Variable, moderate to low	NNW to NNE	Variable amplitude and frequency signature. N to NNW linear high frequency trends.
	Buffalo Central		Subdomain of Proterozoic accreted terrane	Variable, high to low	NNW to NNE	Variable grain. NW to NNW trends in the south, NW to NNE trends in the north. Some subcircular and oblate anomalies. Several zones of remanence.
	Buffalo High[1]	2.0–2.7	Subdomain of Proterozoic accreted terrane	High	NW to NNE	Three subregions: NW linear trends in the southwest, blocky N-NNW trends in the center, subangular NNE trends in the east with EW-trending brittle faults.
	Buffalo Low	2.3–2.8	Subdomain of Proterozoic accreted terrane	Variable, moderate to low	None	Subcircular anomalies and few NW trends near boundaries.
	Buffalo Utikuma[1]	2.0–2.6	Subdomain of Proterozoic accreted terrane	Variable, high to moderate	None, NNW	Variable grain; weakly elongate NNW trends in south, lineated NNE trends in the north.
Taltson	Taltson Arch Lake	1.9	Continental magmatic arc	Variable, very high to low	EW and NNE	Oblate to linear EW trends in the south, and N to NNE linear trends in the north and edges.
	Taltson Athabasca	1.9-2.7	Continental magmatic arc	Variable, high to low	NNW to NE	Strong curvilinear high-amplitude and anastomosing NNW to NNE linear trends.
	Taltson Birch	1.9-2.7	Continental magmatic arc	Variable, high to low	NNW	Strong curvilinear low-amplitude and anastomosing NW- N -NNW linear trends. Zones of remanence.
	Taltson Charles Lake		Continental magmatic arc	Variable, very high to low	NE to NNE	Strong anastomosing NE to NNE linear trends.
	Taltson High		Continental magmatic arc	High	None	Broad anomaly. No linear trends.

Domain[1]	Subdomain[2]	Age (Ga)[3]	Type[4]	Amplitude	General Trend	Magnetic character
	Taltson South	1.9-2.8	Continental magmatic arc	Variable, very high to low	EW to WSW	Refolded fabric with folds trending from ENE - NE.
	Taltson Slave	1.9	Continental magmatic arc	Variable, moderate to low	None	Strong and significant number of subcircular anomalies in the south. Less subcircular anomalies and local N linear trends.
	Taltson Wood Buffalo		Continental magmatic arc	Variable, high to low	NNW	Broad NNW to N linear trends, crosscut by EW-trending brittle faults. Better defined NNW trends in the north.
	Taltson/Rae	1.9	Continental magmatic arc	Low to moderate	None	Grainy with subcircular moderate anomalies, and broad NE trends at boundary with Rae domain.
Rae			Archean	Variable, high to low	NW to NE	Strong parallel high frequency linear trends, two subregions: tight folded in the south with fold trending NW and linear trends curving from NW to NNE trends in the north.
Rimbey		1.8	Continental magmatic arc	Moderate	NE	Subcircular anomalies and few NE trends at boundaries.
Thorsby		1.9–2.4	Remnant of Proterozoic oceanic lithosphere	Low	NE	Strong parallel NE trends curving to the NNE in south boundaries.
Wabamun		2.3	Proterozoic accreted terrane	Variable, high to low	None	Strong subcircular anomalies. No linear trends.
Loverna		1.8–2.7	Archean	Variable, high to low	None	Subcircular anomalies and few NE trends.

1. *Domain name after Ross et al (1994) and Pilkington et al (2000)*
2. *This work*
3. *Ages by Ross et al. (1991), Villeneuve et al. (1993), Burwash et al (1994), and Pana (2010)*
4. *Type from structural elements compilation file downloaded from web application indicated in Pană et al. (2021).*

8.3 Magnetic fabric orientation of domains and relation to the Peace River Arch

The orientation of the magnetic fabric defined by form lines was determined by Fathom Geophysics by enhancing (with automatic gain control) the pole reduced residual magnetic intensity and applying an anisotropic diffusion filter to highlight linear features (Appendix 1). The resulting orientations were interpolated and smoothed to generate the image shown in Figure 8-8. Magnetic fabric orientation of the project area. The known Peace River Arch trend coincides with the trend of the central area dominated by NW to NNW trends (green and red colours).. On this image, the green areas are dominated by WNW to NW trends; the blue and cyan areas are dominated by ENE trends; the magenta indicates NNE trends and the red and orange areas are dominated by NNW to N-trends.

The result of the magnetic fabric orientation shows three main regions with different dominant fabric orientations (Figure 8-8). The north and south regions are dominated by NNE to ENE trends represented by magenta, blue and cyan colours. In contrast, the central area of the image shows a magnetic fabric orientation dominated by WNW to NNW trends represented by green, red and orange colours. This central area coincides with the location of the PRA.

Historically, no apparent ENE-trending linear features in the basement had been reported to coincide with the location of the PRA, which led previous studies to conclude that the arch uplift had no relation with the crystalline basement. However, the resulting magnetic fabric image (Figure 8-8) suggests that either the PRA does have a relationship with Precambrian basement domains or that the Carboniferous NW-trending grabens in the WCSB dominate over the Precambrian fabric. Nevertheless, the higher magnetic susceptibility of crystalline basement relative to sedimentary rocks makes the hypothesis of the relationship of PRA with the basement the most plausible source of the dominant WNW to NNW orientation fabric in the PRA area.

After a detailed examination of the internal magnetic fabric of basement subdomains, it is observed that most of the standard magnetic products do display changes in fabric orientation coincident with the fabric orientation image. For example, form lines observed on Figure 8-4 to Figure 8-7, curve from a predominantly WNW, NW and NNW orientation in the south to a predominantly NNE to NE orientation in the north of the project area. This orientation change occurs for the Ksituan, Chinchaga, Buffalo Head and Taltson domains, including their subdomains. The line formed by the inflection points where the magnetic fabric changes dominantly from WNW-NW to NNW-N trends, given by green and red-orange colours respectively, coincides with the known axis of the PRA of Pană et al (2021). The coincident PRA axis with a curvature axis of the crystalline basement fabric implies that the PRA uplift was superimposed upon a pre-existing Precambrian basement geology (Figure 8-8).

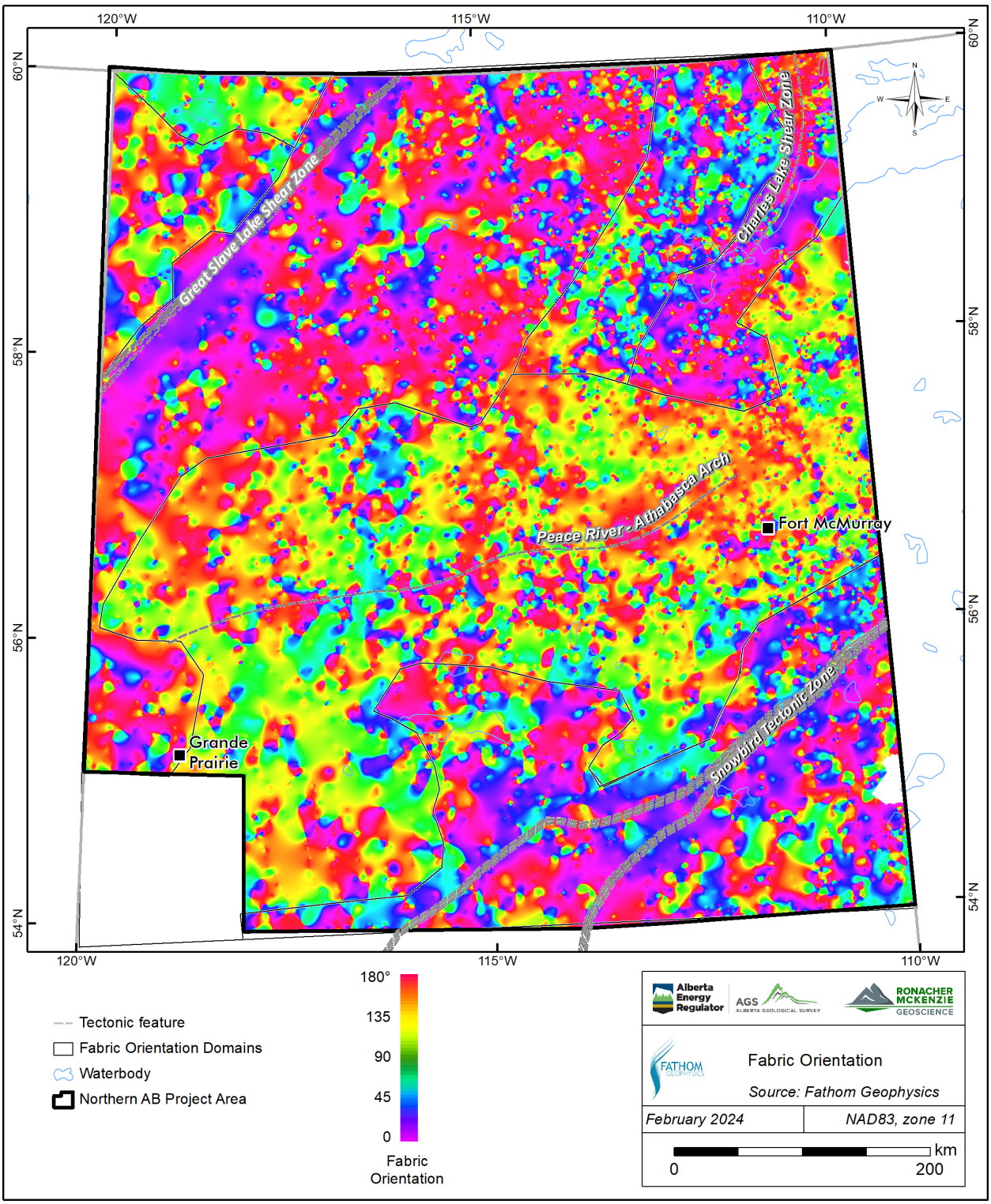

Figure 8-8. Magnetic fabric orientation of the project area. The known Peace River Arch trend coincides with the trend of the central area dominated by NW to NNW trends (green and red colours).

8.4 Lineaments, Faults and Shear Zones

Numerous lineaments were identified using diverse magnetic images (Figure 8-9) and were correlated with the subsurface lineament compilation from Pană et al. (2021). Lineaments were interpreted as ductile shear zones, brittle faults, boundaries, faults (when unclear about ductile/brittle nature), and lineaments (or structural trend). The GIS files containing the interpretation of lineaments and relation to documented structures are included in the Digital Appendix A.

Many lineaments of Pană et al. (2021) show a spatial correlation with the magnetic data, and new lineaments were identified including shear zones and brittle faults. However, the number of existing lineaments in Pană et al. (2021) is substantial. Due to time constraints, only a select number were inspected. Additionally, in many cases the interpreted magnetic and gravity lineament geometries and relationships are complex and would require further studies to better interpret them, such as define their order, and geometric and timing relationships. The most relevant lineaments identified are described in the subsections below.

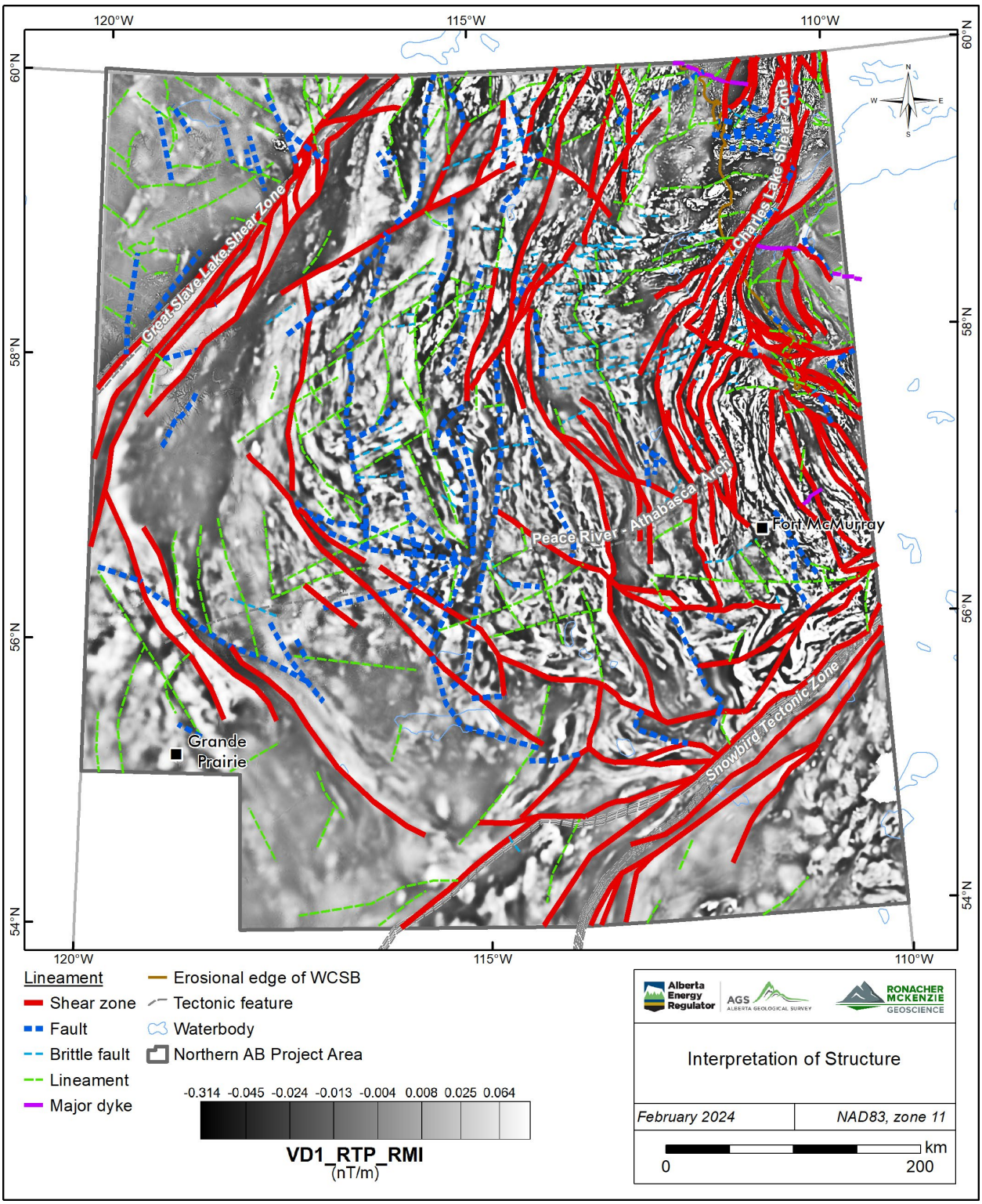

Figure 8-9. Interpreted linear features, including lineaments, faults and shear zones, in northern Alberta. Background image: first vertical derivative in CET colour scheme.

8.4.1 Great Slave Lake Shear Zone

The Great Slave Lake Shear Zone ("GSLSZ") in northern Alberta shows as a NE-trending magnetic and gravity lineament with splays and secondary lineaments with an estimated width of up to 30 km from the northern branch that separates the Hottah and Nova domains, to the southwest boundary of the magnetic low that defines the Kiskatinaw domain (Figure 8-10).

The NE trending GSLSZ is dominantly present on gravity and magnetic image products (Figure 8-11). Interestingly in the middle of the image, the lineament abuts a zone characterized by a magnetic and gravity high that appears to overlie the regional lineament. This is in the area where the Great Bear terrane is located.

Several N060E-oriented lineaments are present on either side of the GSLSZ. Lineaments with this orientation have been reported and are commonly interpreted as normal faults in the sedimentary stack and at basement level (Pană et al., 2021). These lineaments align, but do not necessarily overlap with features observed on the gravity images.

Some of the gravity products show a spatial correlation with the "dmh_30_K_uSh_top" horizon from the 3D subsurface model (Figure 8-12; Alberta Geological Survey, 2019). This horizon represents the top of the Upper Cretaceous Shaftesbury Formation, which lies just above the regionally significant Fish Scales Formation. The correlation indicates that gravity measurements are representative of the Phanerozoic strata, which can obscure definition of the crystalline basement without integration of additional data. Similar conclusions can be drawn for the gravity images in the kimberlite corridor.

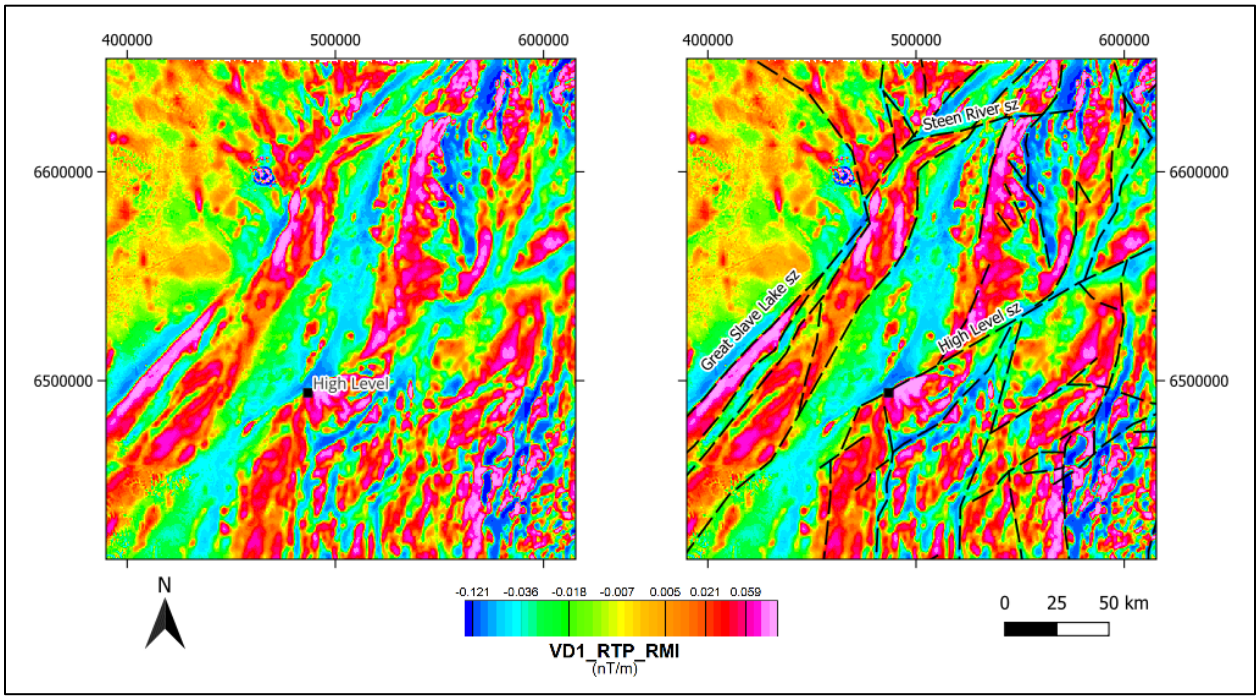

Figure 8-10. Northeast-trending GSLSZ, and ENE-trending High Level and Steen River shear zones.

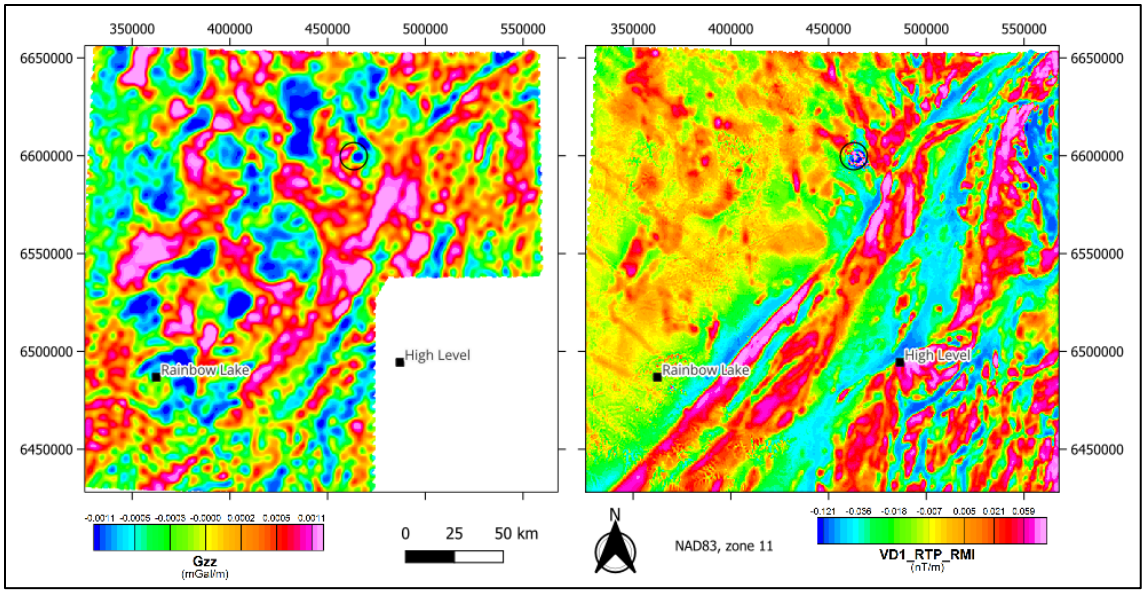

Figure 8-11. Great Slave Lake Shear Zone; (left) 1st vertical derivative of Bouguer anomaly (Gzz), and (right) RMI, reduced to pole, 1st vertical derivative. Steen River astrobleme in black circle (Prior et al., 2013).

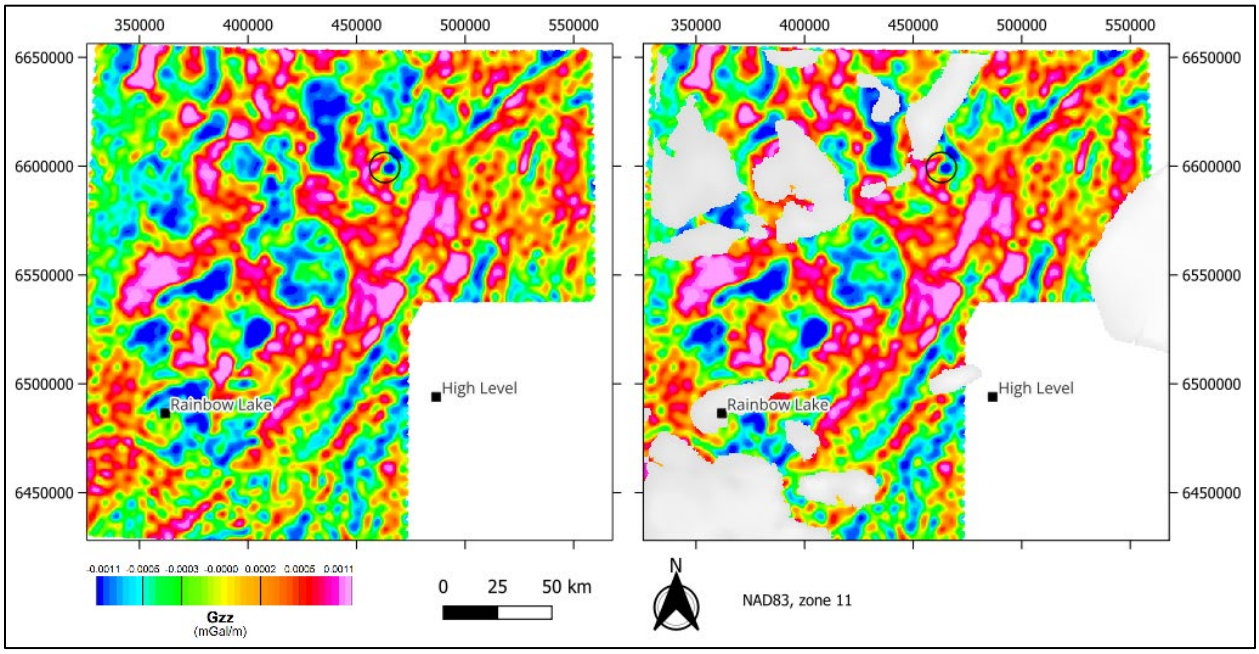

Figure 8-12. Great Slave Lake Shear Zone with 1st vertical derivative of Bouguer anomaly (Gzz; left) showing correlation of lineaments and domains overlain by the modeled Shaftesbury Formation in grey (right; Alberta Geological Survey, 2019). Steen River astrobleme in black circle (Prior et al., 2013).

8.4.2 High Level and Steen River shear zones

Across the northern part of the survey area, distinct ENE-trending linear features are visible in the geophysical data. One of these features is located east of the Great Slave Lake Shear Zone and can be confidently traced for about 250 km. This feature is herein termed the High Level Shear Zone, as it runs near the hamlet of High Level (Figure 8-10).

On regional tectonic domain maps, the High Level Shear Zone can be inferred as a zone where several domain boundaries are curved (e.g. Figure 4-3; Pilkington et al., 2000). It is shown as a discrete tectonic lineament only in a summary note by Peirce et al (n.d.).

A dextral sense of shear with 40km of dextral offset is interpreted by correlating distinct magnetic signatures across the lineament. (Figure 8-10). Regionally, the shear zone is bound to the west by uninterrupted magnetic lineaments that are associated with the Great Slave Lake Shear Zone. To the east, the shear zone cannot be confidently traced into the Taltson domain (e.g., Figure 8-9).

On a regional scale, the High Level Shear Zone does not offset Phanerozoic bedrock geology (Prior et al., 2013) nor is there a distinct spatial correlation with any of the 3D modeled horizons (Alberta Geological Survey, 2019), suggesting that this prominent shear zone is restricted to the crystalline basement.

There are also numerous ENE-trending lineaments that are sub parallel with the High Level Shear Zone. These lineaments are at a consistent 25 km spacing from each other (Figure 8-10) and are suspected to be genetically related. There are a few more lineaments that appear towards the south at 25-50 km spacing. Their lineaments truncating magnetic anomalies can be traced for 200-250 km; There are no distinct magnetic anomalies that can be correlated across these features; hence a sense of shear remains inconclusive.

Interestingly, the prolific Devonian Ladyfern gas field in British Columbia is along strike with the High Level Shear Zone. This petroleum accumulation is characterized by first-order ENE-oriented Phanerozoic faults that are genetically associated with hydrothermal dolomites (Figure 8 in Davies and Smith Jr, 2006). If there is a regional correlation, these ENE-trending lineaments and shear zones in the Northern Plains area may have been reactivated during the Phanerozoic.

A second distinct ENE-trending linear feature visible in the geophysical data is located east of the Great Slave Lake Shear Zone close to Alberta's Steen River settlement near the province boundary with Northwest Territories. This feature is herein termed the Steen River Shear Zone, runs parallel to the High Level Shear Zone and can be confidently traced for about 60 km (Figure 8-10). The Steen River Shear Zone displays a sinistral offset of the Chinchaga domain and Buffalo Arch subdomains. It is recommended to integrate the above findings with available seismic and well data to improve the constraints on these regionally distinct shear zones and their potential impact on brittle faults in the overburden, which helps improve our understanding of the Phanerozoic tectonic evolution of this region.

8.4.3 Dunvegan and Tangent faults

The Dunvegan fault is a basement-rooted fault in the western part of the PRA that affects the Paleozoic strata. It is a dominant fault in a NW-trending half-graben that offsets the basement-cover contact by about 0.1 s two-way travel time (ca. 200 m; Eaton et al., 1999; Wozniakowska et al., 2021). The fault forms the primary structural control to several petroleum fields (Figure 3.7 in Wright et al., 1994).

The Dunvegan Fault coincides with the boundary between the Ksituan and Chinchaga domains, which is clearly defined on aeromagnetic images (e.g., Figure 8-4); Pilkington et al., 2000). A correlation between brittle overburden faults and deeper-seated basement structures is commonly assumed.

Unfortunately, the resolution and/or quality of reported Lithoprobe images is insufficient for detailed observations to be made. In general, the uppermost part of the basement is transparent and devoid of distinct features, which is typical of seismic imaging of crystalline basement. Seismic reflectors are subhorizontal; some inclined reflection fabrics are observed, but these cannot be placed in a geologic context (Figures 17 to 19 in Wozniakowska et al., 2021). In the few published reports that display the deeper sections of the Lithoprobe profiles, shallow east dipping reflectors in the middle to lower crust can be observed (e.g., Ross and Eaton, 2002).

The Dunvegan Fault is also not clearly visible on the 2022 Kimberlite Corridor gravity images (e.g., Figure 6-4 and Figure 6-6). Only after integration with magnetic images and the structural lineaments compilation (Pană et al., 2021) can features related to the Dunvegan Graben be confidently interpreted. As seen in the Great

Slave Lake Shear Zone area (Figure 8-12), the gravity data in the Kimberlite Corridor area reflects the complex relationship of different structures, lithologies and boundaries that are present in the sedimentary stack.

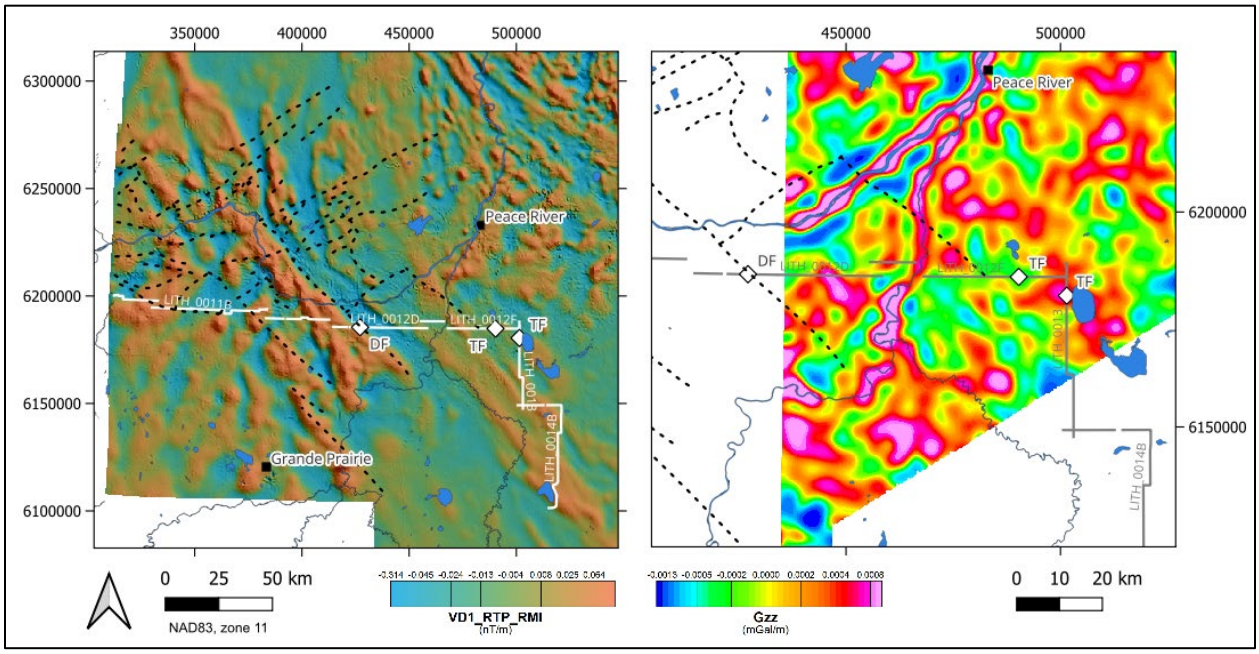

Figure 8-13. Integration of Phanerozoic structural lineaments in the Peace River Arch area (Figure 14.5 in Mossop and Shetzen, 1994; digitized by Pană et al., 2021) with aeromagnetic (left) and gravity images (right). White diamonds indicate where the Dunvegan (DF) and Tangent Fault (TF) are observed on the Lithoprobe seismic lines (white in left, grey in right).

The Tangent Fault is another basement-rooted normal fault impacting the Paleozoic sedimentary rocks of the PRA. The east-side down normal fault can be observed on the east-west oriented Lithoprobe Line 12 and on the north-south oriented Lithoprobe Line 13, allowing a pseudo-3D view of the fault (Figure 8-13). It offsets the basement-cover contact by about 0.1 s two-way travel time (Figure 18 in Wozniakowska et al., 2021).

Unlike the Dunvegan fault, there is no clear spatial correlation between the magnetic fabric and the Tangent Fault. Like the Dunvegan Fault above, the Tangent Fault can only be interpreted on gravity images after integration with the regional structural lineaments (Pană et al., 2021). These observations align with the conclusion by Ekpo et al. (2017) that regional faults in the PRA appear to have a subtle gravity response. In addition, their 2D gravity modeling, constrained by seismic and density logs from wells, indicated that measured gravity can be confidently modeled by lithologies and faults in the sedimentary stack alone (Figure 6 in Ekpo et al., 2017), highlighting that the impact of crystalline basement on the gravity measurements is minimal or localized.

On a regional scale, NW-trending Phanerozoic faults, such as the Dunvegan and Tangent faults, tend to align with the regional magnetic fabrics (Figure 8-13); in contrast, the NE-SW oriented Phanerozoic faults of the Fort St. John and Hines Creek grabens (Mossop and Shetsen, 1994) appear to have only a subtle to non-existent correlation with both the magnetic and the gravity images (Figure 8-13). There is no consistent geophysical signature related to these regional structures.

In summary, as previously concluded by Eaton et al. (1999), the integration of different geophysical datasets shows that any genetic links between the basement rooted Dunvegan and Tangent faults and the underlying reflective basement structures remain speculative at best. Seismic reprocessing of Lithoprobe Lines 11-14 as well as integration with other seismic and well data is highly recommended.

Other faults and lineaments documented in the Peace River Arch area of the WCSB by Pană et al. (2021) were identified in the magnetic filter and derivative products and they can be found in the accompanying GIS files included in the Digital Appendix A.

8.4.4 Charles Lake Shear Zone

The Charles Lake Shear Zone consists of a system of anastomosing splays of shear zones in the Taltson domains. Along the eastern part of the project area, the magnetic products show that the Charles Lake Shear Zone is a zone of highly variable width. Its narrower part occurs in the Shield area adjacent and north of the Athabasca Basin. The shear zone widens considerably in the south spreading its branches towards the SW and SE in a fan-like structure. The eastern branch separates the Rae Craton from the Taltson Domain. The western branch is truncated by a competent unit, possibly a large intrusion not affected by the shearing or intruded later. The splays of the Charles Lake Shear Zone abut to an EW-trending shear zone that separates most of the Taltson subdomains from the refolded Taltson South subdomain (Figure 8-14).

8.4.5 Snowbird Tectonic Zone

Across the southeastern corner of the project area, the magnetic products show the STZ as a NE-trending narrow zone or belt of parallel lineaments that is coincident with the Thorsby Domain (Figure 4-3). This narrow zone separates the southernmost subdomain of the Taltson magmatic arc from the Rimbey magmatic arc (Figure 8-6 and Figure 8-7). The Taltson South subdomain, which displays NE-trending refolding fabric (Type 3 interference patterns of Thiessen, 1986) different from the N to NE-linear trends of the rest of the Taltson domain in the north, appears to have absorbed deformation related to the STZ. Alternatively, the Taltson South subdomain may instead represent an Archean terrane.

The northern splay of the STZ runs through a group of small subdomains of contrasting fabric orientations, possibly broken, displaced and rotated from their original position. The northern splay continues to the SW as a narrow zone between the Ksituan and Wabamun domains.

The existing outline of the STZ and its northern splay from Pană et al. (2021) correlates with these observations and therefore, does not require modification, but may require addition of an E-trending branch running along the northern edge of the Taltson South subdomain. It appears that this new branch continues into the Buffalo Head Domain. The southernmost subdomains of Buffalo Head Domain are separated from northern subdomains by NE-trending splays related to the STZ.

8.4.6 Beatty River Shear Zone

The Alberta extension of Saskatchewan's Beatty River Shear Zone ("BRSZ") is mentioned in few reports (e.g., Ramaekers 2004), but it is not mentioned in more recent reports by Pană et al. (2021). The only reference in Pană et al (2021) to basement faults that spatially correlate with the BRSZ are unnamed EW- and NW-trending basement faults interpreted from structure contours of the Precambrian crystalline basement and overlying strata in the Athabasca Basin area (Cotterill and Hamilton, 1995).

In the magnetic products, the Beatty River Shear Zone is a complex system of EW-, WSW- and NW-trending shear zones in the southern rim of the Athabasca Basin (Figure 8-14). The EW-trending shear zone runs parallel to the southern edge of the Athabasca Basin. The eastern splays of the Charles Lake Shear Zone are intersected by this EW-trending shear zone and separates the Rae Craton in two subregions (Figure 8-14). The southern region displays a high frequency linear fabric trending NW and folding against the shear zone. The northern domain displays the linear fabric trending to the NNW and gently curving to the NNE. This pattern of drastic change of fabric trend from NW to NE and folding in the south to a gentle curvature in the north repeats in most of tectonic domains from Ksituan in the west to Taltson in the east. This EW-trending structure dextrally offsets the splays of the Charles Lake shear zone. The NW-trending shear zones abut to the EW-trending shear zone and the eastern branch of the Charles Lake Shear Zone.

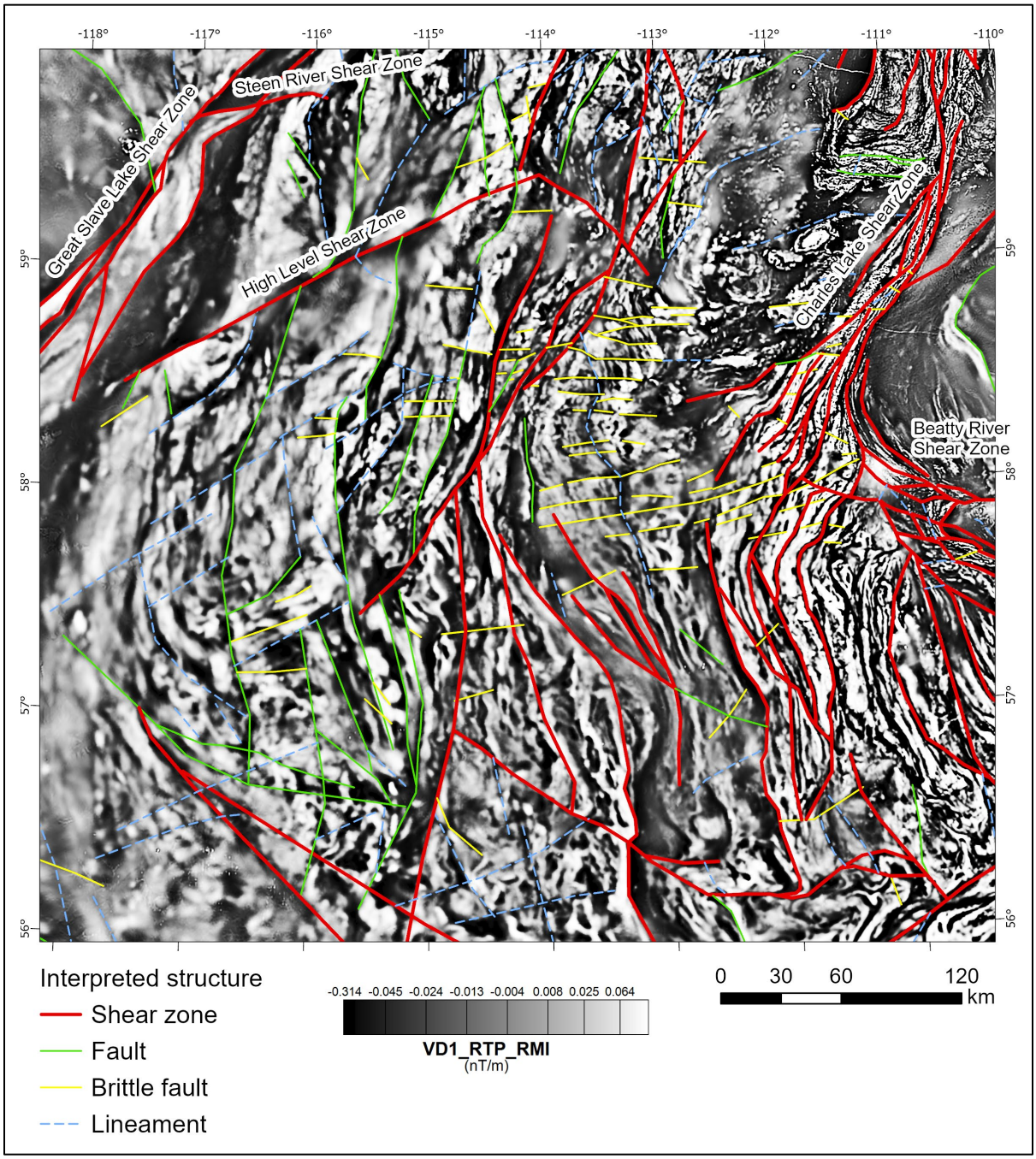

Figure 8-14. Structural complexity in the crystalline basin along the southern rim of the Athabasca Basin.

8.5 Depth to Basement

Fathom Geophysics generated depth to magnetic source and basement elevation surface images (Appendix 1; Figure 8-15). The basement surface corresponds with the regional pattern observed in the 3D modelled surface of the basement based on top picks by Branscombe (2017) (Figure 8-16). Thus, Fathom Geophysics' basement products display an increasing basement depth and decreasing elevation towards the SW, however estimated elevations from the magnetic data are underestimated by half the values of the actual elevations. Fathom Geophysics' products provide more detailed topography and show deeper NE- and ENE-trending narrow zones along the Snowbird Tectonic Zone and the High Level Shear Zone, respectively, which are not apparent in the 3D model (Figure 8-16).

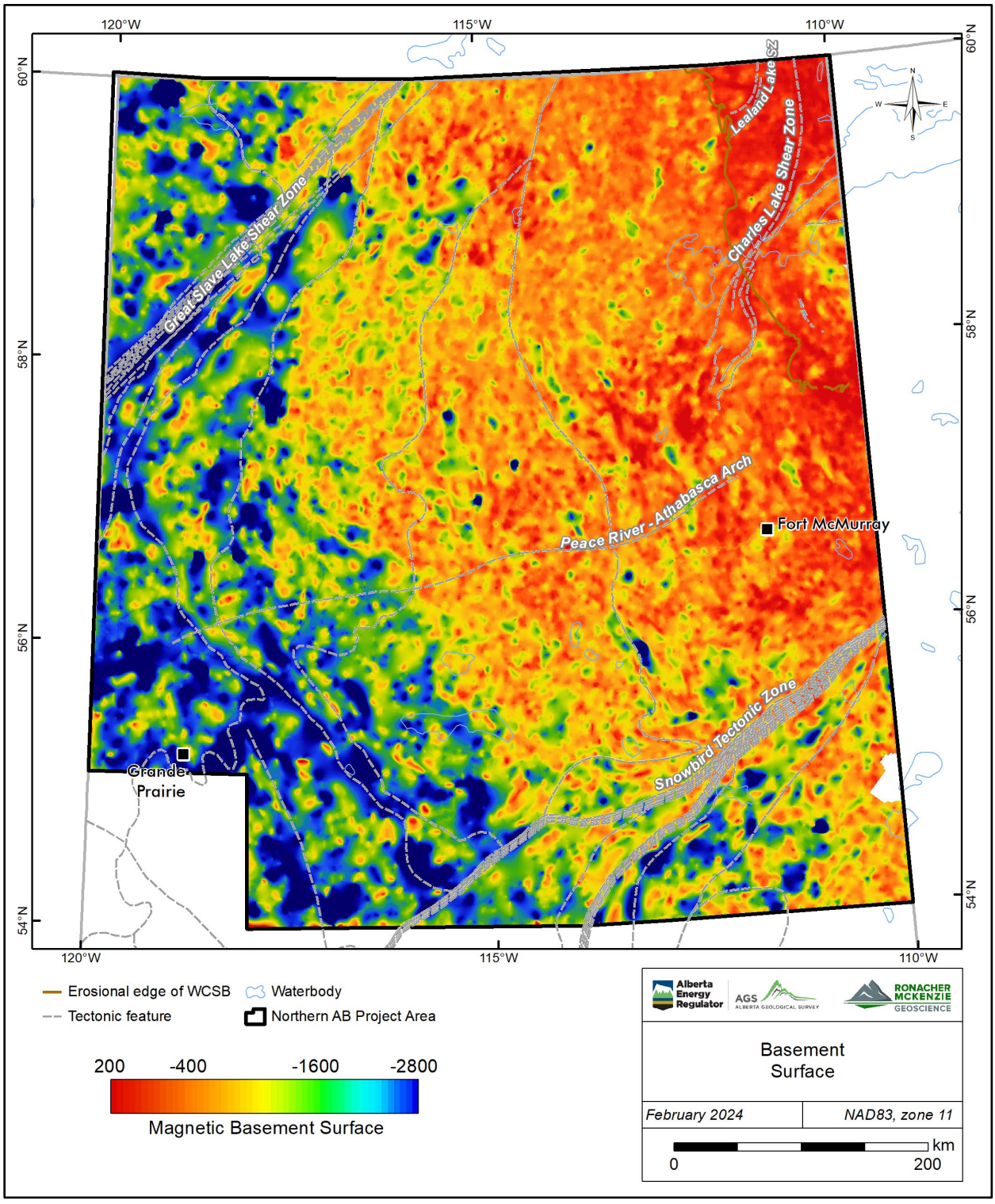

Figure 8-15. Magnetic basement surface product from Fathom Geophysics' depth to basement analysis. Selected structural elements are represented by dashed grey lines. Selected elements from Pana et al (2021) are the Great Slave Lake Shear Zone, Charles Lake Shea Zone, Snowbird Tectonic Zone, and Peace River-Athabasca Arch. Subdomain boundaries are the ones defined in this work.

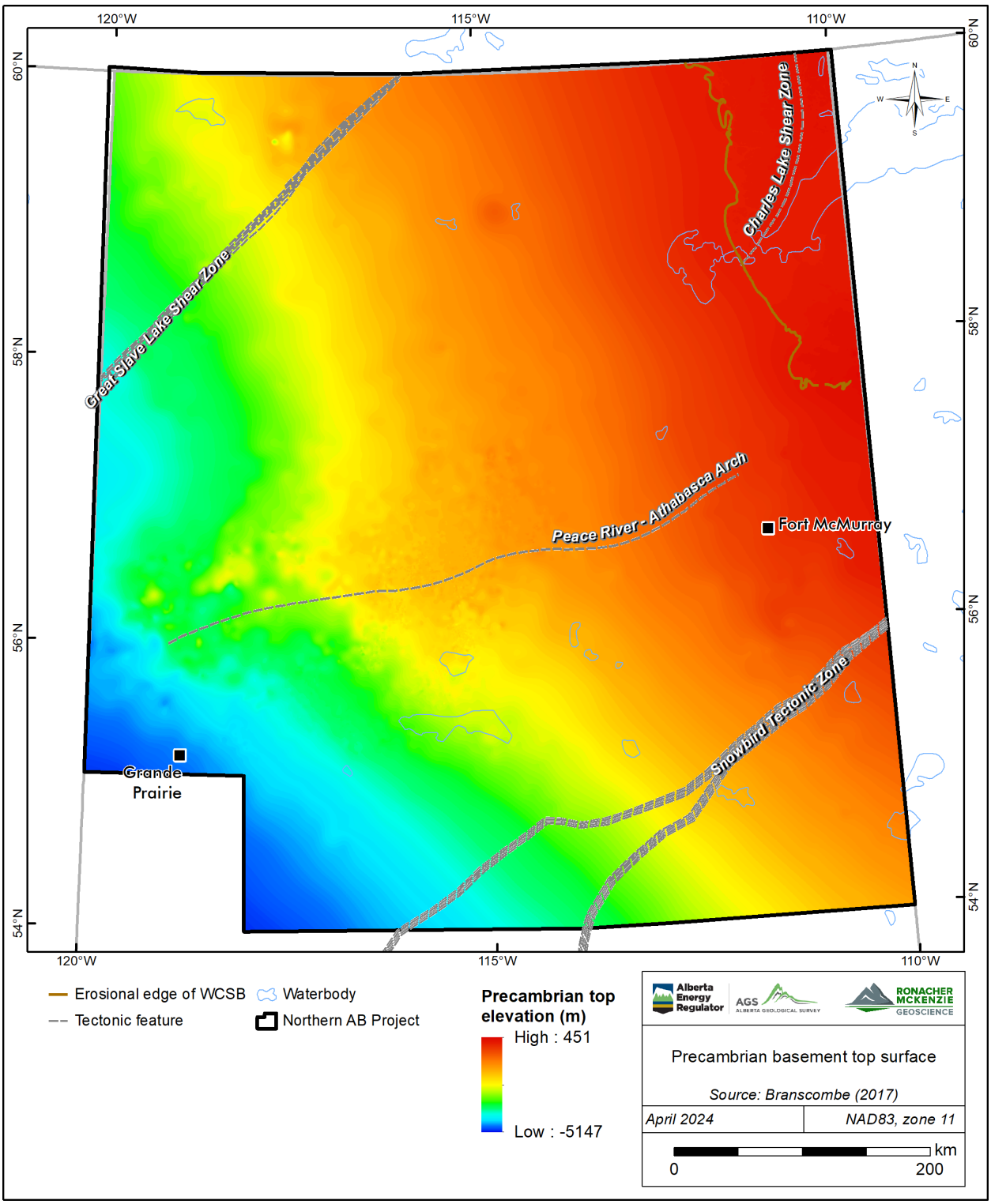

Figure 8-16. Precambrian basement top surface in northern Alberta; taken from AGS (Branscombe, 2017).

8.6 Intrusions

Intrusion detection was conducted in the project area using a combination of manual examination and automatic radial symmetry detection (Figure 8-17). Small and rounded magnetic anomalies were identified that can be interpreted as probable intrusive bodies. These anomalies are noted to be magnetic highs and lows. Following automatic detection, a manual examination was conducted that included calibration with culture such as urban sites and industry infrastructure, and calibration with the known geology. Some kimberlite bodies were detected by automatic detection (e.g., K1, K3 and K5 kimberlites), but manual detection was more efficient for detection of known kimberlites because automatic detection was adjusted to detect larger circular anomalies (> 2 km^2) to avoid detecting cultural effects, whereas manual detection could work with supporting cultural datasets for visual correlation.

Anomalies interpreted to be intrusions in the project area display the following character:

- single lobe small circular or oblate magnetic anomalies;
- isolated to poorly isolated high frequency smaller (< 5 km^2) circular or asymmetric anomalies;
- larger rounded multi-lobe anomalies; and
- broad rounded anomalies with distinct internal texture.

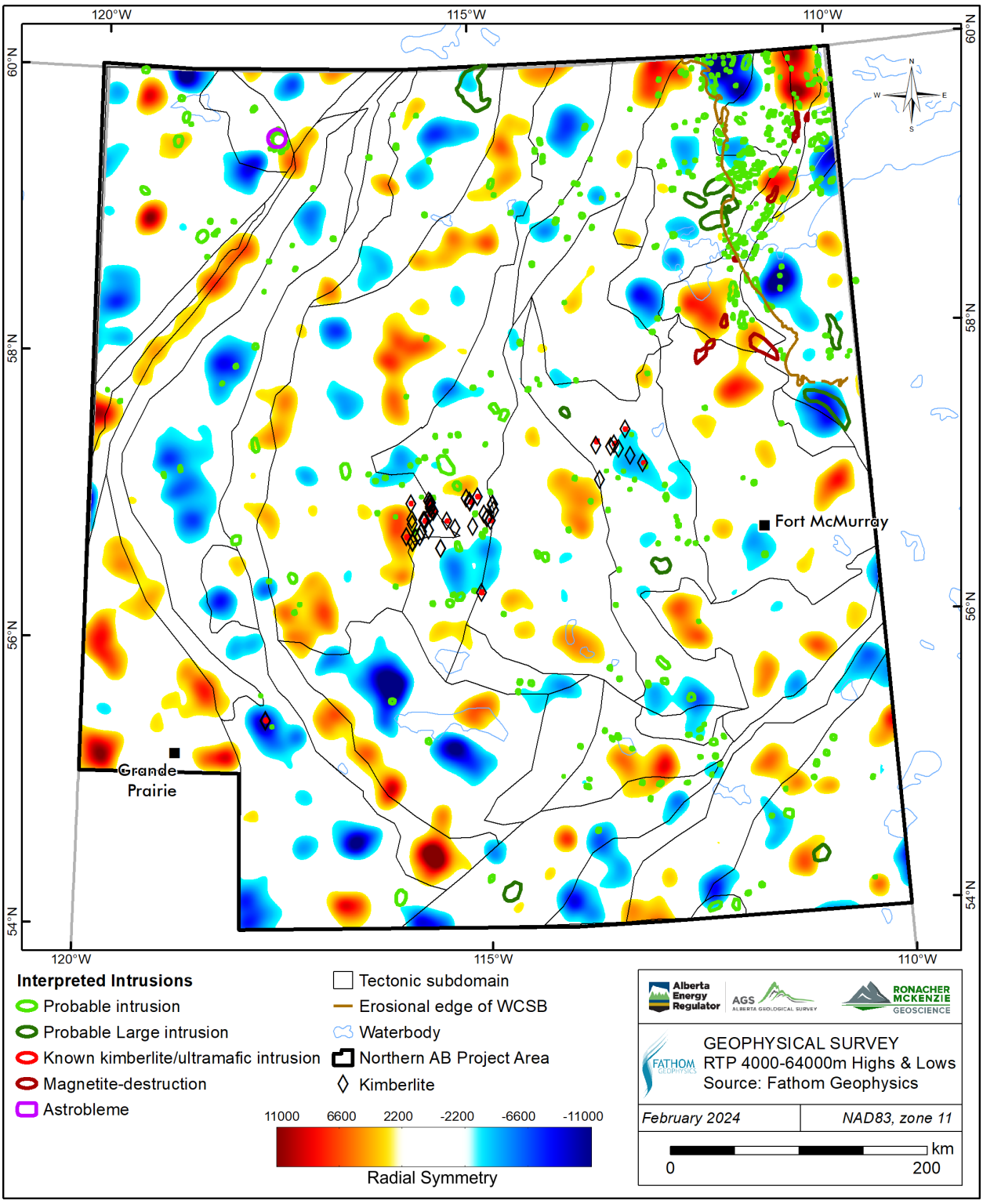

Figure 8-17. Intrusion detection results from Fathom Geophysics' automatic radial symmetry analyses for 4000 m magnitude independent wavelength (red represents rounded magnetic highs, blue represent rounded magnetic lows, and colour bar represents radial symmetry (i.e.,how radially symmetric is a high or low). Subsequent manual examination and selection of rounded anomalies are outlined in green.

8.7 Kimberlite Corridor

Some of the known kimberlite bodies (e.g., Eccles, 2011) are observed in the magnetic products. These show as clear high frequency circular to semi-circular anomalies in AS, VD1 and VD2 products (Figure 8-18). These anomalies are isolated in magnetically active backgrounds. The survey lines of the magnetic survey are too widely spaced for kimberlite detection of most of Alberta's kimberlites (100-600 m in diameter), which explains why only some bodies are observed. Moreover, cultural artefacts related to oil and gas activity produce similar high frequency anomalies making the interpretation of kimberlites equivocal.

8.7.1 Mountain Lake

The Mountain Lake ultrabasic intrusions have a subtle magnetic signature and are best recognizable in the second vertical derivative that highlights an oblate high frequency anomaly. An industrial site in the area displays a more prominent circular high frequency anomaly, whereas a pipeline installation site displays a weaker anomaly (Figure 8-18). Radial symmetry results for 4000 m wavelength detects a rounded anomaly at Mountain Lake. A 15 km form line trending to the NNE occurs adjacent to Mountain Lake. This lineament differs from the general NW trend of the Chinchaga domain fabric.

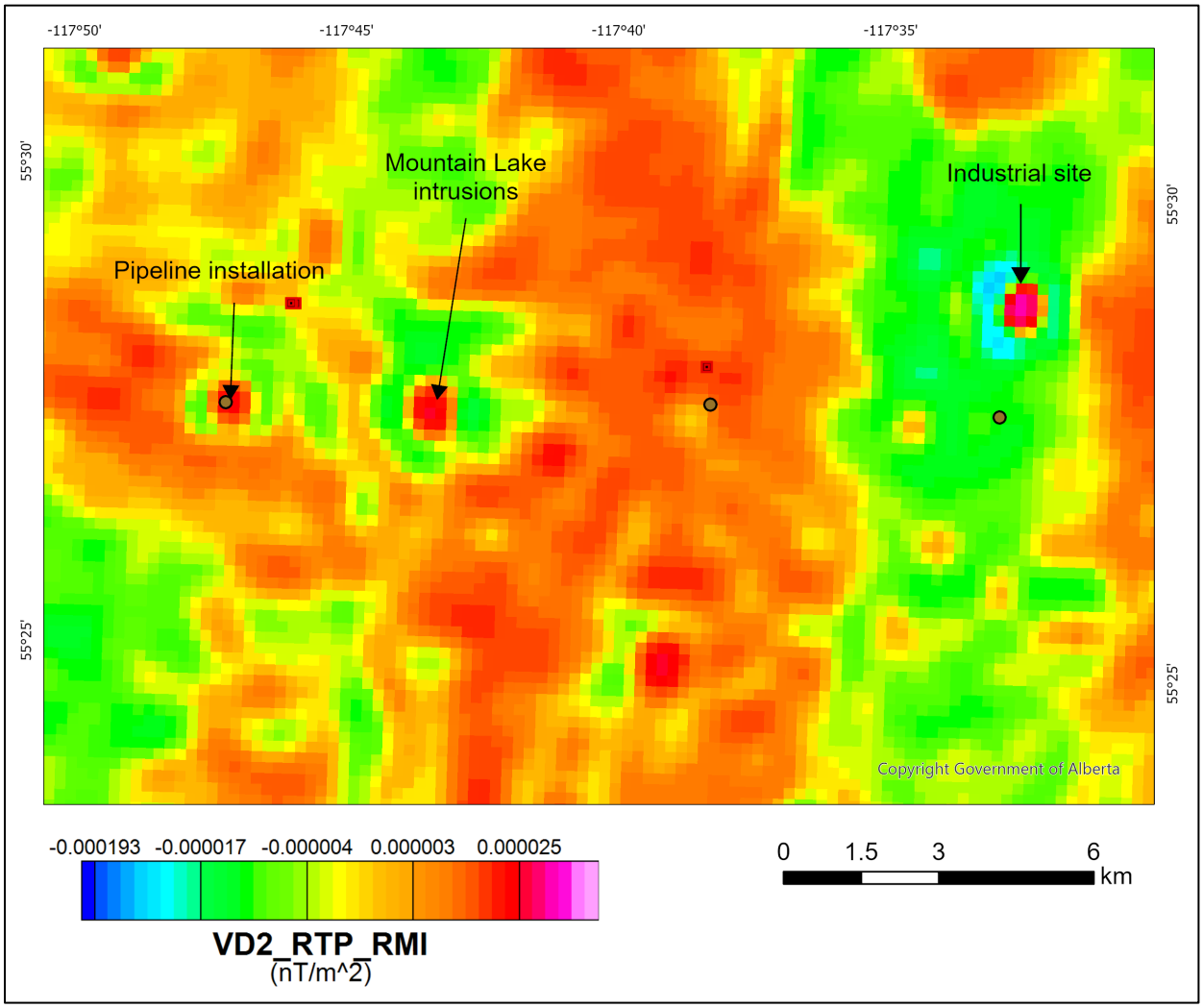

Figure 8-18. Mountain Lake ultrabasic intrusions and their magnetic signature on RMI analytic signal image.

8.7.2 Buffalo Head Hills

Some kimberlites in the Buffalo Head Hills field (e.g., K3, K5, K6, K8, K11) show as high frequency anomalies in magnetic products (Figure 8-19), however the magnetic response is similar to the signature of nearby cultural artefacts such as oil and gas infrastructure (Figure 8-19). Only K1, K3, K5 and K19 were detected by radial symmetry analysis for the 500 m wavelength.

The kimberlites of the Buffalo Head Hills are located in the Buffalo Central subdomain or at the boundary between the Buffalo High and Buffalo Central subdomains. The Buffalo Central subdomain represents the contact zone between Buffalo High and Utikuma domains of Pilkington et al. (2000). This subdomain shows evidence of remanence throughout (Figure 8-20) and the contact with Utikuma subdomain correlates with a N-trending gravity low (Figure 8-21).

North- and NNW-trending faults intersect this kimberlite field, which are interpreted as deep-seated and possibly controlling the formation of the Buffalo Central subdomain. Northeast to ENE-trending faults related to Phanerozoic grabens in the WCSB described by Eccles et al. (2002) were not observed.

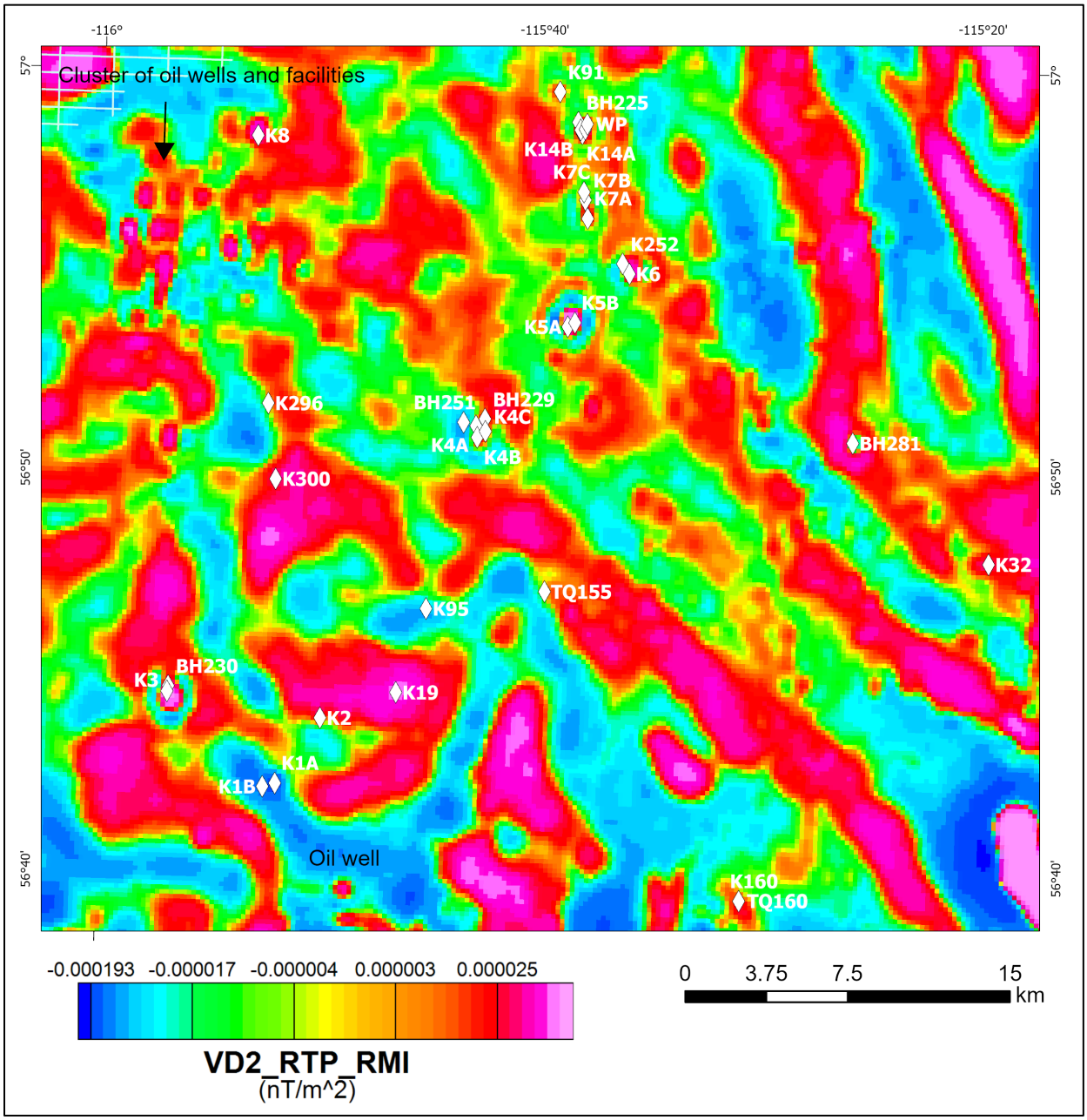

Figure 8-19. Illustration of known Buffalo Head Hills kimberlites and their magnetic signature on the RMI RTP VD2 image.

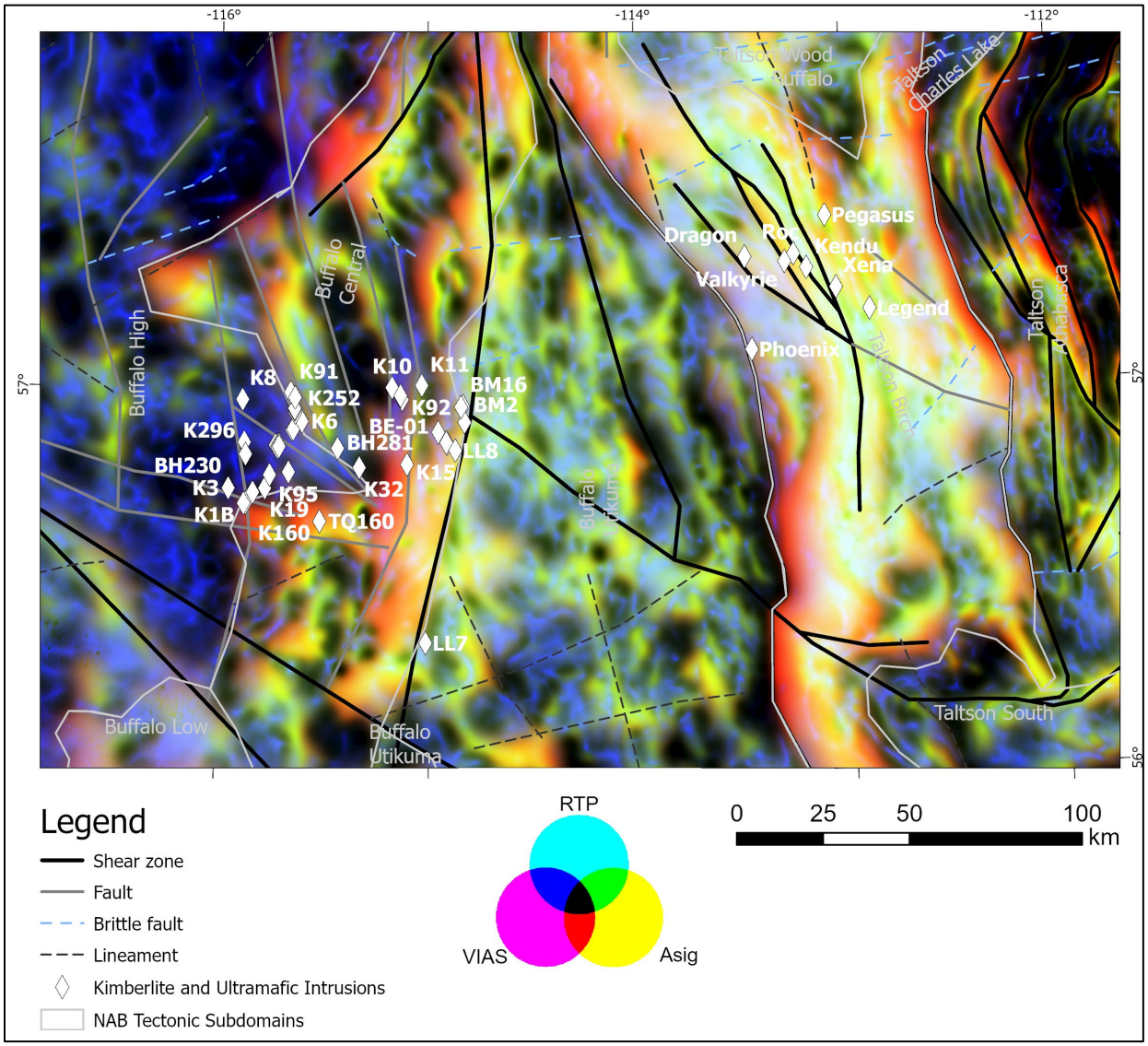

Figure 8-20. Location of kimberlites of Buffalo Head Hills (west) and Birch Mountains (east) in relation to interpreted basement structure on ternary of RTP, analytic signal of vertical integral, and analytical signal. Red colour indicates areas most affected by magnetic remanence.

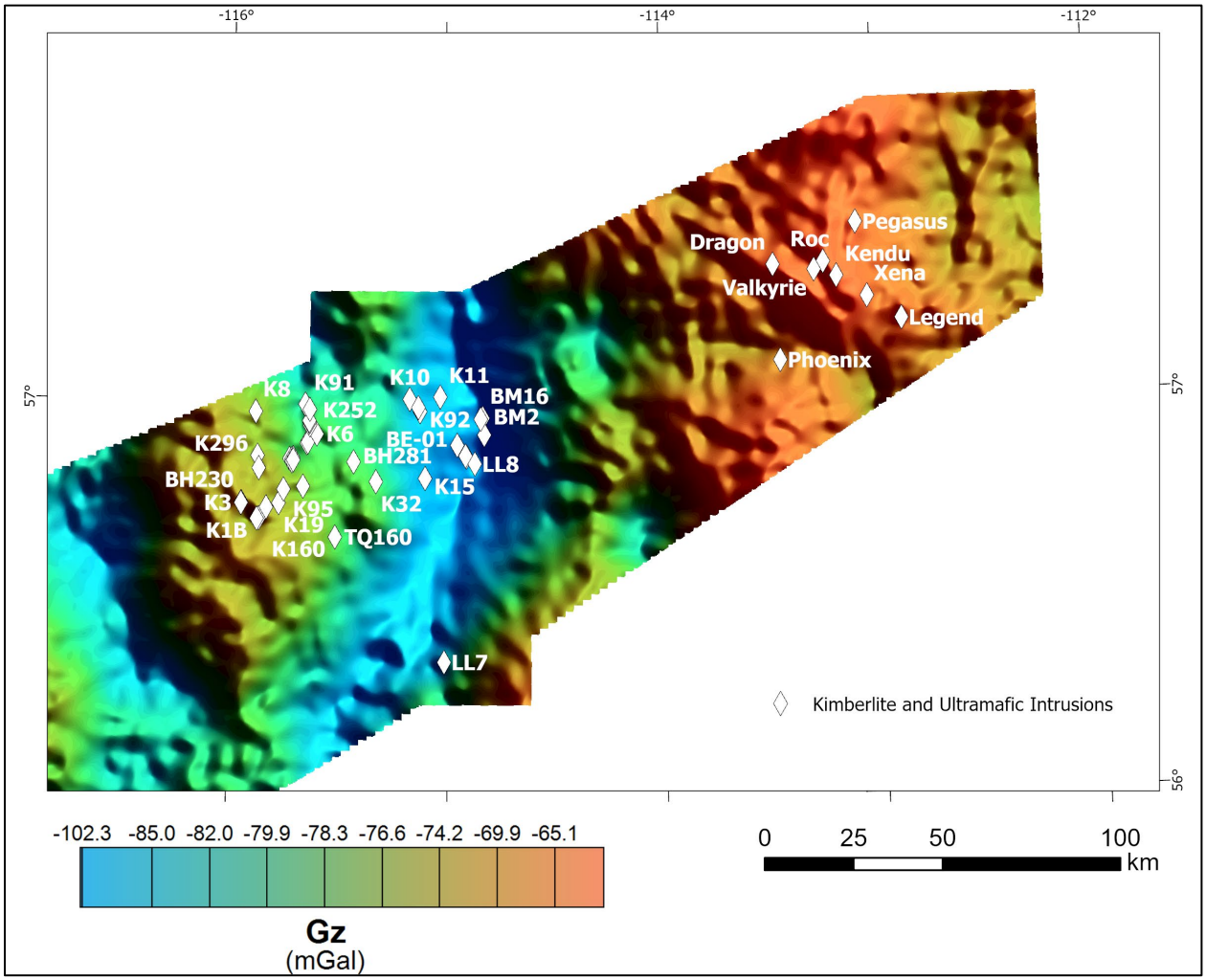

Figure 8-21. Buffalo Head Hills (west) and Birch Mountains kimberlites (east) in northern Alberta. Background image: Bouguer Anomaly (Gz).

8.7.3 Birch Mountains

Some kimberlites in the Birch Mountains field (e.g., Legend, Xena, Pegasus) show a subcircular high frequency anomaly, however the response is similar to the signature of cultural artefacts such as industrial sites, and oil and gas gathering stations and processing plants (Figure 8-22). None of Birch Mountains kimberlites were detected by radial symmetry analysis.

The Birch Mountains kimberlite field occurs in the Taltson Athabasca subdomain. The kimberlites of this field are located in a sheared domain and are spatially related to a second order NW-trending shear zone. This subdomain shows evidence of remanence along the boundaries (Figure 8-20).

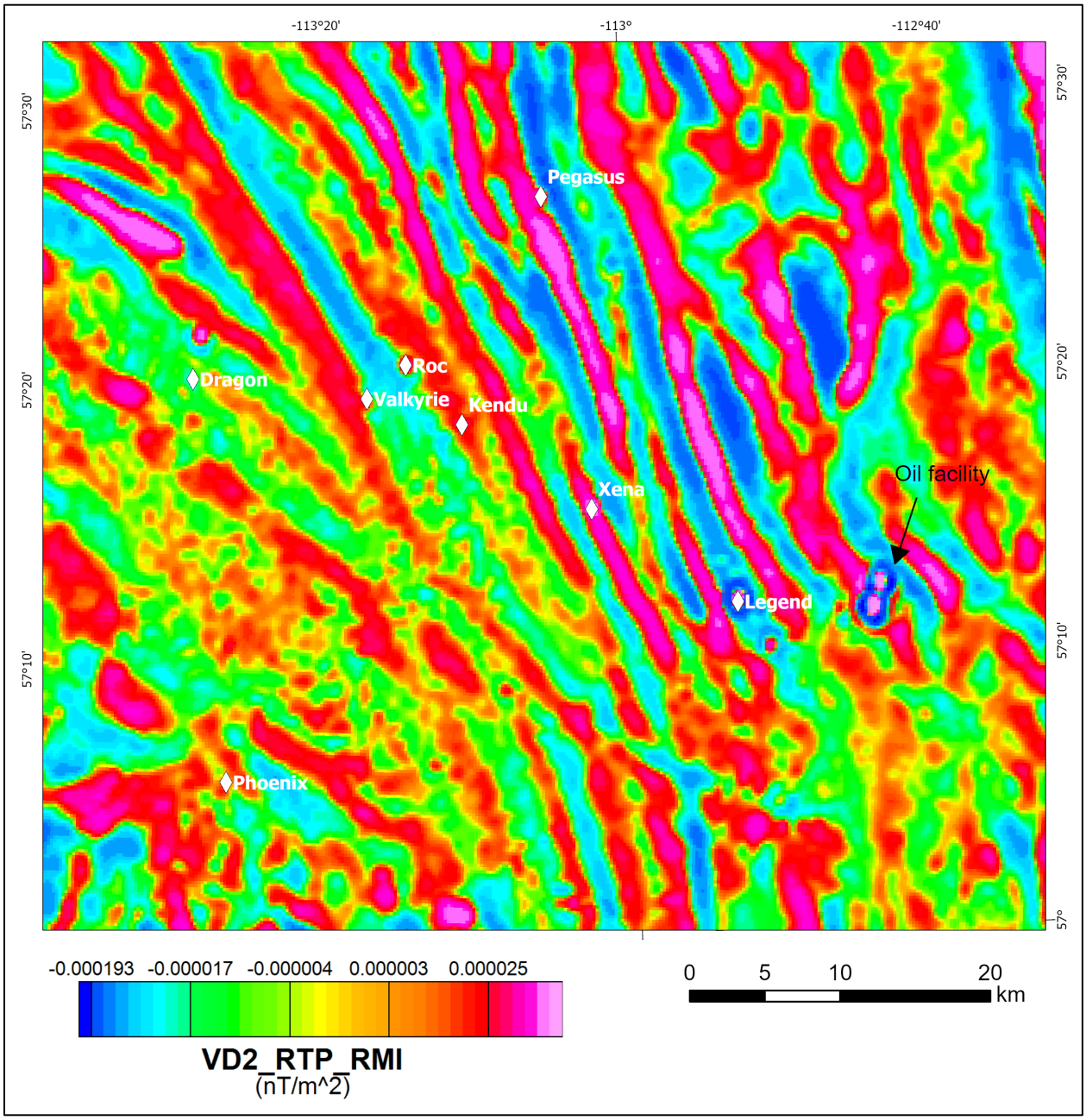

Figure 8-22. Illustration of known Birch Mountains kimberlites and their magnetic signature on RMI RTP VD2 image.

8.8 Astroblemes

Astroblemes are the (eroded) remnants of meteorite impact craters. Two such unique structures have been confidently recognized in the project area, Steen River and Hotchkiss structures (Prior et al., 2013; Pană et al., 2021).

The Steen River astrobleme is located approximately 100 km north of High Level. All magnetic images show a prominent circular anomaly that is spatially associated with the Steen River structure (Figure 8-23). The structure is about 10 km in diameter with a higher amplitude central anomaly. The outside of the circular structure displays anomalies in the NW and SE corners.

The Hotchkiss astrobleme located in township 98 and range 06, near the Chinchaga River, is an anomalous feature that has been observed on seismic data (Mazur, 1999). However, this feature has no expression in the magnetic products.

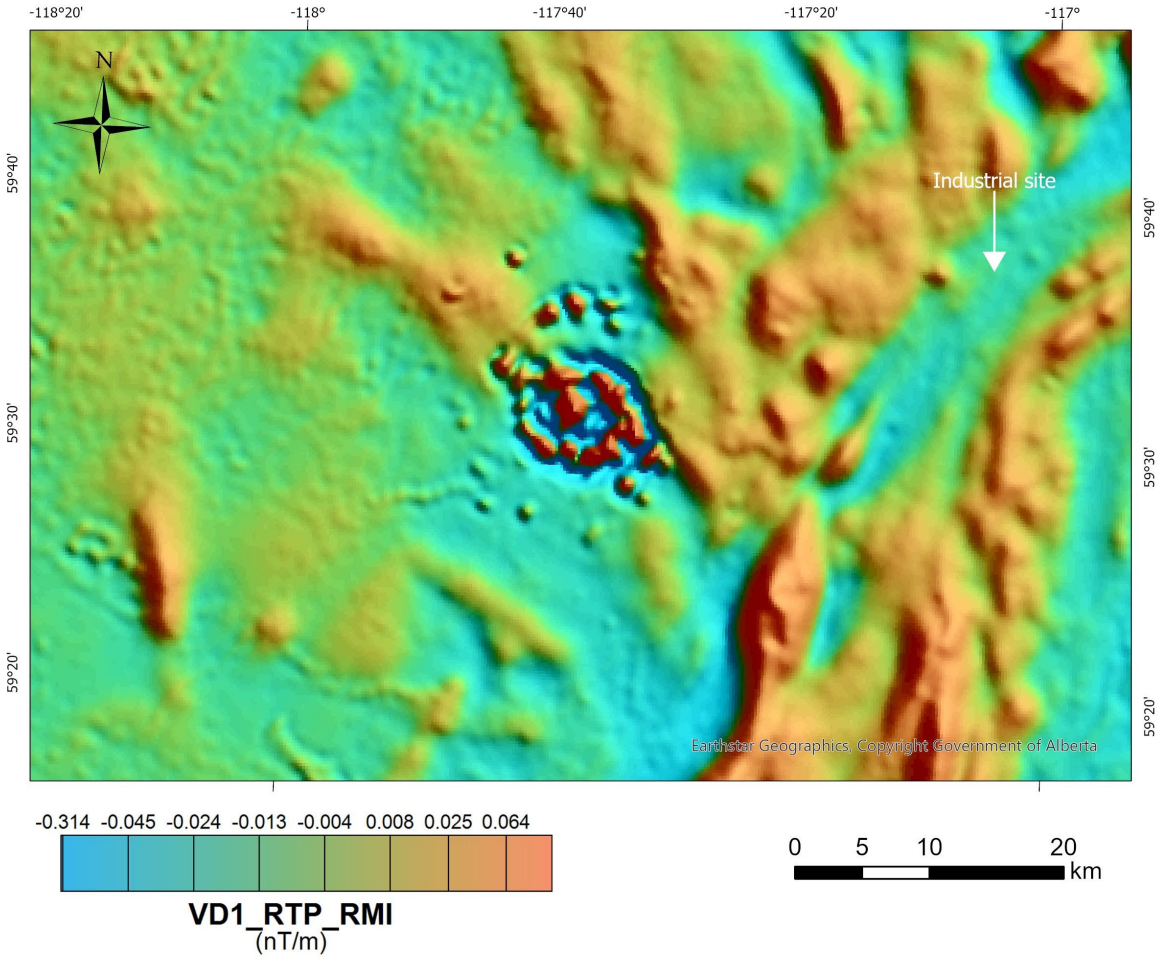

Figure 8-23. Magnetic signature of Steen River astrobleme on first vertical derivative image.

8.9 Critical Mineral Potential

8.9.1 Helium

Oil and gas fields in Alberta have economic (>0.3%) concentrations of helium (Figure 8-24; Lyster et al., 2021). Geological models that describe the generation, migration and trapping of radiogenic helium (^{4}He) follow a similar workflow as oil and gas accumulations and require: (1) a source of radioactive Uranium-238, Uranium-235 and Thorium-232 decay in the crust such as granitic basement rocks, (2) time to accumulate such as in old basement rocks (3) heat and/or deformation event that releases helium from minerals, and also nitrogen to transport it (primary migration) (4) buoyancy or solution in water and the presence of fracture and/or fault systems that serve as migration pathways for gas and/or fluids (secondary migration), (6) gas accumulation, and (7) trap integrity (Danabalan et al. 2022). A helium accumulation may not necessarily overlie the radioactive source that initially released it.

For northern Alberta, the Buffalo Head terrane includes felsic-to-intermediate metaplutonic rocks, and felsic metavolcanic rocks as a potential source rock of radiogenic uranium and thorium. In fact, geochemical data available from core samples from oil and gas wells that intersected the basement (unpublished data Burwash et al., 1994), show anomalous U concentrations above 10 ppm in the Ksituan, Buffalo Arch, Rimbey and Taltson magmatic arcs, and in the Buffalo Central subdomain (Figure 8-24). Brittle faults connecting these source rocks with the Phanerozoic strata cannot be consistently interpreted using aeromagnetic products alone (Section 8.4; Brem et al., 2024). Therefore, establishing gas/fluid pathways from the suspected source to sites of helium accumulations in the Phanerozoic strata requires further integration with other subsurface datasets.

8.9.2 Lithium

Oilfield brines in Alberta have anomalous concentrations of lithium (>50 mg/L), particularly in pools within Devonian strata. The origin of lithium in these brines is still debated but chemistry data collected and interpreted by AGS suggested they either formed by the dissolution of halite and mixing with Li-enriched basement or Cambrian-derived fluids in west-central Alberta brines or by preferential dissolution of Li-enriched late-stage evaporite minerals from the middle Devonian Prairie Evaporite into evapoconcentrated late Devonian seawater for south-central Alberta (Huff, 2019). In the project area, where there is evidence of fluid mixing, the highest lithium anomalies (>100 mg/L) are above the Chinchaga Domain (Figure 8-25), which has been interpreted here as a metasedimentary and/or volcanic terrane based on its magnetic low intensity and available basement sample descriptions from Burwash et al. (1994; 2000). The Chinchaga Domain rocks might be the primary source of lithium in oilfield brines of west-central Alberta.

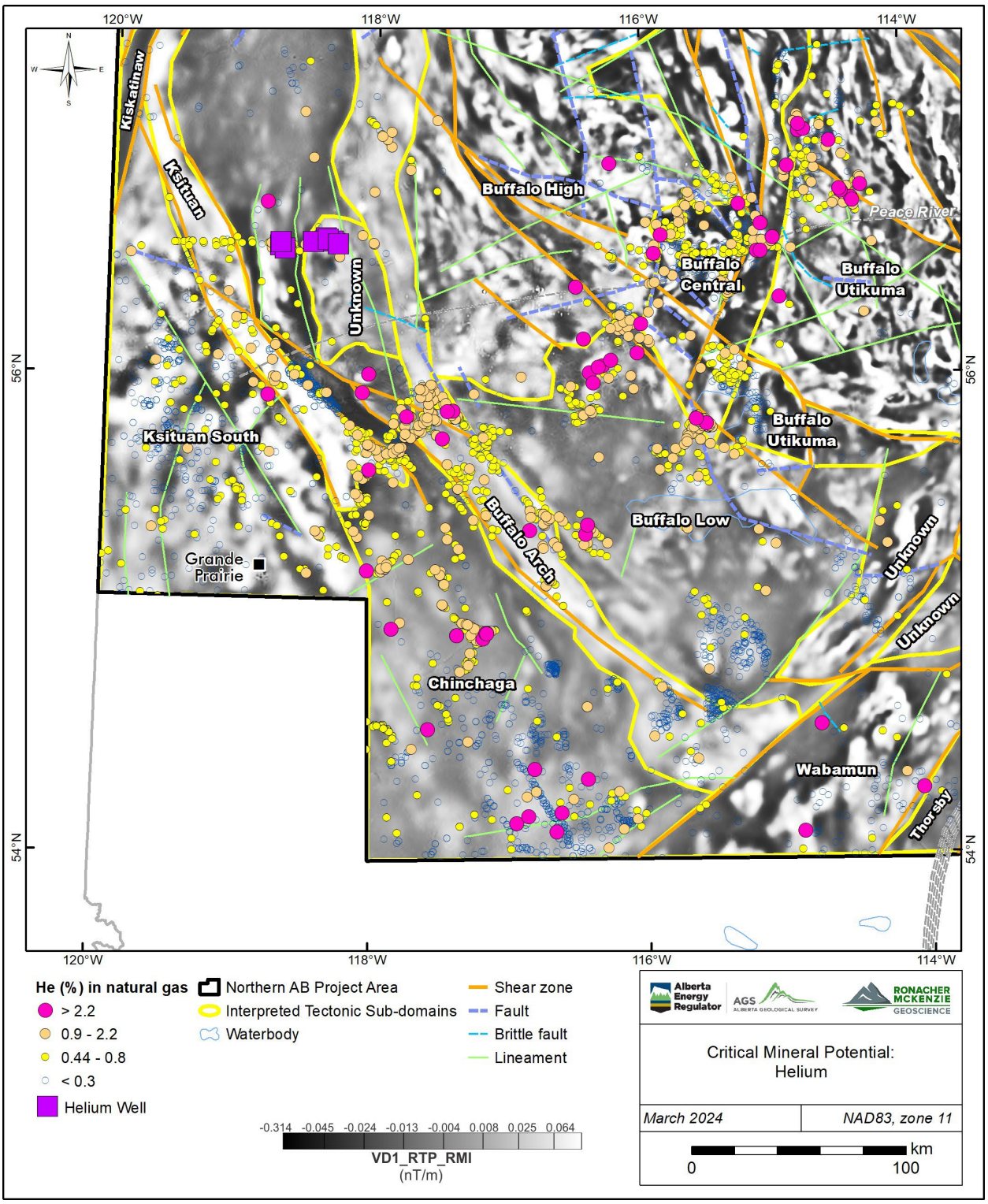

Figure 8-24. Helium concentrations in natural gas in relation to interpreted basement lithotectonic subdomains and lineaments. Helium data from Lyster et al. (2021).

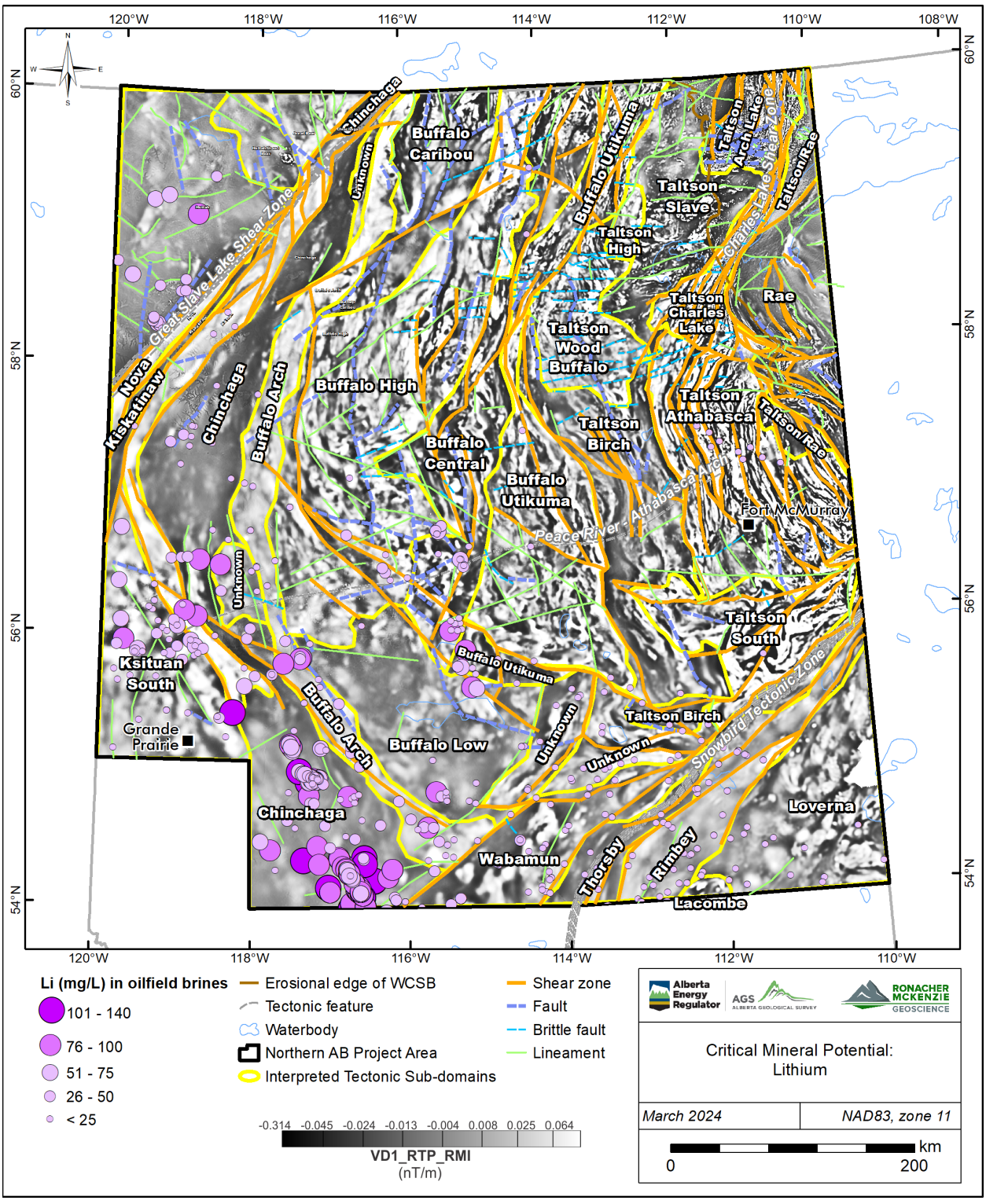

Figure 8-25. Lithium concentrations in brines from oil-gas wells in relation to interpreted basement lithotectonic subdomains and lineaments. Lithium data from Lyster et al. (2022).

8.9.3 Uranium

Alberta has potential for uranium deposits in the Athabasca Basin in northeastern Alberta (Figure 4-1) in relation to basement shear zones and faults. The southern edge of the Athabasca Basin where the Charles Lake Shear Zone meets the Beatty River Shear Zone offers structural complexity with several sites such as jogs and bends that may intersect the basal strata and unconformity of the Athabasca Group (Figure 8-26) or may offer the right mineralogy (e.g., graphite) as other shear zones in the Athabasca Basin to reduce and precipitate uranium from mineralizing fluids.

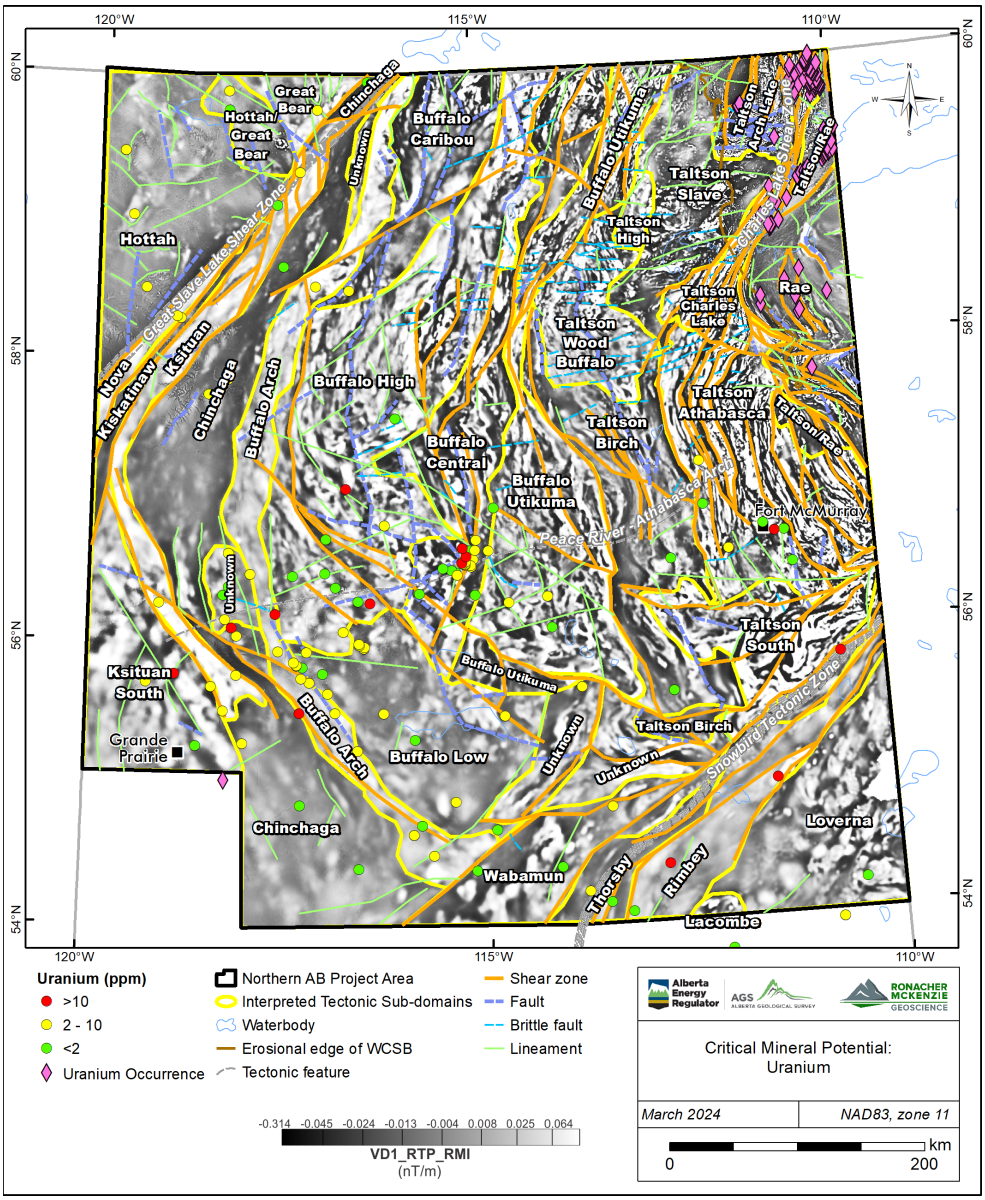

Figure 8-26. Uranium concentrations in samples from cored oil-gas wells and uranium occurrences in relation to interpreted basement lithotectonic subdomains and lineaments. Uranium concentration data from Burwash et al (unpublished data 1994) and uranium occurrences from Lopez et al (2020).

8.9.4 Zinc

Carbonate-hosted lead-zinc ("MVT") Pine Point district in NWT is structurally located along the GSLSZ with the individual deposits distributed in linear trends in Paleozoic platform carbonate sequences of the WCSB above basement fault scarps. In northwestern Alberta, lead and zinc mineral occurrences are documented in Devonian platform carbonates proximal to the GSLSZ (Pană, 2003; Figure 8-27). The interpretation of magnetic and gravity products shows that the GSLSZ presents structural complexity in its middle section (between the High Level and Steen River shear zones) with several bends that may have controlled potential epigenetic Pb-Zn mineralization in brecciated and hydrothermally dolomitized Devonian carbonates during possible GSLSZ reactivation during the Mesozoic – Cenozoic tectonic events (Davies and Smith, 2006).

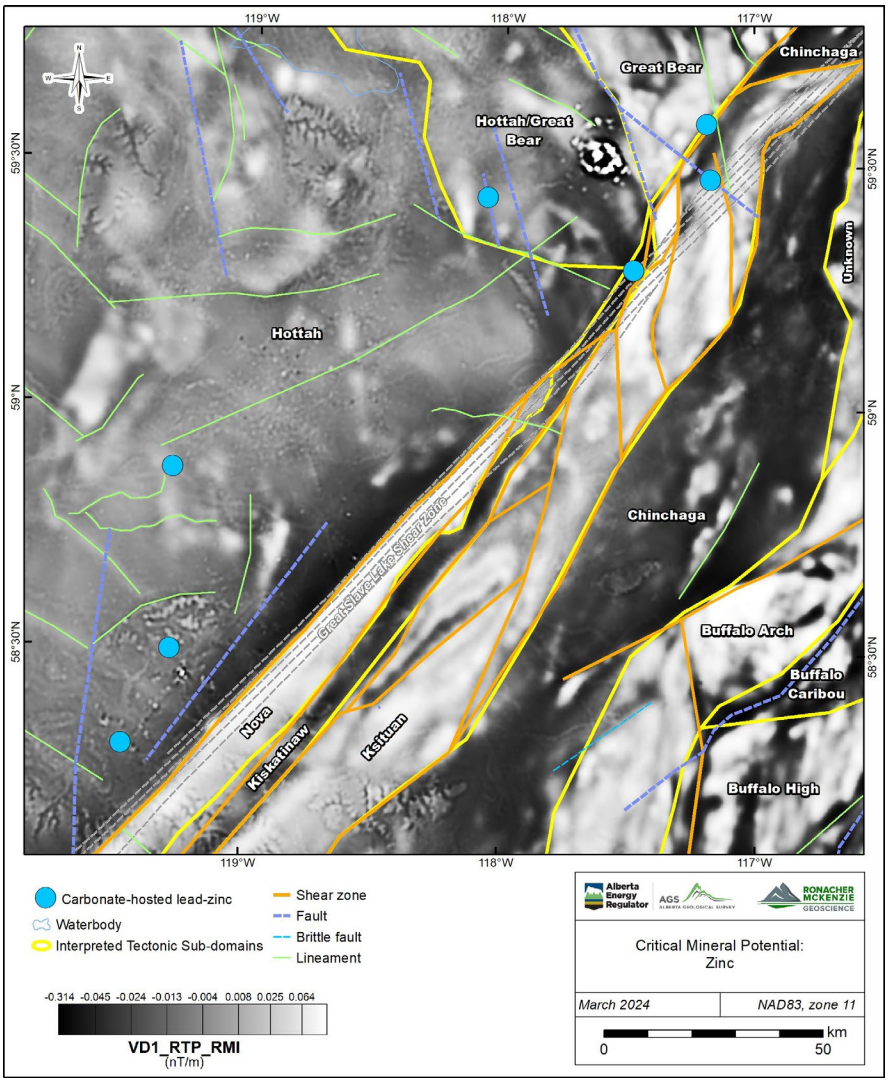

Figure 8-27. Lead-zinc mineral occurrences in core of oil-gas wells in relation to interpreted basement lithotectonic subdomains and lineaments.

9.0 CONCLUSIONS

The magnetic and gravity filter products and images and the automatic detection products derived from the 2021-2022 airborne magnetic and gravity surveys provide new insights into the basement in northern Alberta and its overlying sedimentary rocks in northern Alberta. The geological interpretation involved a high-level integration with tectonic elements documented in government and academic publications.

Care was taken to recognise cultural artefacts (predominantly oil and gas infrastructure) during the interpretation stage.

The following conclusions can be made:

- Modifications to basement domains were made by editing the tectonic domain boundaries of Ross et al. (1994) and Pilkington et al. (2000) and by dividing known domains into subdomains. The higher resolution of the new magnetic data allows for further subdivision of subdomains in the crystalline basement based on variations of internal magnetic fabrics.

- Basement anomalies were delineated. These range from small single lobe circular anomalies to larger multi-lobe rounded asymmetrical anomalies and may represent potential intrusions.

- Known ductile structures were recognized and new ductile structures were identified.

- New brittle faults were delineated. Few faults of the WCSB reported in literature show a spatial correlation with the magnetic and gravity lineaments.

- The axis of the Peace River Arch coincides with changes in direction of magnetic fabric observed in most subdomains that possibly relates to the original geometry of the continental margin. Therefore, the rise of the Peace River Arch appears to be related to a basement feature.

- Overall, the known kimberlite fields are aligned perpendicular to the curvature of the magnetic fabric that dominates the south-central part of the project area.

- The Buffalo Head Hills kimberlite field relates to a complex suite of overlapping features, including N- and NNW-trending faults, and a N-trending subdomain of variable magnetic fabric with evidence of remanence along the contact between the Buffalo High and Buffalo Utikuma subdomains. The Birch Mountains kimberlite field relates to a NW-trending basement fault crosscutting the sheared Taltson Athabasca subdomain which also shows evidence of remanence. The Mountain Lake intrusions do not clearly show a relation with major structures in the Chinchaga terrane.

- A number of known kimberlites can be positively identified in the magnetic data as high-frequency circular anomalies. Given the small size of Alberta kimberlites and abundant cultural footprint in the region, a higher resolution magnetic survey and correlation with datasets of infrastructure and imagery are needed to effectively conduct kimberlite detection.

- Basement lithotectonic elements appear to control mineralization by providing source and fluid pathways for the occurrences of helium, lithium, uranium and zinc in northern Alberta, however their relation with shallow structural elements to explain their final emplacement in the WCSB is equivocal. Local interpretations of the magnetic data would be required to get insights into the shallower structure.

- Gravity and magnetic trends are poorly correlated, possibly because the sources of the two types of anomalies are different. Gravity appears to reflect geomorphology and density contrasts between strata in the WCSB in addition to basement features, whereas magnetic trends are mostly the result of magnetic contrasts in the crystalline basement.

The integrated interpretation of the new magnetic and gravity data has identified a number of previously unrecognized features, including subdomains, shear zones, faults, fractures and intrusions underneath the WCSB of Northern Alberta that will influence future interpretations of the lithotectonic history of the basement. Local interpretations of the magnetic and gravity data are required to resolve remaining uncertainties in the geometry of basement structure and gain insights into the shallower structure. In addition, further integration with existing and new petrological, geochronological and rock property data, and integration with regional seismic and magnetotelluric data can improve the geological interpretation of the nature and architecture of the basement.

10.0 REFERENCES

Alberta Geological Survey. 2019. *3D provincial geological framework model of Alberta, Version 2.* AER/AGS Model 2018-02, Alberta Energy Regulator / Alberta Geological Survey.

—. 2023. "Alberta Aeromagnetic and Gravity Survey, Southern Alberta, Northern Alberta and Gap + Shield Surveys." https://geology-ags-aer.opendata.arcgis.com/pages/aeromag-gravity-survey.

Alberta Geological Survey. 2020. *Sediment thickness of Alberta, version 2 (gridded data, ASCII format).* AER/AGS Digital Data 2020-0023, Alberta Energy Regulator / Alberta Geological Survey.

Banas, A., Eccles, D.R. and Dufresne, M.B. (2016). 2016. *Diamond potential in Alberta: distribution of kimberlite and kimberlite indicator mineral clusters; Alberta Energy Regulator.* AER/AGS Special Report 103, 50 p. .

Branscombe, P. 2017. *Precambrian basement top surface in Alberta (elevation) (gridded data, ASCII format).* Digital Data 2016-0045, Alberta Energy Regulator, AER/AGS.

Brem, A., Lopez, G., McGill, D., and McKenzie, J. 2024. "Geological Interpretation of the 2022-2023 Aeromagnetic Data - Southern Alberta, Canada."

Burwash, R.A., J. Krupička, and J.R. Wijbrans. 2000. "Metamorphic evolution of the Precambrian basement of Alberta." *The Canadian Mineralogist* v. 38, p. 423–434.

Burwash, R.A., McGregor, C.R., Wilson, J.A. and O'Connell, S.C. 1994. "Chapter 5: Precambrian Basement." In *Geological Atlas of the Western Canada Sedimentary Basin*, by G.D. Mossop and I. Shetsen (comp.), p. 48-56. Canadian Society of Petroleum Geologists and Alberta Research Council. https://ags.aer.ca/atlas-the-western-canada-sedimentary-basin/chapter-5-precambrian-basement.

Cotterill, D.K. and Hamilton, W.N. 1995. *Geology of Devonian limestones in northeast Alberta.* ARC/AGS Open File Report 1995-07, 91 p., Alberta Research Council.

Cutts, J.A., Dyck, B., Davies, J. and Stern, R. 2022. "Tectonic setting and provenance of plutonic rocks hosting the Great Slave Lake shear zone from microanalytical zircon U-Pb geochronology and oxygen and hafnium isotopes." *GAC-MAC-IAH-CNC-CSPG 2022 Halifax Meeting: Abstracts, 45, p. 94.*

Danabalan, D., Gluyas, J.G., Macpherson, C.G., Abraham-James, T.H., Bluett, J.J., Barry, P.H., and Ballentine, C.J. 2022. "The principles of helium exploration." *Petroleum Geoscience, v. 28, Issue 2* petgeo2021-029, 13 pages.

Davies, G.R., and L.B. Smith Jr. 2006. "Structurally controlled hydrothermal dolomite reservoir facies; an overview." *AAPG Bulletin* v.90, p. 1641-1690.

Davies, G.R., Watson, N., Moslow, T.F., and MacEachern, J.A. 2018. "Regional subdivisions, sequences, correlations and facies relationships of the Lower Triassic Montney Formation, west-central Alberta to northeastern British Columbia, Canada — with emphasis on role of paleostructure." *Bulletin of Canadian Petroleum Geology* v. 66, pp. 23-92.

Dufresne, M.B., D.R. Eccles, B. McKinstry, D.R. Schmitt, Fenton, Pawlowicz, J.G. M.M., and W.A.D. Edwards. 1996. "The diamond potential of Alberta." Alberta Energy, AE/AGS Bulletin 63, 164 p.

Eaton, D.W., B. Milkereit, G.M. Ross, E.R. Kanasewich, W. Geis, D.J. Edwards, L. Kelch, and J. Varsek. 1995. "Lithoprobe basin-scale profiling in central Alberta: influence of basement on the sedimentary cover." Bulletin of Canadian Petroleum Geology, v. 43, p. 65-77.

Eaton, D.W., G.M. Ross, and J. Hope. 1999. "The rise and fall of a cratonic arch: a regional perspective on the Peace River Arch, Alberta." *Bulletin of Canadian Petroleum Geology* v. 47, no. 4: p. 346–361.

Eccles, D.R. 2011. *Northern Alberta kimberlite province: the first 20 years.* ERCB/AGS Bulletin 65, 119 p., Energy Resources Conservation Board.

Eccles, D.R., E.C. Grunsky, M. Grobe, and J.A. Weiss. 2002. *Structural-emplacement model for kimberlitic diatremes in northern Alberta.* Earth Sciences Report 2000-01, 114 p., Alberta Energy and Utilities Board, ARC/AGS.

Ekpo, E., D. Eaton, and R. Weir. 2017. *Basement Tectonics and Fault Reactivation in Alberta Based on Seismic and Potential Field Data.* (https://www.intechopen.com/chapters/58517).

Hauck, T.E., and H. Corlett. 2017. "Precambrian basement top picks in Alberta (elevation) (tabular data, tab-delimited format)." Alberta Energy Regulator, AER/AGS Digital Data 2016-0043. (https://ags.aer.ca/publication/dig-2016-0043).

Hoffmann, P.F. 1988. "United plates of America, the birth of a craton, Early Proterozoic assembly and growth of Laurentia." Annual Review of Earth and Planetary Science Letters, v. 16, p. 543–603.

Hope, J., D.W. Eaton, and G.M. Ross. 1999. "Lithoprobe seismic transect of the Alberta Basin: Compilation and overview." Bulletin of Canadian Petroleum Geology, v. 47, no. 4, p. 331-345.

Huff, G.F. 2019. *Origin and Li-enrichment of selected oilfield brines in the Alberta Basin, Canada.* AER/AGS Open File Report 2019-01, 29 p., Alberta Geological Survey / Alberta Energy Regulator.

Isles, D. J., and L. R. Rankin. 2013. *Geological interpretation of aeromagnetic data.* Australian Society of Exploration Geophysicists, 365 p.

Kovesi, P. 2015. *Good Colour Maps: How to Design Them (colorcet.com).* Accompanying Document, Crawley, Western Australia: Centre for Exploration Targeting, The University of Western Australia. (https://colorcet.com/).

Lopez, G., D. McGill, and J. McKenzie. 2024. "Geological Interpretation of the 2021 Aeromagnetic Data - Canadian Shield, Alberta." Prepared for the Alberta Geological Survey, 113 p.

Lopez, G.P., J.G. Pawlowicz, J.A. Weiss, and G.M. Jean. 2020. *Metallic Mineral Occurrences of Alberta (tabular data, tab-delimited format).* AER/AGS Digital Data 2019-0026., Alberta Energy Regulator / Alberta Geological Survey.

Lyatsky, H.V., D.I. Pană, and M. Grobe. 2005. "Basement structure in central and southern Alberta; insights from gravity and magnetic maps." Alberta Energies and Utilities Board/Alberta Geological Survey, Special Report 72, 83 p.

Lyster, S., G.P. Lopez, and S. Poulette. 2022. *Geochemistry data of lithium-bearing groundwater in the Alberta Basin compiled from multiple sources (tabular data, tab-delimited format)* . Digital Data 2021-0021., Alberta Energy Regulator / Alberta Geological Survey.

Lyster, S., P. Branscombe, A. Singh, C.D. Rokosh, and C. Filewich. 2021. *Helium concentrations from natural gas analysis tests in Alberta.* AER/AGS Information Series 153, 1 p., Alberta Energy Regulator / Alberta Geological Survey.

Mazur, M.J. 1999. "Seismic characterization of meteorite impact craters." M.Sc. Thesis, University of Calgary, 176 p.

McDonough, M.R., V.J. McNicoll, E.M. Schetselaar, and T.W. Grover. 2000. "Geochronological and kinematic constraints on crustal shortening and escape in a two-sided oblique-slip collisional and magmatic orogen, Paleoproterozoic Taltson magmatic zone, northeastern Alberta." (Canadian Journal of Earth Sciences) v. 37, no. 11: p. 1549–1573.

McGregor, M., E. Walton, C. Mcfarlane, and J. Spray. 2020. "Multiphase U-Pb geochronology of sintered breccias from the Steen River impact structure, Canada: Mixed target considerations for a Jurassic-Cretaceous boundary event." *Geochimica et Cosmochimica Acta. v. 274,.*

McKenzie, J., E. Ronacher, and F. Farahani. 2021. "Interpretation of Geophysical Data, Alberta Geological Survey: He and Li project." Alberta Energy Regulator/ Alberta Geological Survey, AER/AGS Special Report 114, 35 p., 36 p.

Molak, B., S.A Balzer, Olson, R.A., and E.J. Waters. 2001. *Petrographic, mineralogical and lithogeochemical study of core from three drillholes into the Steen River structure, northern Alberta;.* Earth Sciences Report 2001-04, Alberta Energy and Utilities Board, EUB/AGS, 89 p.

Mossop, G.D., and I. Shetsen. 1994. "Geological Atlas of the Western Canada Sedimentary Basin." *Alberta Geological Survey.* Canadian Society of Petroleum Geologists and Alberta Research Council. Accessed October 30, 2023. https://ags.aer.ca/reports/atlas-western-canada-sedimentary-basin.

Okulitch, A.V. 2006. *Bedrock geology, Peace River, Alberta.* Open File 5282, Geological Survey of Canada.

Pană, D.I. 2007. "A two-stage thermotectonic model for the Athabasca unconformity-type uranium deposits; in Digging deeper." *Society for Geology Applied to Mineral Deposits.* Dublin, Ireland: C.J. Andrew (ed.) v. 2. p. 1133-1136.

Pană, D.I. 2003. *Precambrian basement of the Western Canada Sedimentary Basin in northern Alberta.* Earth Sciences Report 2002-02, 39 p., Alberta Energy and Utilities Board, EUB/AGS, 39 p.

Pană, D.I. 2010. "Precambrian geology of northeastern Alberta (NTS 74M, 74L and part of 74E)." Energy Resources Conservation Board, ERCB/AGS Map 537.

Pană, D.I. 2003. *Structural control of lead-zinc mineralization in carbonate sequences of northern Alberta: a contribution to the carbonate-hosted Pb-Zn (MVT) targeted geoscience initiative*. EUB/AGS Geo-Note 2002-15, Alberta Energy and Utilities Board.

Pană, D.I., and E. J. Waters. 2016. *GIS compilation of structural elements in Alberta, version 3.0 (GIS data, line features).* Digital Data 2003-0012, Alberta Energy Regulator/Alberta Geological Survey.

Pană, D.I., and R.A. Olson. 2009. *Overview of uranium exploration work along the northern rim of the Athabasca Basin, northeastern Alberta.* ERCB/AGS Open File Report 2009-19, Energy Resources Conservation Board, 50 p.

Pană, D.I., R. Elgr, E.J. Waters, J.A. Warren, G.P. Lopez, and J.G. Pawlowicz. 2021. "Structural elements in the Alberta Plains." Alberta Energy Regulator/Alberta Geological Survey, AER/AGS Open File Report 2021-01, 33 p.

Pană, D.I., Waters, J., and Grobe, M. 2001. "GIS compilation of structural elements in northern Alberta, release 1.0." Alberta Energy and Utilities Board, EUB/AGS Earth Sciences Report 2001-01, 60 p.

Peirce, J.W., Cordsen, A., and Glenn, T. n.d. *The Great Slave Lake Shear Zone – Implications for Exploration in NW Alberta and NEBC.* Accessed March 2024. (https://chad-data.com/#publications).

Pilkington, M., W.F. Miles, G.M. Ross, and W.R. Roest. 2000. "Potential-field signatures of buried Precambrian basement in the Western Canada Sedimentary Basin." Canadian Journal of Earth Sciences, v. 37, p. 1453-1471.

Post, R. T. 2004. "Stratigraphy and sedimentology of the Athabasca Group in the Net Lake-Maybelle River area, northeastern Alberta." Alberta Energy and Utilities Board, EUB/AGS Earth Sciences Report 2003-01, 103 p.

Prior, G.J., B. Hathaway, P. Glombick, D.I. Pană, C.J. Banks, D.C. Hay, C.L. Schneider, M. Grobe, R. Elgr, and J.A. Weiss. 2013. "Bedrock geology of Alberta." Alberta Energy Regulator / Alberta Geological Survey, AER/AGS Map 600.

Ramaekers, P. 2004. "Development, stratigraphy and summary diagenetic history of the Athabasca Basin, early Proterozoic of Alberta and its relation to uranium potential." Alberta Energy and Utilities Board, EUB/AGS Special Report 62, 94 p.

Ramaekers, P., C. W. Jefferson, G. M. Yeo, B. Collier, D. G.F. Long, O. Catuneanu, S. Bernier, et al. 2007. "Revised geological map and stratigraphy of the Athabasca Group, Saskatchewan and Alberta; in EXTECH IV: geology and uranium EXploration TECHnology of the Proterozoic Athabasca Basin." Bulletin of the Geological Survey of Canada 588, p. 155-191.

Ross, G.M., and D.W. Eaton. 2002. "Proterozoic tectonic accretion and growth of western Laurentia: results from Lithoprobe studies in northern Alberta." *Canadian Journal of Earth Sciences* v. 39, p 313-329.

Ross, G.M., B. Milkereit, D Eaton, White, D., E.R. Kanasewich, and M.J.A. and Burianyk. 1995. "Paleoproterozoic collisional orogen beneath the western Canada sedimentary basin imaged by Lithoprobe crustal seismic-reflection data." *Geology, v. 23,* p. 195-199.

Ross, G.M., J. Broome, and W. Miles. 1994. "Chapter 4: Potential fields and basement structure." In *Geological Atlas of the Western Canada Sedimentary Basin*, by G.D. Mossop and I. Shetsen (comp.), p. 41–47. Canadian Society of Petroleum Geologists and Alberta Research Council.

Ross, G.M., R.R. Parrish, M.E. Villeneuve, and S.A. Bowring. 1991. "Geophysics and geochronology of the crystalline basement of the Alberta Basin, western Canada." *Canadian Journal of Earth Sciences, v. 28,* p. 512–522.

Šilerová, D., B. Dyck, J. A. Cutts, and K. Larson. 2023. "Long-lived (180 Myr) ductile flow within the Great Slave Lake shear zone." *Tectonics, v. 42, e2022TC007721.*

Skelton, D., and D. Willis. 2002. "Assessment report for the Buffalo Hills property, 2002; Ashton Mining of Canada Inc." Alberta Energy, Mineral Assessment Report 20020010, 279 p.

Thiessen, R. 1986. "Two-dimensional refold interference patterns." *Journal of Structural Geology* Vol. 8, (Issue 5,): p. 563-573.

Villeneuve, M.E., G.M. Ross, R.J. Thériault, W. Miles, R.R. Parrish, and J. Broome. 1993. "Tectonic subdivision and U-Pb geochronology of the crystalline basement of the Alberta Basin, western Canada." Geological Survey of Canada Bulletin 447, 95 pages.

Walton, E., A. Hughes, E. MacLagan, C. Herd, and M. Dence. 2017. "A previously unrecognized high-temperature impactite from the Steen River impact structure, Alberta, Canada." *Geology, v. 45,.*

Wozniakowska, P., D.W. Eaton, C. Deblonde, A. Mort, and O.H. Ardakani. 2021. "Identification of regional structural corridors in the Montney play using trend surface analysis combined with geophysical imaging, British Columbia and Alberta." Geological Survey of Canada, Open File 8814, 65 p.

Wright, G.N., McMechan, M.E., Potter, D.E.G., and Holter, M.E. 1994. "Chapter 3: Structure and Architecture." In *Geological Atlas of the Western Canada Sedimentary Basin*, by (comp.) G.D. Mossop and I. Shetsen, p. 25-40. Canadian Society of Petroleum Geologists and Alberta Research Council.

Appendix 1 – Automatic detection - Fathom Geophysics Report

Processing of the Northern Alberta magnetic survey for Ronacher McKenzie Geoscience

March 2024

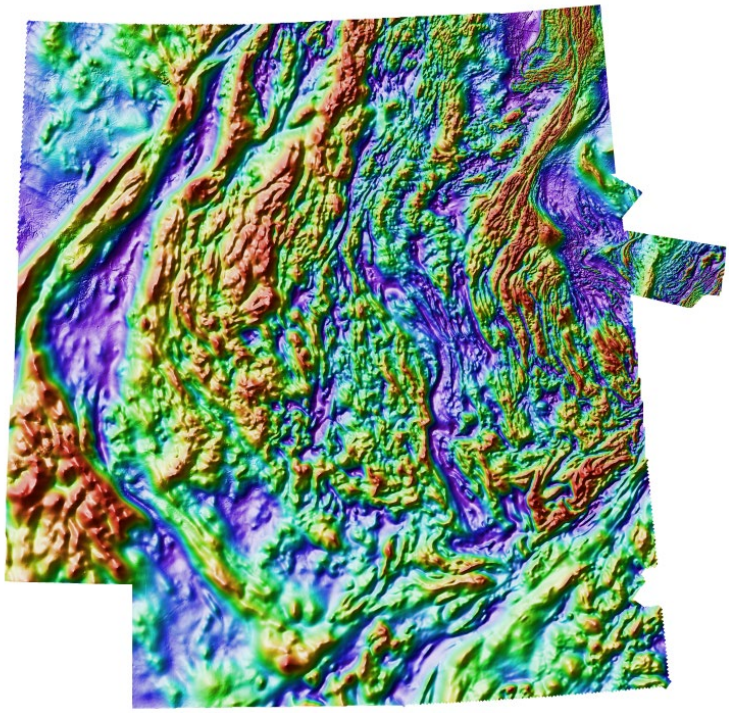

by Dan Core†, Eric Core and Lisa Lombardi
Fathom Geophysics

†Corresponding author: dan@fathomgeophysics.com

Introduction

The project area for this work is the Northern Alberta magnetic survey from the Alberta Geological Survey (AGS) (**Figure 1**). The goal of this work is to process the magnetic data to generate products that can assist with interpretation of structure and lithology based on the magnetic data.

The magnetic data are from a survey flown in 2021 and 2022 by EON Geosciences Inc on behalf of the Alberta Energy Regulator. Gridded data provided with the survey were good quality and were supplied to us with coordinates in WGS84 UTM Zone 11N (**Figure 2**)**.** All outputs of our work use this coordinate system. Survey data have 800m line-spacing. All gridded products use a cell size of 200m.

The processing completed includes application of a suite of standard filters and depth-to-magnetic source processing as well as application of Fathom Geophysics' structure detection and radial symmetry filters.

Processing summary

Reduction to the pole (RTP)

RTP processing produces a magnetic field that is equivalent to what would be generated if the data were collected at the magnetic north pole. This shifts magnetic highs to be directly over their sources and creates symmetric anomalies over the top of symmetric magnetic sources. The RTP filter for these data uses an inclination of 77.2° and a declination of 15.3° (**Figure 3**).

Note that in general RTP processing is not valid for remanent bodies unless the remanence is directly opposed to the present-day field. The dataset almost certainly contains some remanent bodies that will not be corrected properly using the RTP filter. However, it is worthwhile applying the filter because most of the anomalies in the area are normally magnetized or reversely magnetized with relatively few anomalies possessing an apparent magnetization direction at a high angle to the present-day field.

Magnetic standard filtering

The RTP grid was filtered with a suite of standard geophysical filters including the analytic signal and vertical derivative. These grids were imaged using our in-house software to produce shaded images with the sunlight coming from the northeast or northwest (NE or NW in the filename). Unshaded images were also produced so that the geographic location of pertinent features in the data can be readily defined (because shaded images can 'fool the eye' in this respect).

Processing summary — Magnetic data

Magnetic standard filtering (continued)

Figures 4 to 22 show images of most of the standard filtering results supplied. Standard filtering results have been included in this report because of their capacity to help the reader who might be new to the delivered processing results files to quickly grasp the project area's overall magnetic susceptibility changes/contrasts.

Magnetic total structure detection

Structure detection was applied to highlight edges in the RTP magnetic data and the AGC of the RTP data. Edges in potential field data are locales that are more likely to be faults, contacts or other structures. The structure detection algorithm and processing are described in more detail in **Appendix 1**.

Representative images of the total structure detection filtering are shown in **Figures 23 and 24** for the RTP data and **Figures 25 and 26** for the AGC of the RTP. Further results files were delivered in addition to those visualized within this report, and we urge the reader to explore the entire series of results files to ensure full familiarity with the results of total structure detection processing and their possible exploration ramifications.

Total-structure detection filtering was applied to the RTP grid at minimum wavelengths of 200m, 400m, 800m, 1600m, 3200m, 6400m, and 12800m. The RTP-derived total-structure detection results are good at depicting relatively long-wavelength features. Structure intersection images were supplied alongside structure images.

This filtering was also applied to the AGC grid at minimum wavelengths of 200m, 400m, 800m, 1600m, 3200m, and 6400m. The AGC-derived total-structure detection results are good at depicting relatively detailed features as well as highlighting features in quiet parts of the dataset. Structure intersection images were supplied alongside structure images.

The RTP results show that the central part of the area is dominated by WNW-trending to north-south trending structures that bend around to be NNE-trending in the northern part of the dataset. The southeast is dominate by ENE-trending features and looks like a different structural block. Significant east-west trending structures are present throughout. The orientations of structures seem to stay consistent across scales.

The AGC results show similar results to the RTP overall. However, they do a better job of highlighting detailed features. The AGC results are also good for seeing different structural domains. The contrast between the central and northern parts of the area is more apparent in the AGC results.

Processing summary — Magnetic data (continued)

Magnetic total structure detection (continued)

The intersection maps show where structures of different orientations are collocated. Areas with a high density of intersections are likely to be more structurally complex and therefore may be more likely to host mineralization.

Magnetic belt-parallel and belt-crossing structure detection

In many heavily deformed belts, the fabric-parallel and fabric-crossing structures can be different structure types and may have different timing. The fabric-parallel features tend to be contacts or belt-parallel shear zones. The cross structures are usually not contacts and are more likely to be faults. Any sense of motion is possible on the cross structures. If clear lateral offset of the units is present, the faults are likely strike-slip faults. Normal and reverse faults are often represented by a change in amplitude or frequency content of the magnetic data.

The first step in extracting fabric-parallel and fabric-crossing structures is to extract the fabric orientation. The AGC was used for determining the fabric orientation because it was better at delineating the different structural domains than the RTP did (**Figure 27**). The results are dominated by NW to NNW-trending features in the central part of the area bending around to NNE-trending in the northern part of the area. The southeast is dominated by NE-trending units.

Representative images of the results of parallel and cross structure detection are shown in **Figures 28 and 29** for the RTP data and **Figures 30 and 31** for the AGC of the RTP data. The wavelengths that were run are the same as for the total structure. At longer wavelengths, the original fabric orientation maps are smoothed so that larger-scale structures do not get broken up by rapid changes in the fabric orientation.

The fabric-parallel structures should be useful for highlighting lithological contacts and fabric parallel shear zones. The AGC results appear to be useful for highlighting lithological boundaries. The fabric-crossing structures are likely to be faults. The RTP results are likely more useful for cross structures because there is a lower density of features meaning that the features that are present are more likely to be significant.

Further results files were delivered in addition to those visualized within this report, and we urge the reader to explore the entire series of results files to ensure full familiarity with the results of belt-parallel and belt-crossing structure detection processing and their possible exploration ramifications.

Processing summary — Magnetic data (continued)

Magnetic radial symmetry

The radial symmetry detection filter can highlight discrete, equant magnetic features with different radii. These features indicate areas that are more likely to host intrusive rocks or discrete alteration zones. Radial symmetry detection was completed on the RTP magnetic data. The radial symmetry algorithm is described in greater detail in **Appendix 2** of this report.

Representative images of the radial symmetry results are shown in **Figures 32**. Further results files were delivered in addition to those visualized within this report, and we urge the reader to explore the entire series of results files to ensure full familiarity with the results of radial symmetry analysis processing and their possible exploration ramifications.

Radial symmetry detection processing was applied to the RTP grid in magnitude-independent mode at minimum-radius runs of 500m, 1000m, 2000m, 4000m, 8000m, and 16000m. Radii smaller and larger than these did not appear to be useful on this dataset. Both magnetic highs and magnetic lows represent meaningful/useable results and therefore are presented in images. The smallest radius results are most likely only valid in the eastern third of the dataset. The western part of the dataset is buried by too much sediment too allow the detection of small-scale features.

Note that in order to obtain optimal results it was necessary to take a residual (i.e., carry out differential upward continuation) prior to running radial symmetry detection at a given minimum radius. It was found that a residual involving levels going from on quarter the minimum radius to four times the minimum radius enable the production of satisfactory radial symmetry detection results (e.g., for the 2000m radial symmetry detection run, a 500m-8000m residual was carried out first).

The results in **Figure 32** show that parts of the central and eastern part of the dataset have very few intrusions detection. There appears to be a belt following the main structural fabric just west of the central part of the dataset that has the most intrusions. This area is completely under cover, so it is difficult to assess whether these results are real or if they are being caused by the data being smoother because it is under cover. Smoother data will generally show more round features.

Reversely magnetized bodies will be highlighted as radially symmetric lows in this analysis. Any lows that correspond with highs in the analytic signal are likely to be reversely magnetized.

Processing summary — Magnetic data (continued)

Depth to magnetic source

Many algorithms can be used to estimate the depth to magnetic sources. Most are based on at least second order derivatives making them significantly influenced by any kind of noise in the data.

This dataset presents some significant challenges for these algorithms due to high frequency noise that occurs where cultural features are present in the data. These features are mostly due to oil and gas infrastructure in the area. While the airborne contractor took steps to mitigate the noise caused by these features, the effects were not completely removed. These features are most abundant in the western part of the dataset.

In order to smooth out these features, a localized Gaussian filter was applied only where the high-frequency noise was a problem. This had to be done rather than using a global filter because a global filter would have smoothed out real detail in the east.

The method that was used for the depth to source is that of Cooper (2014). It involves looking at the derivative of the tilt angle to estimate the depth of contacts in the dataset. The resulting depths were then interpolated to generate a continuous distance to magnetic source grid. The average altitude of the aircraft was subtracted off to generate a depth to magnetic basement grid.

The results of the depth to magnetic source processing are shown in **Figure 33**. The smoother parts of the dataset show greater depth to source as is expected. The results show that the basement surface gets deeper to the west and that it appears to be exposed in the northeast.

The average depths observed in the depth to source processing are similar to those observed in wells that have pierced the basement in parts of the area. The correlation between the well depths and the calculated basement depths are reasonably good indicating that the depth to source appears to be a good estimate.

The depth to magnetic source grid was subtracted from the topography data to generate a top of magnetic basement surface (**Figure 34**)**.** The magnetic basement surface looks almost like an inverse of the depth to source grid. This is expected given the relatively small amount of topographic variation in the area.

*Cooper (2014) The automatic determination of the location, depth, and dip of contacts from aeromagnetic data. Geophysics, v79, pp J35-J41. https://library.seg.org/doi/10.1190/geo2013-0181.1

File formats and image types delivered

The grids for this work have been delivered in ER Mapper ERS format. All images have been provided in GeoTIFF format with associated MapInfo TAB files and ESRI world files. Vectors have been delivered in ESRI shapefile format.

Structure detection results have been supplied as grids, images (GeoTIFF), and polylines (vectorization of the gridded results). The polylines have been attributed with the values from the structure detection grid and the orientation of the structure calculated based on the vectorized result.

Structure images were made in an unshaded fashion using a warm color bar (yellows through to reds) and a linear color stretch. Shaded structure images cycle through colors starting from purple and blue (lows) through to reds (highs) and were made with a histogram-equalized color stretch. Dominant orientation images use a wraparound colorbar palette that produces the same color for 0 and 180 with a rainbow distribution for colors in between. Those orientation images that have been thresholded display only significant features and are white in locales that essentially lack structure.

Radial symmetry 'lows and highs' images were made using a blue-and-red color bar possessing no intermediate colors. Highs-only images use the red side of that same color bar, and lows-only images use the blue side.

Several ternary images were also created for this work. These images are generated using three separate grids to represent the red-green-blue (RGB) or cyan-magenta-yellow (CMY) channels of the output image. RGB ternary images involve color addition, analogous to how different-colored light beams combine on a performance stage. When all three channels are present in full strength, pure white is the result. (Pure black indicates all three channels are absent.) CMY ternary images involve color subtraction, similar to colors resulting from the mixing of paint pigments. When all three channels are present in full strength, pure black is the result. (Pure white indicates all three channels are absent.) **Figure 17** explains in more detail how to interpret the full gamut of colors that can turn up in ternary images.

See also the list of abbreviations and acronyms supplied in this report to help decode the information contained within a given grid/image filename.

List of acronyms and abbreviations

agc	automatic gain control (appears in delivered file names)
agc30	AGC when standard deviation=30 (in file names)
asig	analytic signal (appears in delivered file names)
colorbar	numerical values associated with image's color range (in file names)
Cross	structures that are perpendicular or oblique to the magnetic stratigraphic fabric
CMY	cyan-magenta-yellow ternary (appears in delivered file names)
hgm	horizontal gradient magnitude (appears in delivered file names)
Highs	positive anomalies-only radial symmetry image (in file names)
HSI	hue, saturation and intensity (appears in delivered file names)
HTh	hysteresis thresholding was used during vectorization (in file names)
Int	structural intersections image (appears in delivered file names)
LgeRes	large-scale residual (appears in delivered file names)
lin	linear-stretch image (appears in delivered file names)
Lows	negative anomalies-only radial symmetry image (in file names)
LowsAndHighs	negative and positive anomalies radial symmetry image (in file names)
md	magnitude dependent radial symmetry result (in file names)
MedRes	medium-scale residual (appears in delivered file names)
Mi	magnitude independent radial symmetry result (in file names)
NAB	Northern Alberta project area
OriDom	dominant orientation image (appears in delivered file names)
Para	Structures that are parallel to the magnetic stratigraphic fabric
Pgrav	pseudogravity (appears in delivered file names)
PgravRes	residual of pseudogravity (appears in delivered file names)
PgravResHGM	HGM of residual of pseudogravity (appears in delivered file names)
res	residual (appears in delivered file names)
res25_100	25m-100m residual (appears in delivered file names)
RGB	red-green-blue ternary (appears in delivered file names)
RMI	residual magnetic intensity (appears in delivered file names)
RSym	radial symmetry image (appears in delivered file names)
RSym100	100m minimum radius radial symmetry image (in file names)
RTP	reduced-to-pole (appears in delivered file names)
SmRes	small-scale residual (appears in delivered file names)
Struct	structure image (appears in delivered file names)
Struct100	100m minimum wavelength structure image (in file names)
tern, ternary	ternary image (appears in delivered file names)
Thresh, thr, Th	image made via thresholding (appears in delivered file names)
tilt	tilt angle (appears in delivered file names)
TMI	total magnetic intensity (appears in delivered file names)
Total	total structure image (appears in delivered file names)
vd	vertical derivative (a.k.a. 1VD) (appears in delivered file names)

List of acronyms and abbreviations (continued)

vdmhgm	vertical derivative minus HGM (appears in delivered file names)
Vec	vectorized results file (appears in delivered file names)
vias	analytic signal of vertical integral (appears in delivered file names)
vint	vertical integral (appears in delivered file names)
X	directional derivative along X axis (appears in delivered file names)
Y	directional derivative along Y axis (appears in delivered file names)
Z	directional derivative along Z axis (i.e., vertical derivative) (in file names)

Project location map

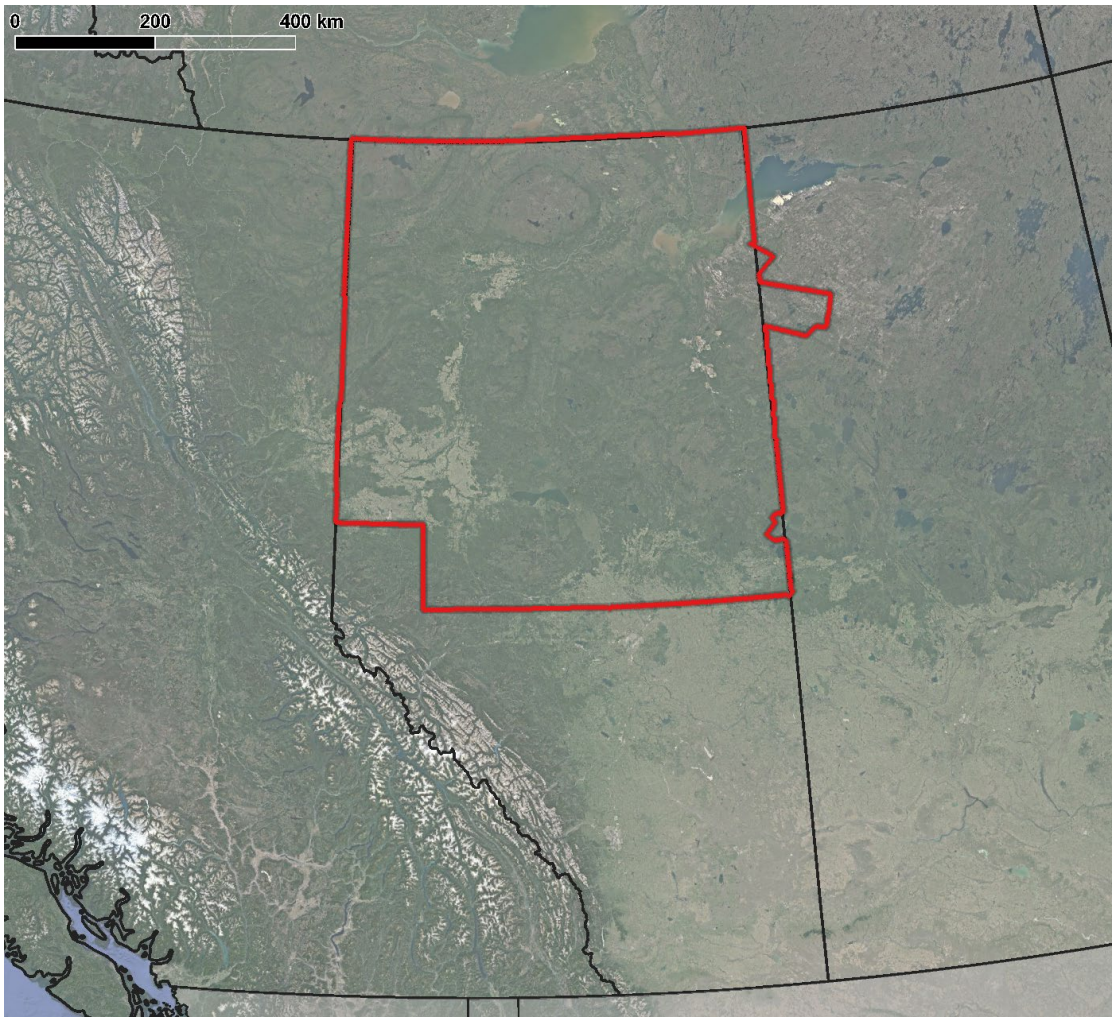

Figure 1: Map showing the location of the project area in Northern Alberta.

Magnetic data-processing results images
▶ Residual magnetic intensity (RMI)

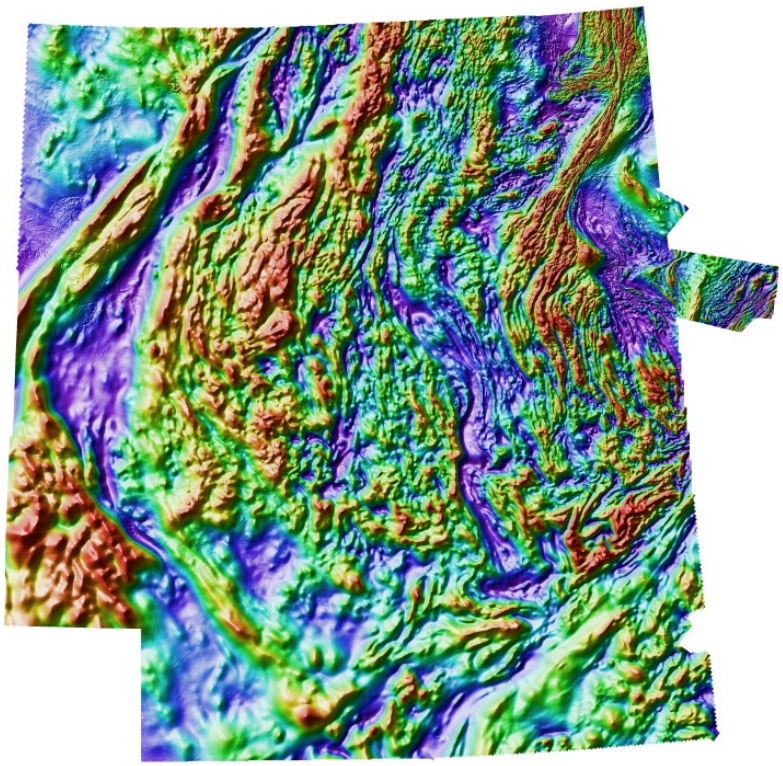

2022_NAB_RMI_HSI_NW

Figure 2: Residual magnetic intensity data for the project area. The indicative colorbar shown applies to all magnetic data-processing results images involving the HSI (hue, saturation, intensity) color display system.

Magnetic data-processing results images
▶ Reduction-to-pole (RTP)

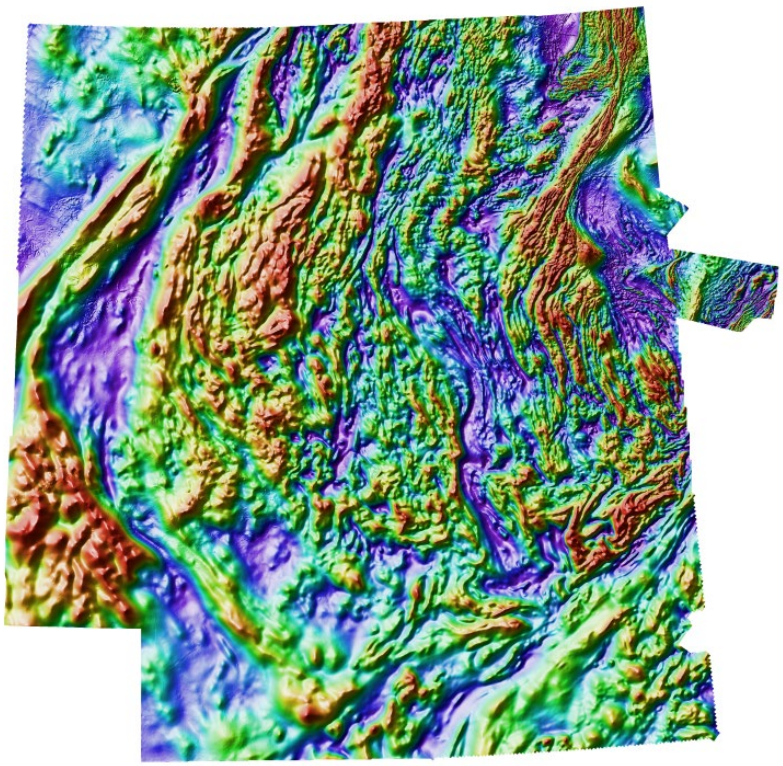

2022_NAB_RMI_RTP_HSI_NW

Figure 3: Reduced-to-the-pole magnetic data for the project area. The RTP filter attempts to produce the magnetic field that would be expected if the data were collected at the magnetic pole.

Magnetic data-processing results images (continued)
▶ Standard filtering — First vertical derivative

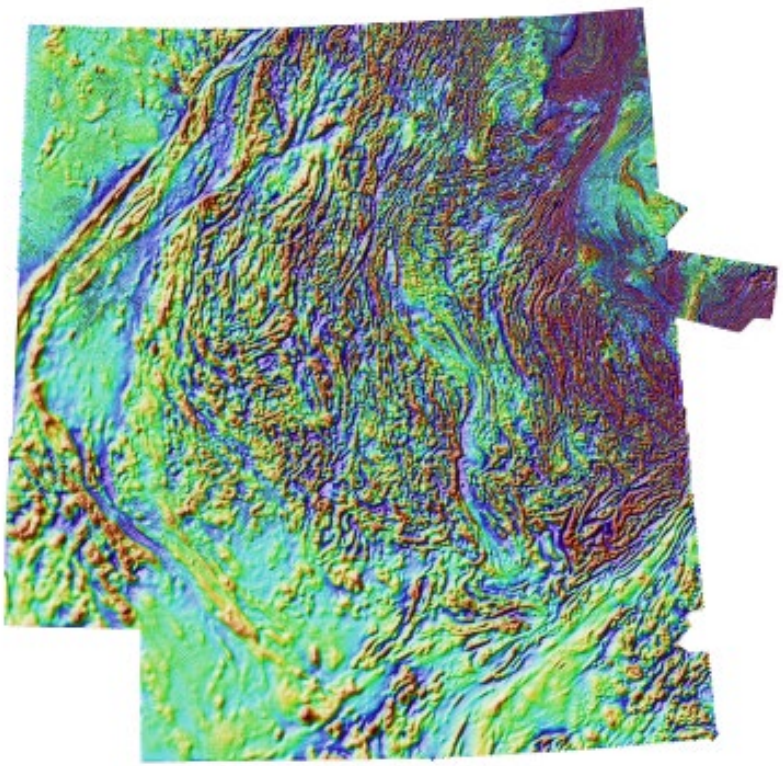

2022_NAB_RMI_RTP_vd_HSI_NW

Figure 4: The first vertical derivative (1VD) transform is the rate of change of the potential field in the vertical direction. Application of this filter has the effect of accentuating the shorter wavelength (higher frequency) components at the expense of longer wavelength (more regional) features.

Magnetic data-processing results images (continued)
▶ Standard filtering — Horizontal gradient magnitude

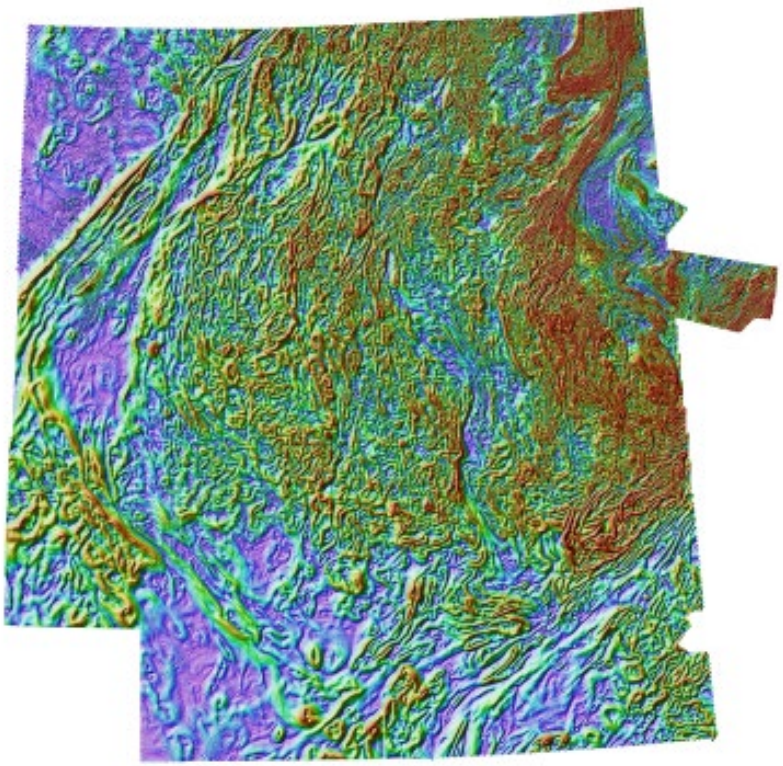

2022_NAB_RMI_RTP_hgm_HSI_NW

Figure 5: The horizontal gradient magnitude is calculated from the x- and y-derivatives of the data ($\sqrt{dx^2 + dy^2}$). This filter highlights the location of steep gradients in the data. Peaks in the HGM should occur at susceptibility contrasts in magnetic data and density contrasts in gravity data. These are likely to be locations of faults or contacts. Peaks will be offset in the down-dip direction for dipping bodies. The results are affected by remanent magnetization.

Magnetic data-processing results images (continued)
▶ Standard filtering — Vertical derivative minus HGM

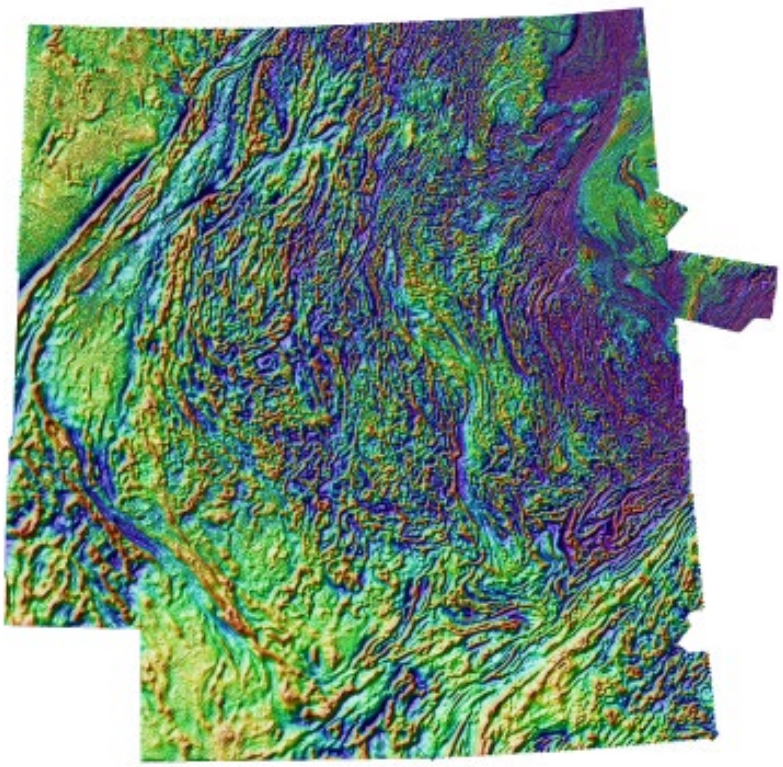

2022_NAB_RMI_RTP_vdmhgm_HSI_NW

Figure 6: The vertical derivative minus the HGM (VDMHGM) is a filter that accentuates the contrast in the first vertical derivative. This is useful for highlighting shallow sources in potential field data. It can also be useful when trying to pick the exact location to place a narrow magnetic unit or a narrow dense unit.

Magnetic data-processing results images (continued)
▶ Standard filtering — Tilt angle

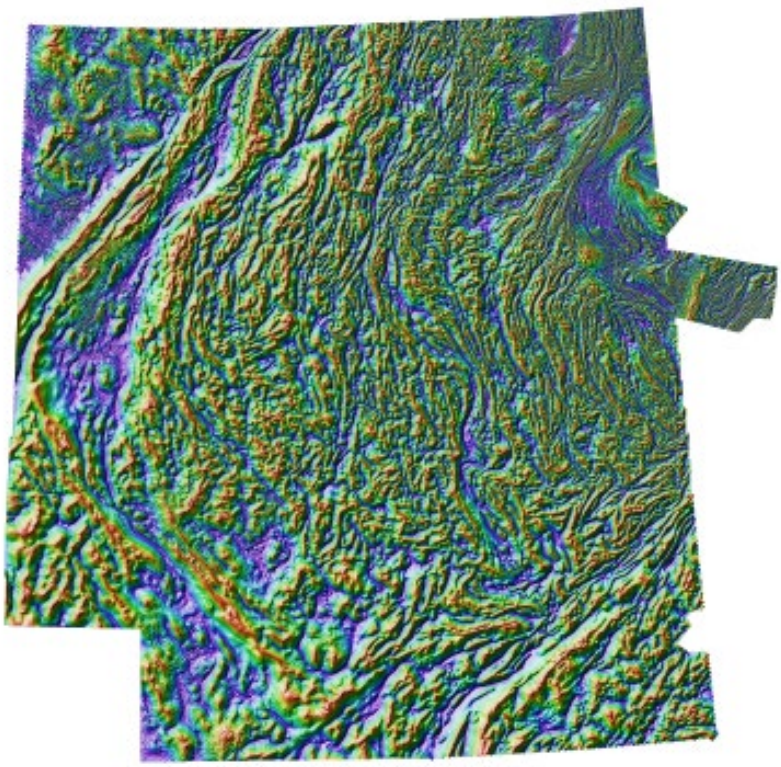

2022_NAB_RMI_RTP_tilt_HSI_NW

Figure 7: The tilt angle filter is the arctangent of the ratio of the vertical derivative to the horizontal gradient magnitude. This filter removes information about the amplitude of the signal, making the heights of peaks the same regardless of the susceptibility or density of the causative body. Structure and depth information are preserved. This makes it easier to see subtle features and some structures.

Magnetic data-processing results images (continued)

▶ Standard filtering — Analytic signal

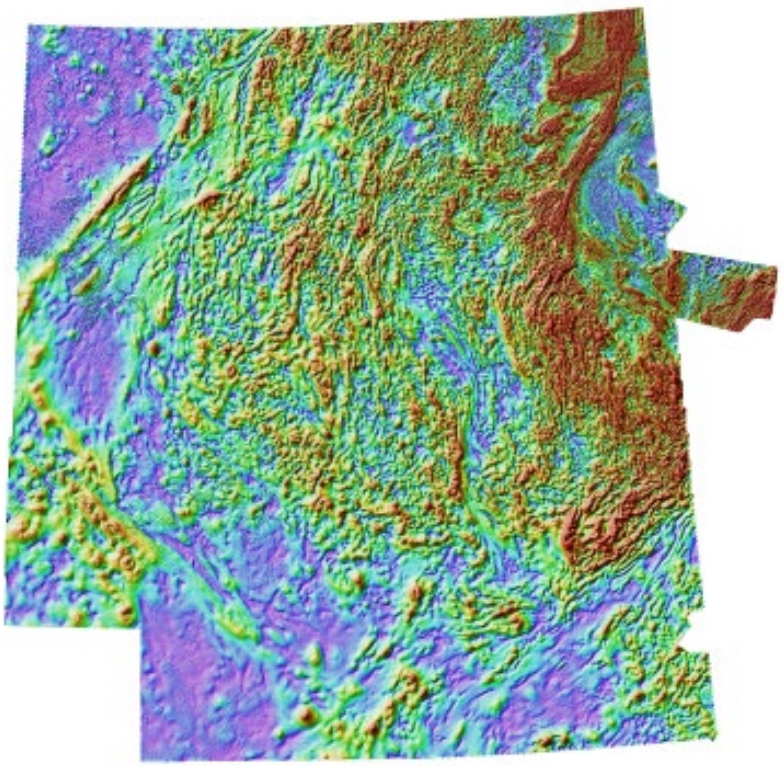

2022_NAB_RMI_RTP_asig_HSI_NW

Figure 8: Analytic signal of the RTP data. The analytic signal (also known as the total gradient magnitude) is calculated as $\sqrt{dx^2 + dy^2 + dz^2}$. This filter highlights the location of rapid changes in the data. Highs in the analytic signal correspond to high amplitudes in the vertical derivative (positive or negative) or high amplitudes in the horizontal gradient magnitude. Highs will occur over the top of small bodies with high susceptibility or high density contrast or at the edge of large-scale susceptibility or density contrast. Long-wavelength features are suppressed by this filter since it is based on derivative filters. This filter is relatively independent of magnetization direction and remanent magnetization.

Magnetic data-processing results images (continued)
▶ Standard filtering — Analytic signal of vertical integral

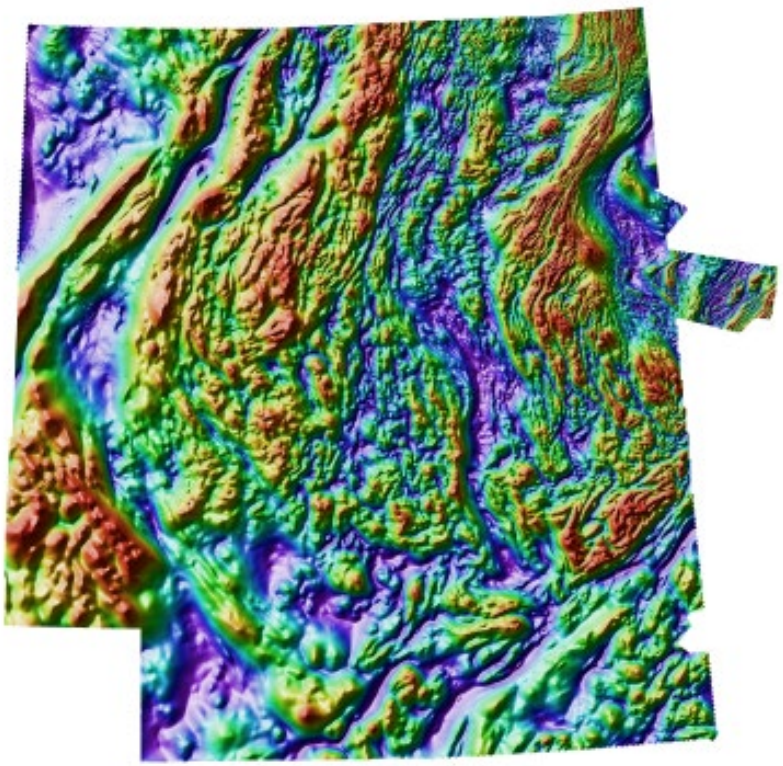

2022_NAB_RMI_RTP_vias_HSI_NW

Figure 9: The analytic signal filter was applied to the vertical integral of the magnetic data to produce this VIAS result. The analytic signal filter is described in the caption of **Figure 8**. This processing produces a grid with wavelength and amplitude characteristics that are similar to the RTP grid, but with reduced effects of remanent magnetization and magnetization direction.

Magnetic data-processing results images (continued)
▶ Standard filtering — Automatic gain control

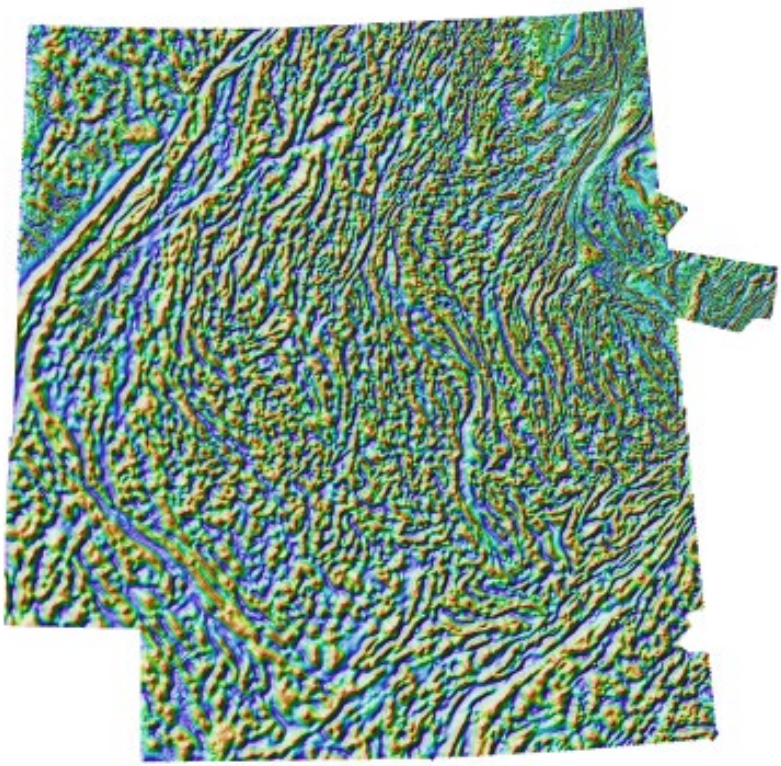

2022_NAB_RMI_RTP_AGC20_HSI_NW

Figure 10: The automatic gain control filter (AGC) is a means of evening out the amplitudes of anomalies. This makes more subtle features in the data visible. The filter also acts as a high-pass filter by suppressing the longer wavelengths.

Magnetic data-processing results images (continued)
▶ Standard filtering — Small-scale residual

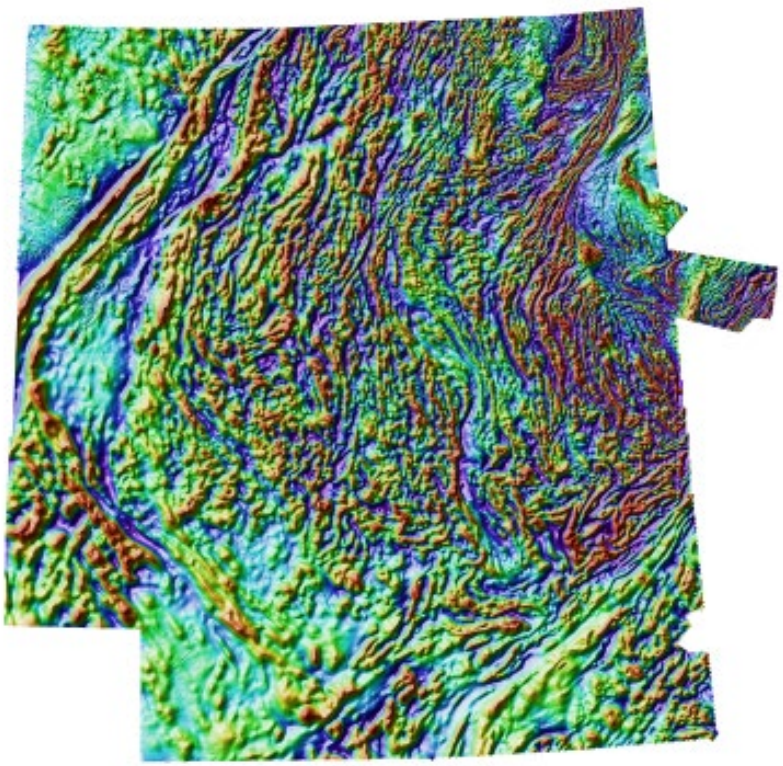

2022_NAB_RMI_RTP_res300_1500_HSI_NW

Figure 11: Differential upward continuation was applied to calculate the 300m-1500m residual of the RTP data in an attempt to separate sources from different depths (Jacobsen, 1987). The source depths should correspond to half of the upward continuation level. For this residual, that would be about 150m-750m depth.

Magnetic data-processing results images (continued)
▶ Standard filtering — Medium-scale residual

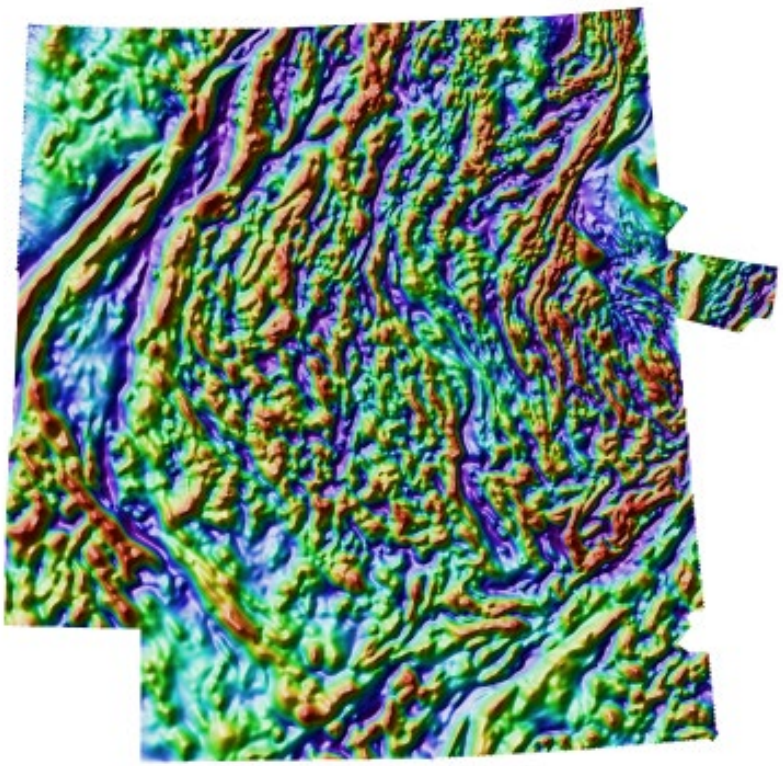

2022_NAB_RMI_RTP_res1500_6000_HSI_NW

Figure 12: Differential upward continuation was applied to calculate the 1500m-6000m residual of the RTP data in an attempt to separate sources from different depths (Jacobsen, 1987). The source depths should correspond to half of the upward continuation level. For this residual, that would be 750m-3000m depth.

Magnetic data-processing results images (continued)
▶ Standard filtering — Large-scale residual

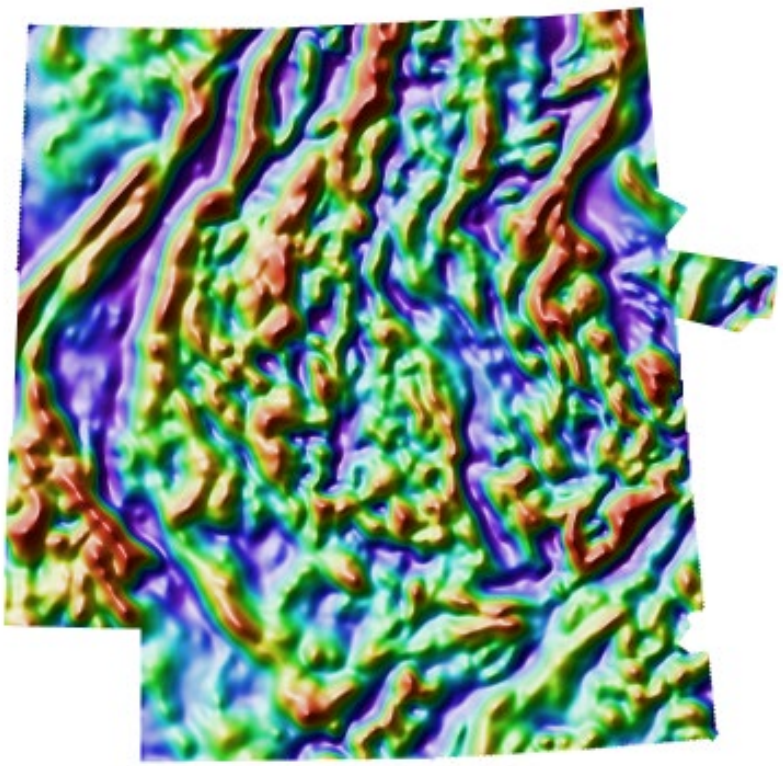

2022_NAB_RMI_RTP_res6000_15000_HSI_NW

Figure 13: Differential upward continuation was applied to calculate the 6000m-15000m residual of the RTP data in an attempt to separate sources from different depths (Jacobsen, 1987). The source depths should correspond to half of the upward continuation level. For this residual, that would be 3000m-7500m depth.

Magnetic data-processing results images (continued)
▶ Standard filtering — Pseudogravity

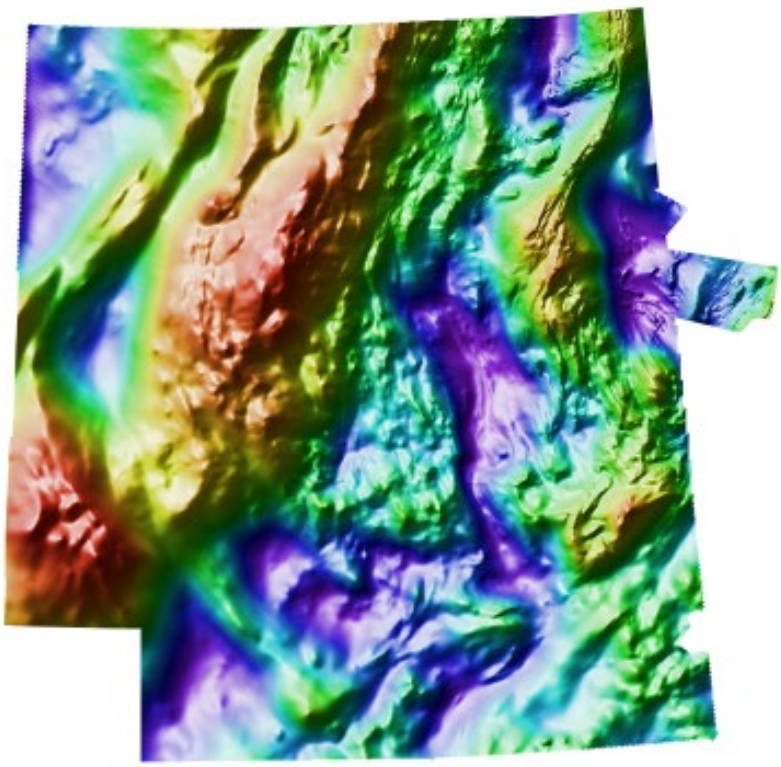

2022_NAB_RMI_RTP_PGrav_HSI_NW

Figure 14: Pseudogravity is generated by calculating the vertical integral of reduced-to-the-pole magnetic data and then using Poisson's relation (correlation between magnetic potential and gravitational potential) to scale the result. This generates a grid that is the expected gravity field if density were distributed in the same way as magnetic susceptibility in the project area. This is not a true gravity grid because it is highly unlikely that susceptibility and density are perfectly correlated. This filter enhances long-wavelength features and is good for highlighting large-scale features.

Magnetic data-processing results images (continued)
▶ Standard filtering — Pseudogravity residual

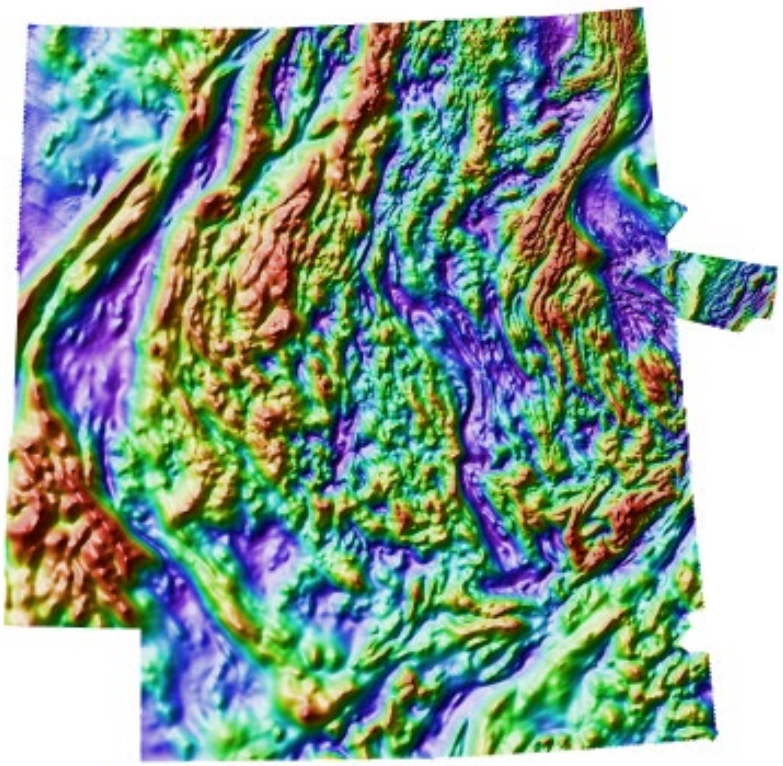

2022_NAB_RMI_RTP_PGravRes_HSI_NW

Figure 15: Differential upward continuation was applied to the pseudogravity grid to generate a 0-2000m residual. This removes the longest wavelength features to allow intermediate-scale features to be seen.

Magnetic data-processing results images (continued)
▶ Standard filtering — HGM of pseudogravity residual

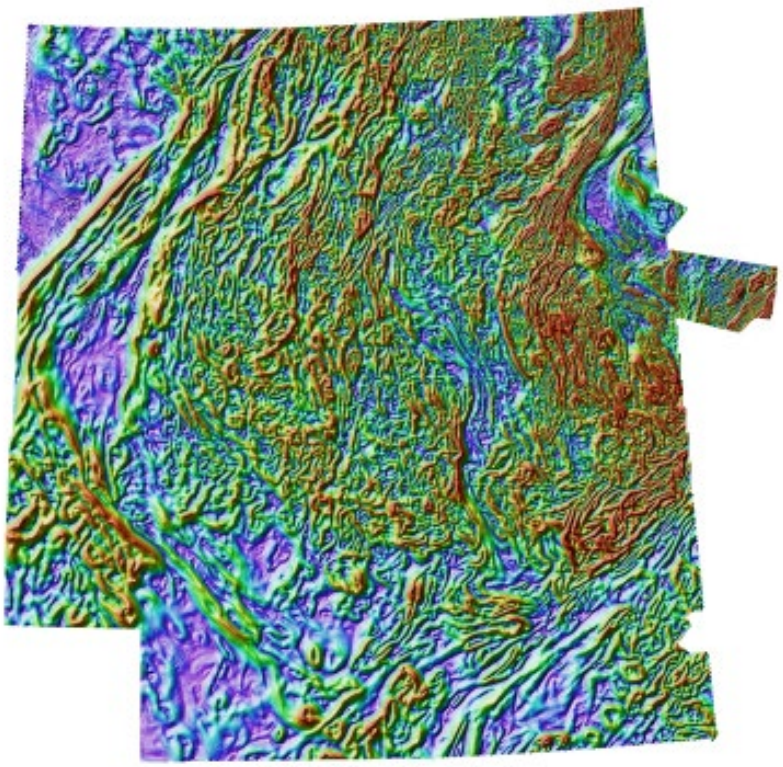

2022_NAB_RMI_RTP_PGravResHGM_HSI_NW

Figure 16: The horizontal gradient was calculated from the pseudogravity residual as described in the caption for **Figure 5**. The results highlight the edges of intermediate-scale features. However, this filter is affected by magnetization direction and remanent magnetization.

Magnetic data-processing results images (continued)
▶ Standard filtering images — Using ternary images

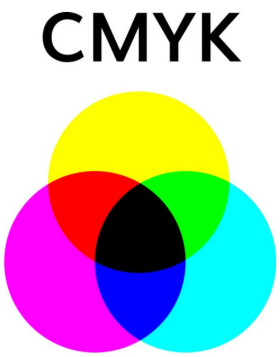

For RGB images:
Green + blue = cyan
Red + blue = magenta
Red + green = yellow
Red + green + blue = white
Low in red + green + blue = black

For CMY images:
Magenta + yellow = red
Cyan + yellow = green
Cyan + magenta = blue
Cyan + magenta + yellow = black
Low in red + green + blue = white

Figure 17: The information above shows how to interpret the colors in the RGB and CMY ternary images appearing in the next few figures, which are:

(i) Ternary of directional derivatives — This image encapsulates information about how steeply the gradient is changing in 3 orthogonal directions, namely the X and Y directions (within the plane of the image), and the Z direction (perpendicular to the plane of the image). All of this gradient information combines to help the observer intuitively identify the various major geological domains residing throughout the area of interest, and how these domains relate to each other.

(ii) Ternary of 1VD, tilt angle, and HGM — This image helps the observer intuitively understand where major structural features are situated, where breaks in the continuity of the magnetic 'fabric' occur, and how the textural character of the magnetic data changes from one locale to the next.

(iii) Ternary of residuals — Again, this image helps the observer intuitively understand where major structural features are situated, where breaks in the continuity of the magnetic 'fabric' occur, and how the textural character of the magnetic data changes from one locale to the next. However, features seen are generally coarser than those appearing in the ternary combining 1VD, tilt and HGM.

(iv) Ternary of RTP, VIAS, and analytic signal — This image helps the observer intuitively understand which subareas may be most affected by remanence (red locales in the CMY image).

(v) Ternary of pseudogravity results — This image combines three pseudogravity-related grids and produces an image that may assist the observer with intuitively grasping the geological affinity of features in the data.

Magnetic data-processing results images (continued)

▶ Standard filtering — Ternary of directional derivatives

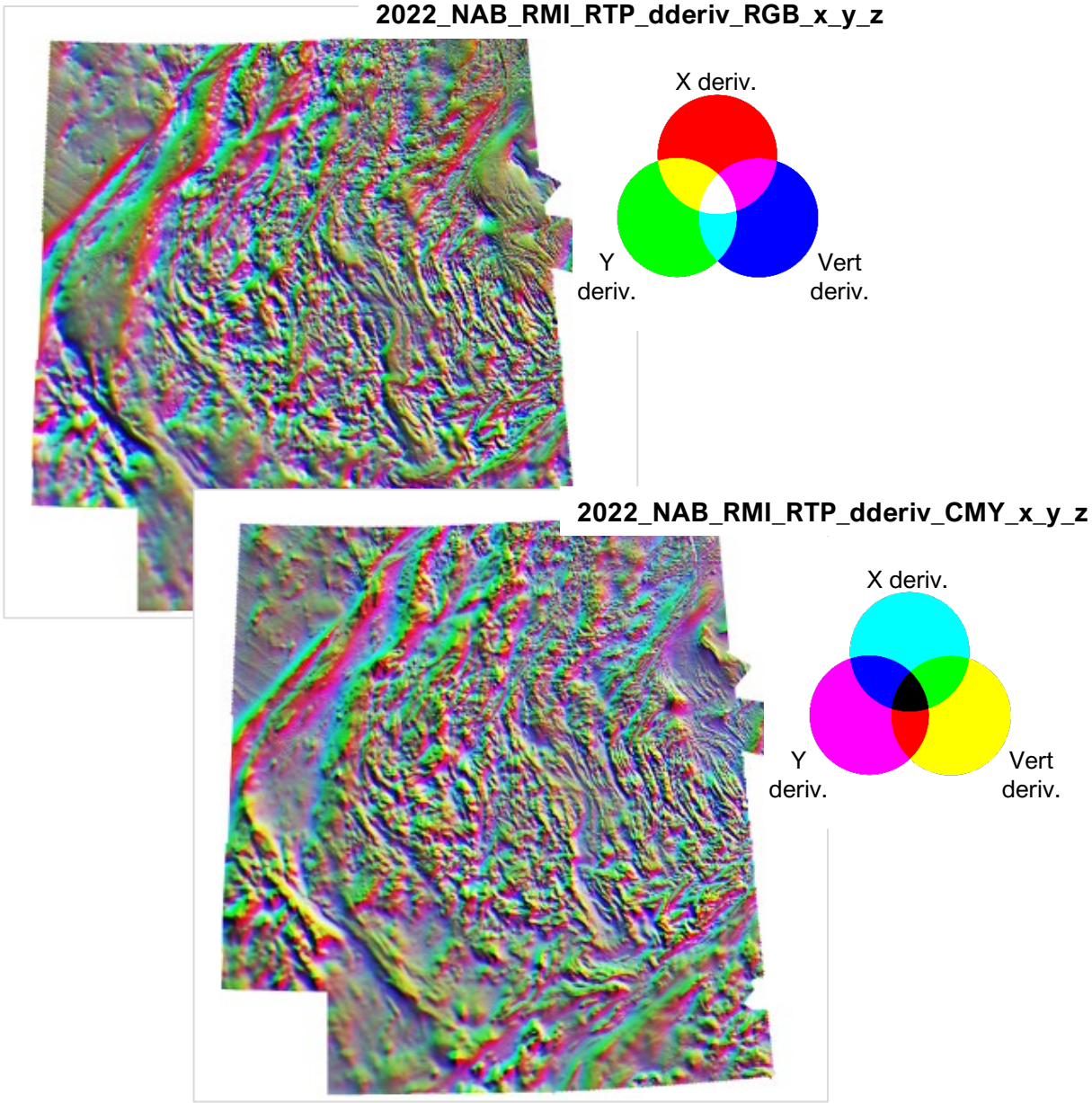

Figure 18: RGB and CMY ternary images co-displaying the X-gradient (R/C channels), Y-gradient (G/M channels), and Z-gradient (i.e., vertical derivative) (B/Y channels).

Magnetic data-processing results images (continued)

▶ Standard filtering — Ternary of 1VD, tilt, HGM

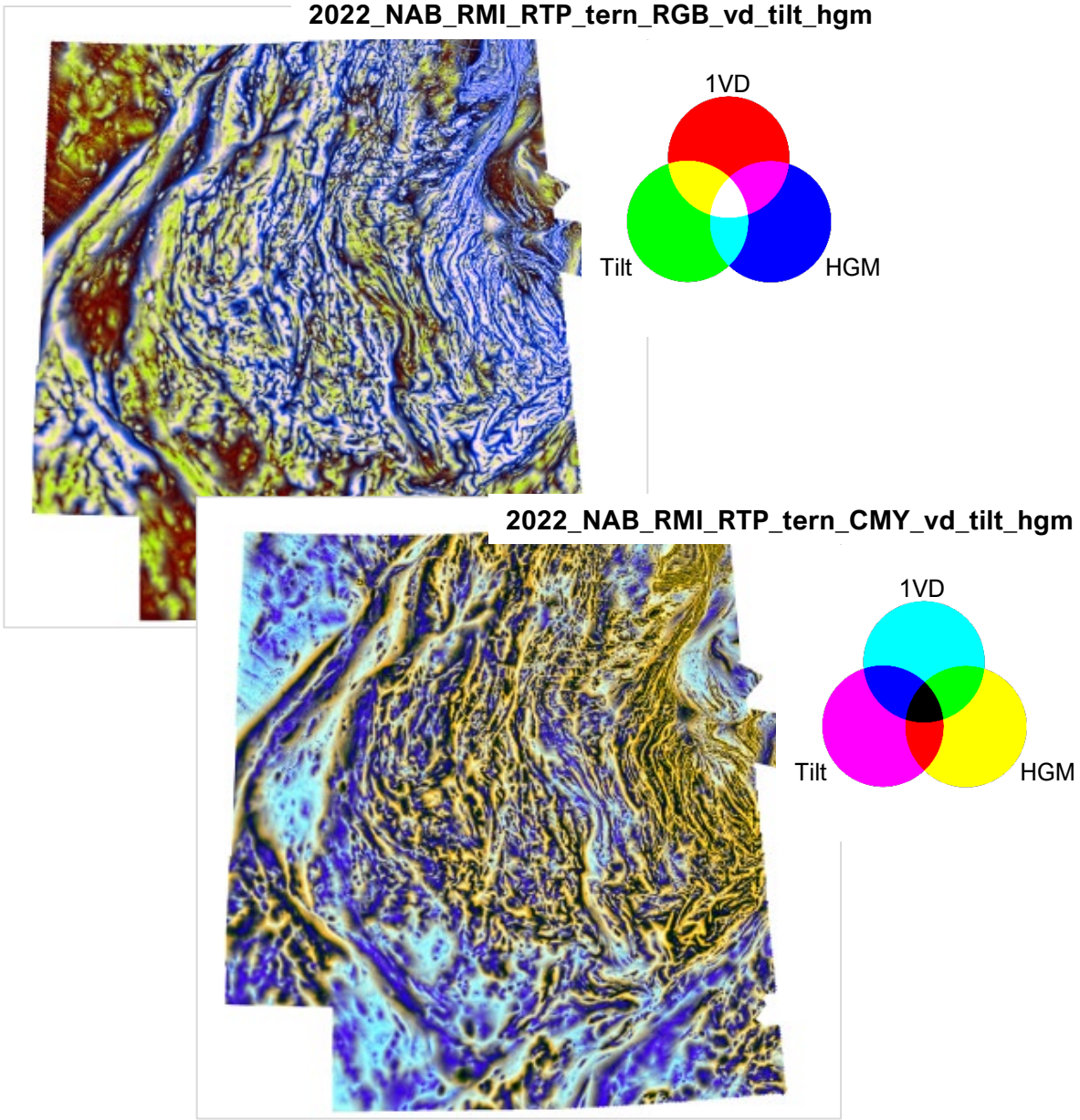

Figure 19: RGB and CMY ternary images co-displaying the vertical derivative (R/C channels), tilt angle (G/M channels), and HGM (B/Y channels).

Magnetic data-processing results images (continued)

▶ Standard filtering — Ternary of residuals

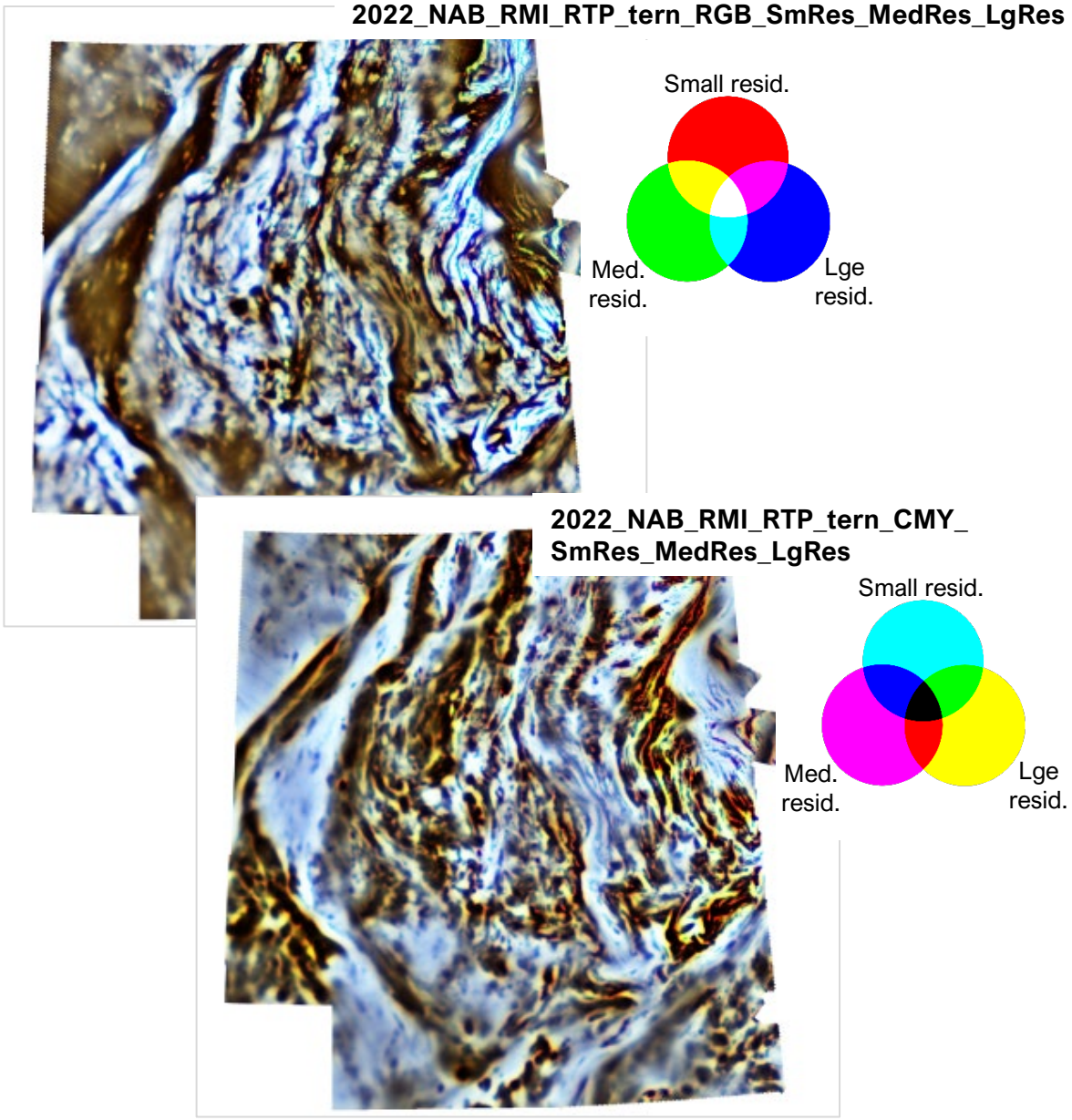

Figure 20: RGB and CMY ternary images co-displaying the small-scale (R/C channels), medium-scale (G/M channels), and large-scale residuals (B/Y channels).

Magnetic data-processing results images (continued)

▶ Standard filtering — Ternary of RTP, VIAS, Asig

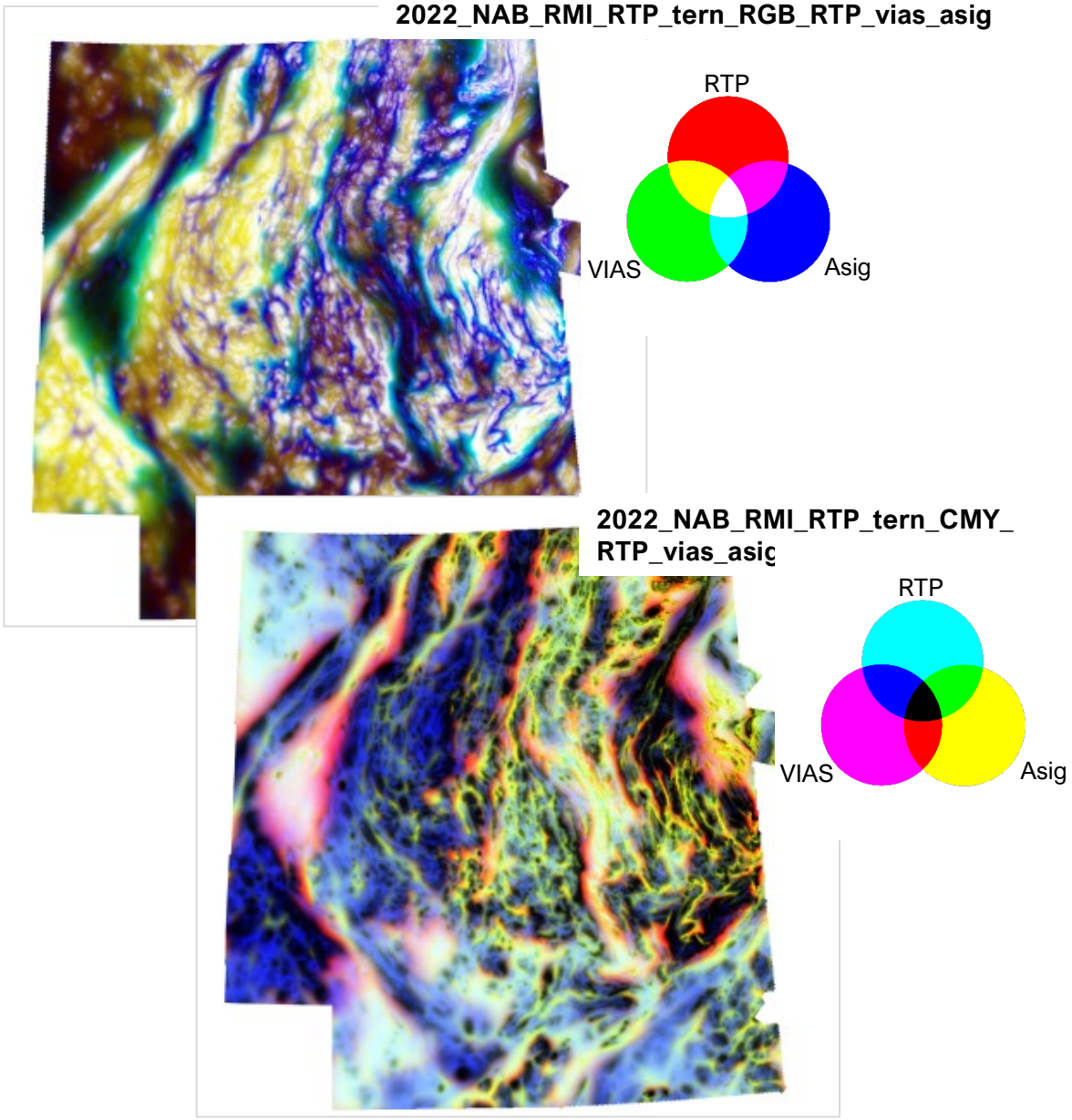

Figure 21: RGB and CMY ternary images co-displaying the RTP (R/C channels), VIAS (G/M channels), and analytic signal (B/Y channels).

Magnetic data-processing results images (continued)

▶ Standard filtering — Ternary of pseudogravity results

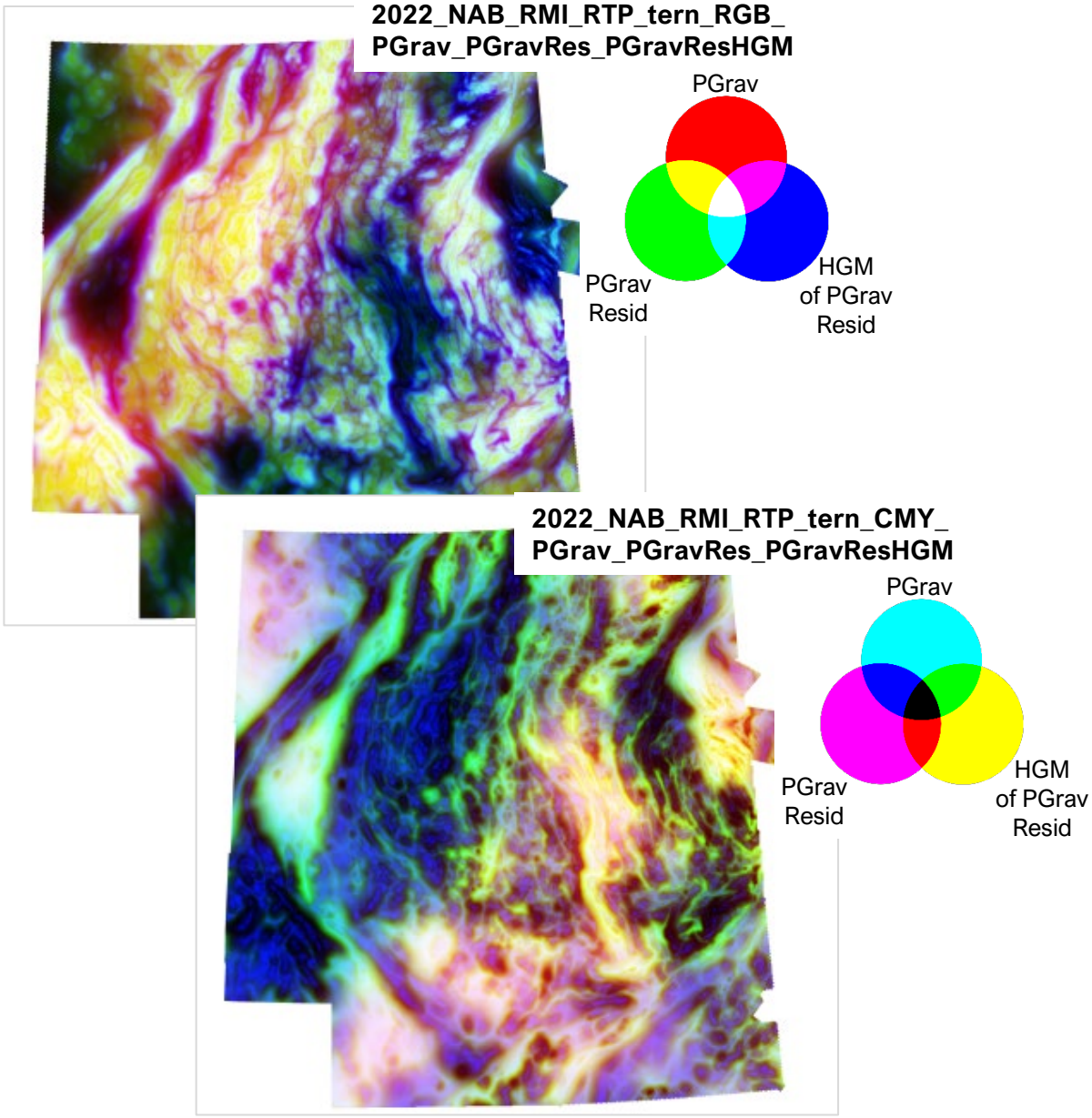

Figure 22: RGB and CMY ternary images co-displaying pseudograv (R/C channels), pseudograv residual (G/M channels), and HGM of pseudograv residual (B/Y channels).

Magnetic data-processing results images (continued)

▶ Total structure detection — Analysis of RTP

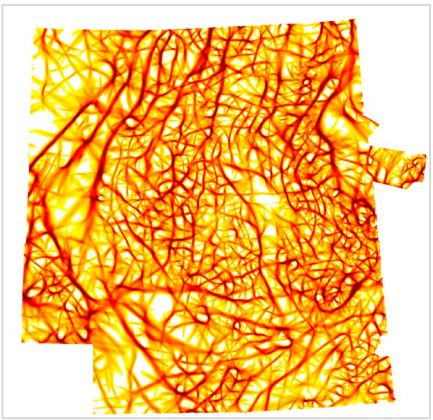

Figure 23: Representative image** showing 3200m structure detection results for the RTP data. TOP: Total structure detected. MIDDLE: Map of thresholded structural orientations. BOTTOM: Total structure in vectorized form (black lines with displayed thickness varying according to median value) over the project area's RTP image.

2022_NAB_RMI_RTP_Struct3200_Total

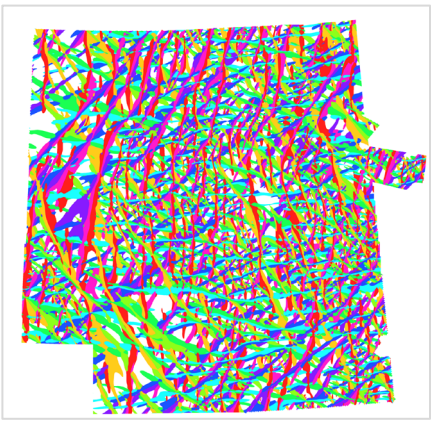

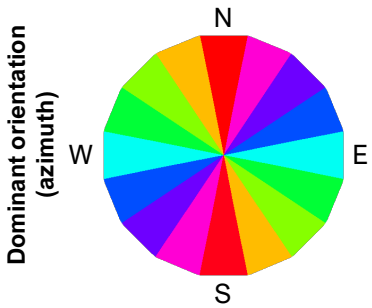

2022_NAB_RMI_RTP_Struct3200_OriDom_Th

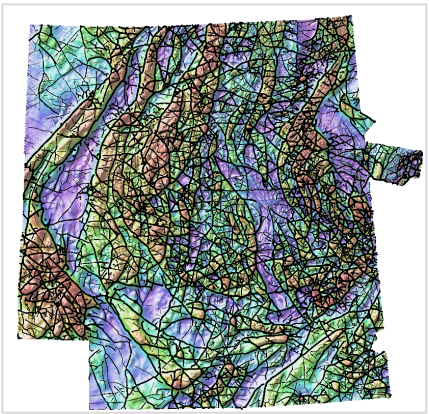

2022_NAB_RMI_RTP_Struct3200_Total_Vec

2022_NAB_RMI_RTP_HSI_NW

** *Further scales of results also delivered.*

Magnetic data-processing results images (continued)
▶ Total structure detection — Analysis of RTP

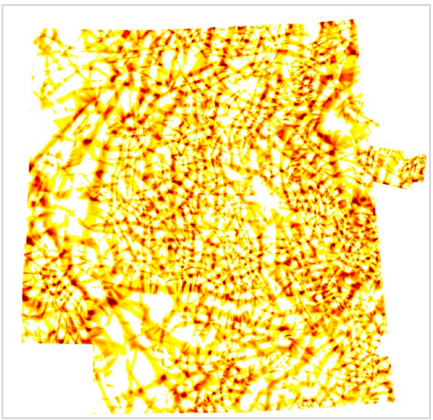

Figure 24: Representative image** showing 3200m structure detection results for the RTP data. TOP: Total structure intersections detected. MIDDLE: Intersections co-displayed with same-scale structures (line color and thickness varies according to structure's median value). BOTTOM: Intersections co-displayed with strong intersections (black-lined polygons) over gray RTP.

2022_NAB_RMI_RTP_Struct3200_Int

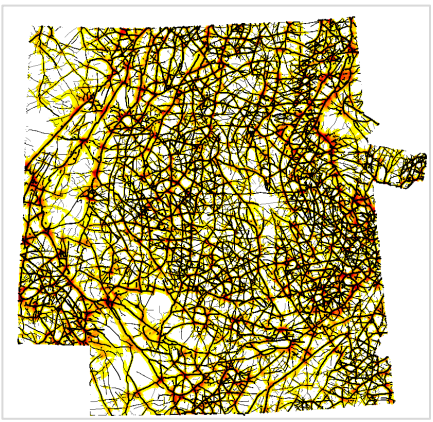

2022_NAB_RMI_RTP_Struct3200_Int

2022_NAB_RMI_RTP_Struct3200_Total_Vec

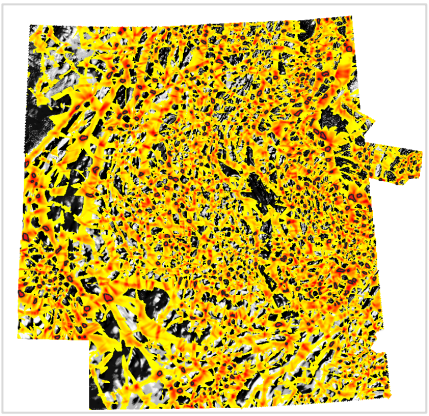

2022_NAB_RMI_RTP_Struct3200_Int

2022_NAB_RMI_RTP_Struct3200_Int_HTh_Vec

2022_NAB_RMI_RTP_HSI_NW (grayscale)

** *Further scales of results also delivered.*

Magnetic data-processing results images (continued)

▶ Total structure detection — Analysis of AGC

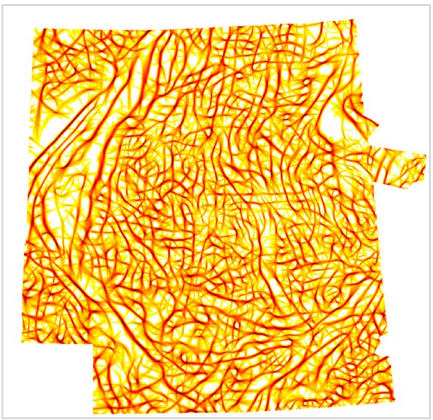

Figure 25: Representative image** showing 3200m structure detection results for the RTP's AGC. TOP: Total structure detected. MIDDLE: Map of thresholded structural orientations. BOTTOM: Total structure in vectorized form (black lines with displayed thickness varying according to median value) over the project area's RTP image.

2022_NAB_RMI_RTP_AGC60_Struct3200_Total

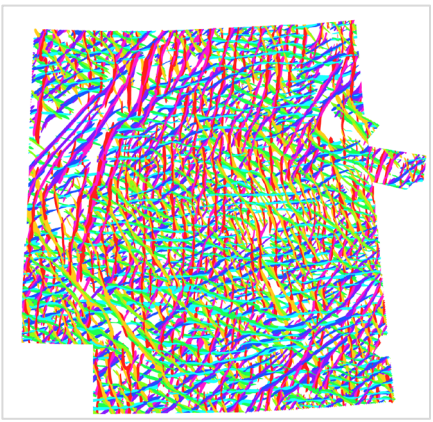

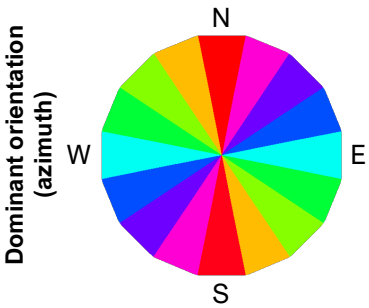

2022_NAB_RMI_RTP_AGC60_Struct3200_OriDom_Th

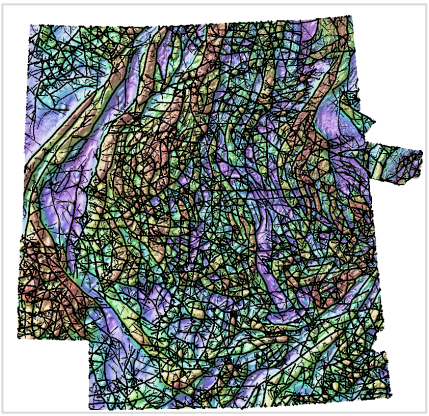

2022_NAB_RMI_RTP_AGC60_Struct3200_Total_Vec

2022_NAB_RMI_RTP_HSI_NW

** *Further scales of results also delivered.*

Magnetic data-processing results images (continued)

▶ Total structure detection — Analysis of AGC

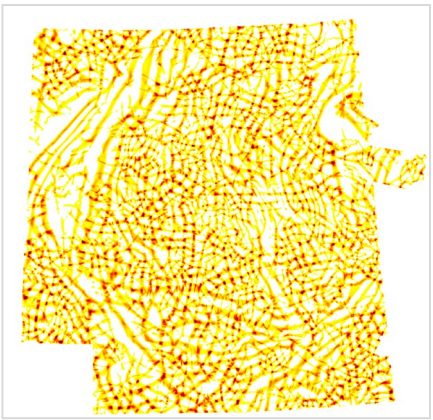

Figure 26: Representative image** showing 3200m structure detection results for the RTP's AGC. TOP: Total structure intersections detected. MIDDLE: Intersections co-displayed with same-scale structures (line color and thickness varies according to structure's median value). BOTTOM: Intersections co-displayed with strong intersections (black-lined polygons) over gray RTP.

2022_NAB_RMI_RTP_AGC60_Struct3200_Int

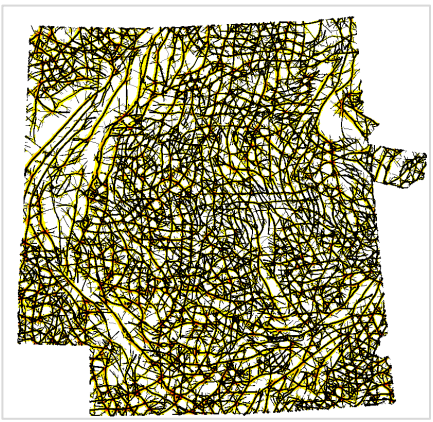

2022_NAB_RMI_RTP_AGC60_Struct3200_Int

2022_NAB_RMI_RTP_AGC60_Struct3200_Total_Vec

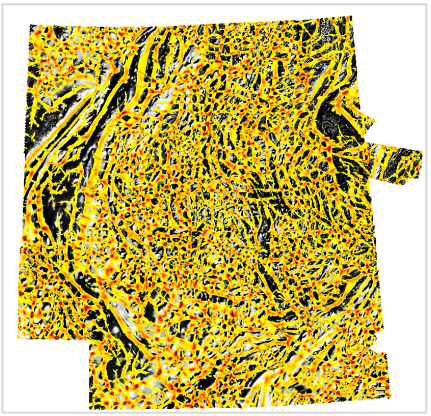

2022_NAB_RMI_RTP_AGC60_Struct3200_Int

2022_NAB_RMI_RTP_AGC60_Struct3200_Int_HTh_Vec

2022_NAB_RMI_RTP_HSI_NW (grayscale)

** *Further scales of results also delivered.*

Magnetic data-processing results images (continued)

▶ Parallel/cross structure — RTP fabric orientation

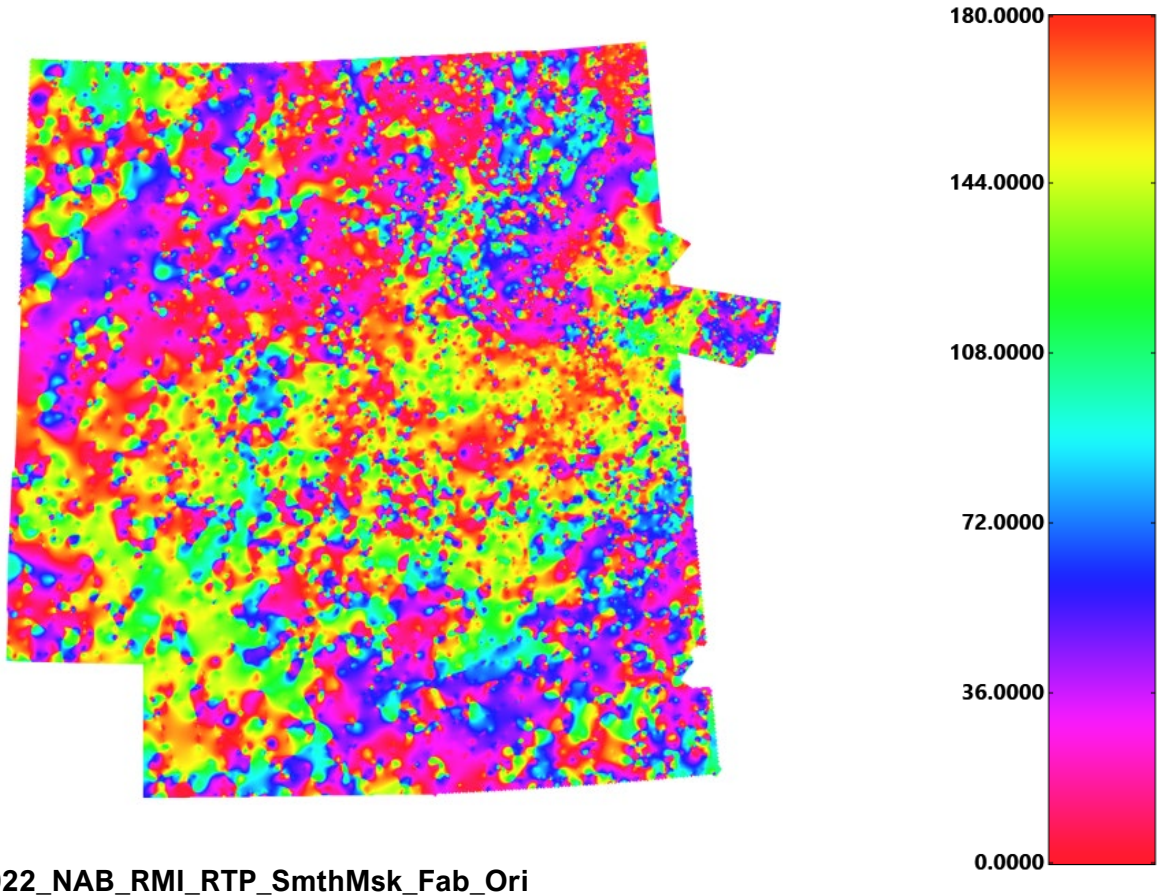

2022_NAB_RMI_RTP_SmthMsk_Fab_Ori

Figure 27: The orientation of magnetic units was determined by taking the AGC of the RTP magnetic data and applying an anisotropic diffusion filter to highlight linear features. Ridge lines were extracted from the enhanced grid and the orientation of the ridge lines was determine. The resulting orientations were interpolated and smoothed to generate the map shown above. The green areas are dominated by WNW to NW trends. The blue and cyan areas are dominated by ENE trends while the magenta indicates NNE trends. The reds and oranges indicate areas that are dominated by NNW to N-trending features. Several distinct zones with relatively coherent orientations are evident in the data. The boundaries between the zones with different orientations are likely either significant faults or large-scale folds.

Magnetic data-processing results images (continued)

▶ Parallel/cross structure — RTP

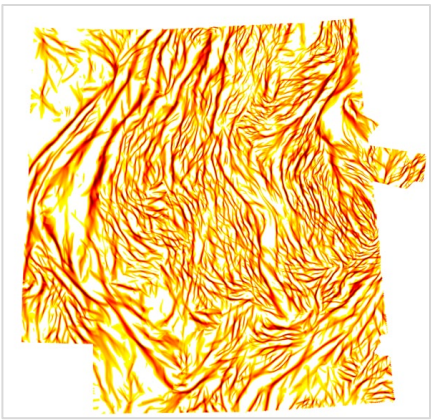

Figure 28: Representative image** showing 1600m belt-parallel structure detection results for the RTP data. TOP: Parallel structures detected. MIDDLE: The same results in vectorized form (displayed line thickness varies according to structure's median value). BOTTOM: Vectorized results co-displayed with the RTP image.

2022_NAB_RMI_RTP_Struct1600_Para

2022_NAB_RMI_RTP_Struct1600_Para_Vec

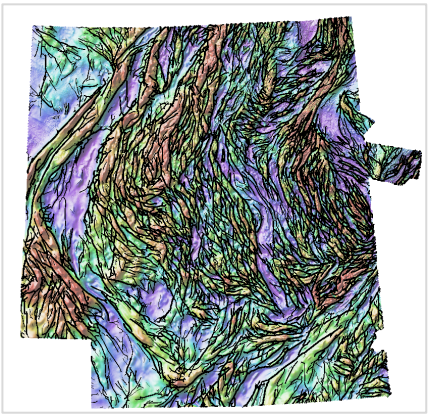

2022_NAB_RMI_RTP_Struct1600_Para_Vec

2022_NAB_RMI_RTP_HSI_NW

** *Further scales of results also delivered.*

Magnetic data-processing results images (continued)

▶ Parallel/cross structure — RTP

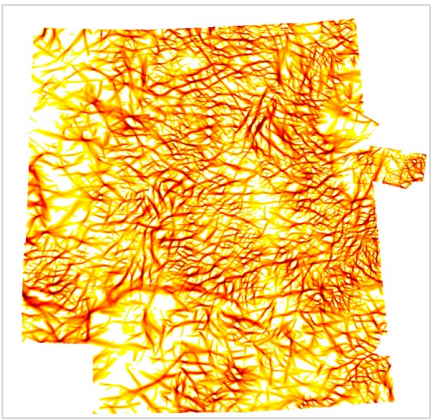

Figure 29: Representative image** showing 1600m belt-crossing structure detection results for the RTP data. TOP: Cross structures detected. MIDDLE: The same results in vectorized form (displayed line thickness varies according to structure's median value). BOTTOM: Vectorized results co-displayed with the RTP image.

2022_NAB_RMI_RTP_Struct1600_Cross

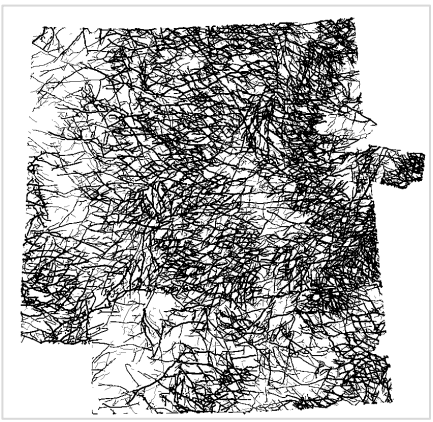

2022_NAB_RMI_RTP_Struct1600_Cross_Vec

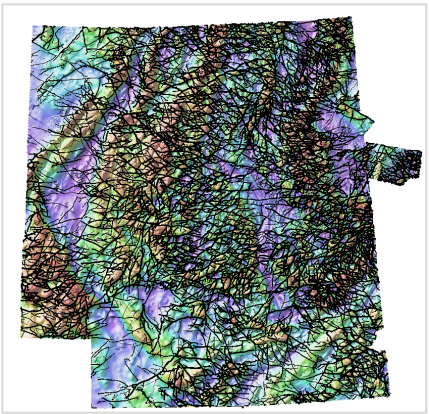

2022_NAB_RMI_RTP_Struct1600_Cross_Vec

2022_NAB_RMI_RTP_HSI_NW

** *Further scales of results also delivered.*

Magnetic data-processing results images (continued)

▶ Parallel/cross structure — AGC

Figure 30: Representative image** showing 1600m belt-parallel structure detection results for the RTP's AGC. TOP: Parallel structures detected. MIDDLE: The same results in vectorized form (displayed line thickness varies according to structure's median value). BOTTOM: Vectorized results co-displayed with the RTP image.

2022_NAB_RMI_RTP_AGC60_Struct1600_Para

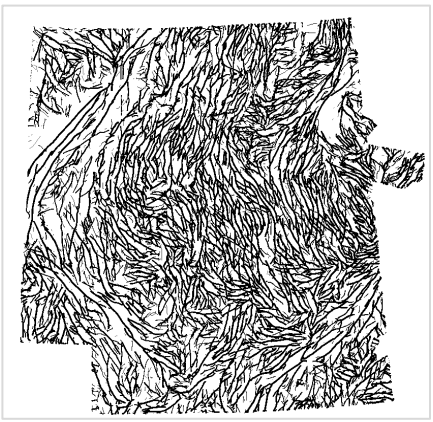

2022_NAB_RMI_RTP_AGC60_Struct1600_Para_Vec

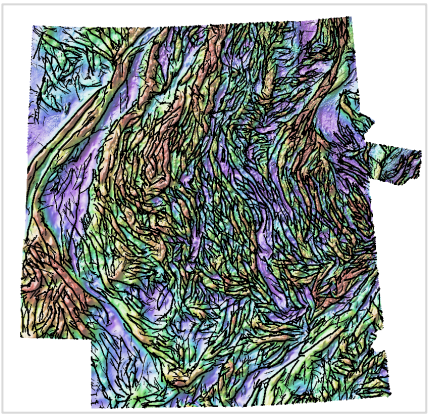

2022_NAB_RMI_RTP_AGC60_Struct1600_Para_Vec

2022_NAB_RMI_RTP_HSI_NW

** *Further scales of results also delivered.*

Magnetic data-processing results images (continued)

▶ Parallel/cross structure — AGC

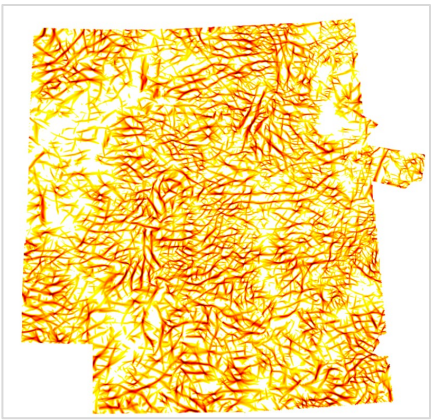

Figure 31: Representative image** showing 1600m belt-crossing structure detection results for the RTP's AGC. TOP: Cross structures detected. MIDDLE: The same results in vectorized form (displayed line thickness varies according to structure's median value). BOTTOM: Vectorized results co-displayed with the RTP image.

2022_NAB_RMI_RTP_AGC60_Struct1600_Cross

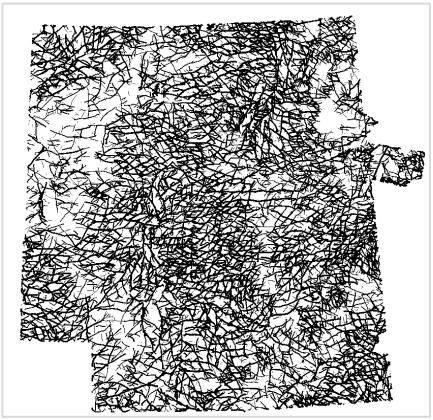

2022_NAB_RMI_RTP_AGC60_Struct1600_Cross_Vec

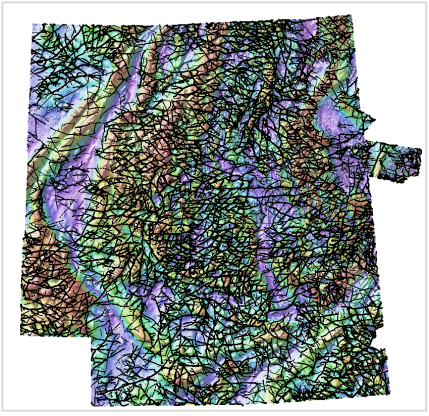

2022_NAB_RMI_RTP_AGC60_Struct1600_Cross_Vec

2022_NAB_RMI_RTP_HSI_NW

** *Further scales of results also delivered.*

Magnetic data-processing results images (continued)

▶ Radial symmetry analysis — RTP

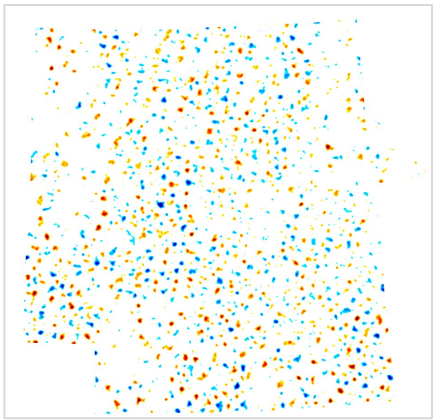

Figure 32: Representative image** showing 4000m magnitude-independent radial symmetry results for the RTP data. TOP: Radially symmetric features detected (both positive and negative anomalies). MIDDLE: Vectorized polygons representing strong anomalies obtained via thresholding. BOTTOM: Polygons co-displayed with the RTP image.

2022_NAB_RMI_RTP_res1000_16000_RSym4000_mi_Highs_and_Lows

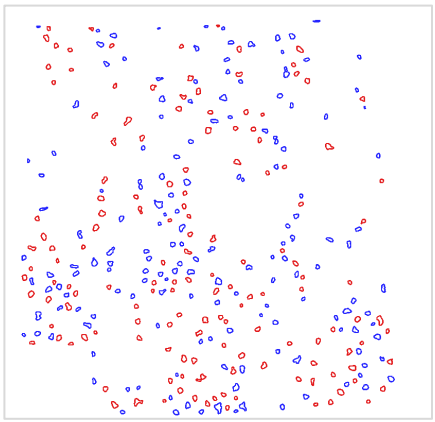

2022_NAB_RMI_RTP_res1000_16000_RSym4000_mi_HTh_Vec_High

2022_NAB_RMI_RTP_res1000_16000_RSym4000_mi_HTh_Vec_Low

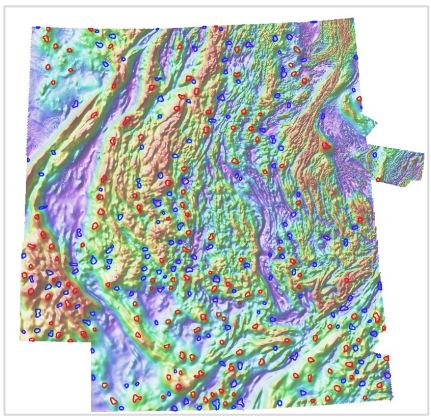

2022_NAB_RMI_RTP_res1000_16000_RSym4000_mi_HTh_Vec_High

2022_NAB_RMI_RTP_res1000_16000_RSym4000_mi_HTh_Vec_Low

2022_NAB_RMI_RTP_HSI_NW

** *Further scales of results also delivered.*

Magnetic data-processing results images (continued)

▶ Depth to basement — Depth

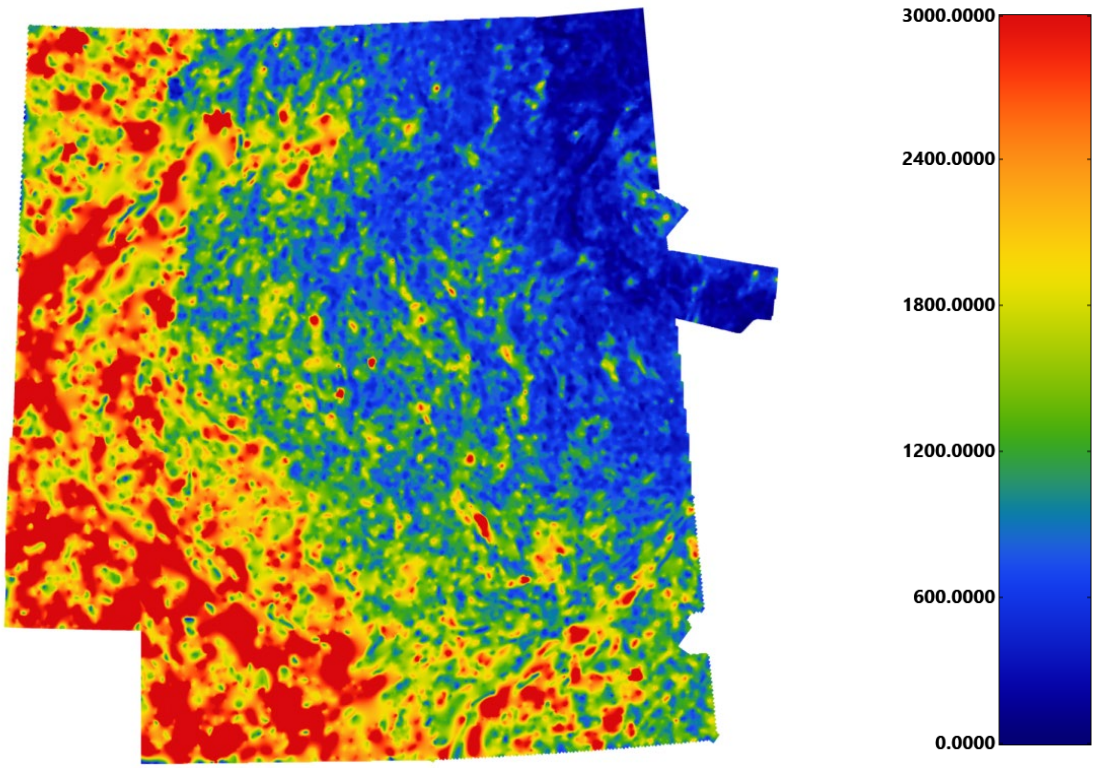

2022_NAB_RMI_RTP_Depth_to_Magnetic_Source

Figure 33: The depth to magnetic source results are shown colored according to the color bar on the right. The units are in meters below the topographic surface. The depths increase to the west with the magnetic rocks being buried by more than 3km in the areas with the most cover. The least cover is in the northeast where it appears the basement rocks are outcropping.

Magnetic data-processing results images (continued)

▶ Depth to basement — Surface elevation

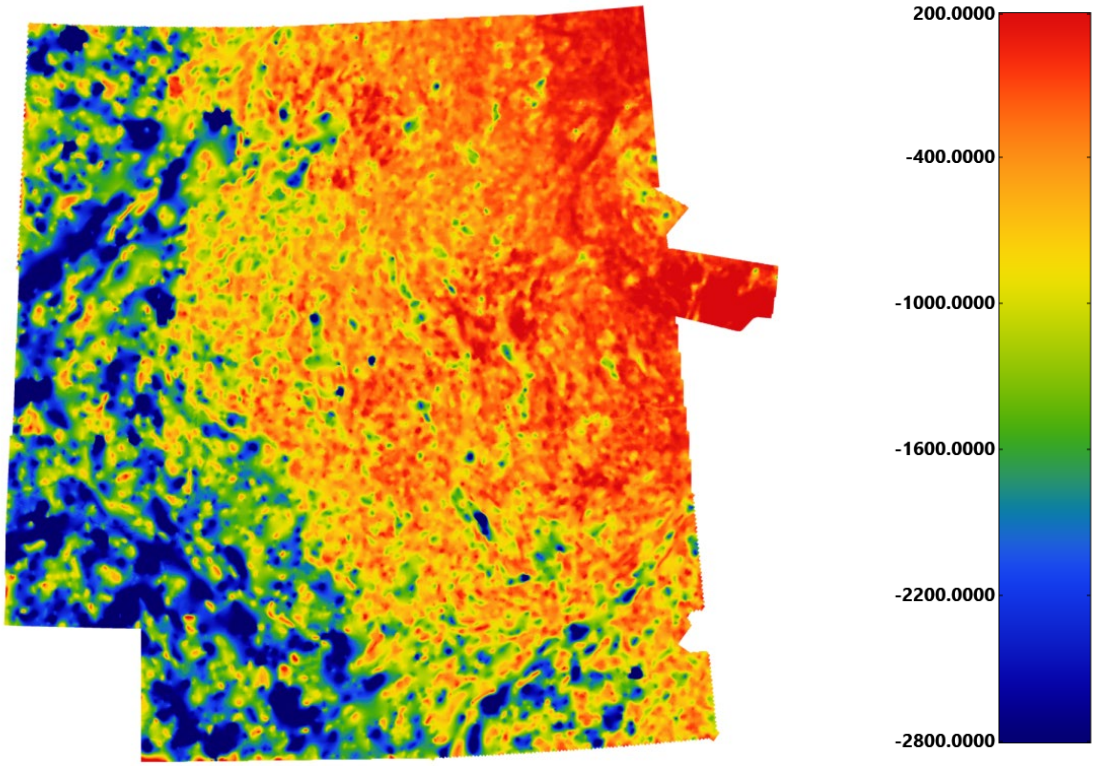

2022_NAB_RMI_RTP_Magnetic_Basement_Surface

Figure 34: The elevation of the magnetic basement surface is shown colored as indicated by the color bar to the right of the image. The grid is basically the inverse of the depth to source grid with the magnetic rocks outcropping in the northeast and getting down to and RL below -2800 in parts of the west.

Appendix 1: Structure detection algorithm

The goal in developing structure detection was to move towards automated interpretation of potential field data that would be most similar to an interpretation by a person. The structure detection is a phase congruency algorithm based on oriented exponential filters (**Kovesi, 1999**).

The structure detection filter is a feature detection algorithm used to highlight ridges, valleys or edges in gridded data. The results are significantly different from other feature detection routines.

Perhaps the biggest difference is that the results are a measure of symmetry or asymmetry, irrespective of amplitude. This is because the analysis is completed using the local phase rather than the signal amplitude.

This means that features in areas of low contrast are highlighted just as well as those in areas of high contrast, as long as the frequencies are present. High values in the structure grid indicate that the structure is close to a step edge. A small step change will have a higher value than a higher amplitude change that is more gradual.

The method is also multi-scale by design. For structures to be highlighted, they must be present at more than one scale. This eliminates more-minor edges that may be present over a narrow frequency range.

The use of exponential filters to determine the scale allows for some inference as to the depth of the structures detected when the filter is applied to potential field data. The wavelength in the filename is the shallowest upward continuation level used and the approximate depth should range between 0.5 and 1 times this wavelength.

This depth estimate is based on **Jacobsen (1987)**. This method is not perfect at separating sources from different depths. It is possible to generate long-wavelength features from shallow sources as evidenced by the fact that there are long wavelength features present in radiometric data, which do not have a significant depth component. However, the method should provide a good first pass estimate of which features extend to depth and which are only surficial. It is possible for deep tapping structures to be missed if there is not a significant property contrast across them.

Appendix 1: Structure detection algorithm (continued)

The structure detection filter produces orientation grids that show the orientation of the strongest edge at a given location. When these orientation grids have been thresholded to remove low amplitude features, it's easier to see the prominent structural orientations.

References

Kovesi, P., 1999, Image Features From Phase Congruency. Videre: A Journal of Computer Vision Research, v. 1, no. 3.

Jacobsen, B.H., 1987, A case for upward continuation as a standard separation filter for potential-field maps. Geophysics, v.52, no. 8, pp. 1138-1148.

Appendix 2: Radial symmetry algorithm

The goal in developing the radial symmetry filter is a move towards automated interpretation of potential field and topographic data that would be most similar to an interpretation by a person.

The filter highlights round features (as opposed to linear features) in the data. This allows us to locate areas that have a higher likelihood of being intrusive bodies or discrete alteration zones.

We have developed several radial symmetry filters. The filter that was used for this project is a gradient-based filter that looks for points where the grid slopes away in all directions. Detected locations are magnetic highs that are discrete bodies. Discrete magnetic lows are areas where the grid slopes toward the location from all directions. This algorithm is based on **Loy and Zelinsky (2002)**.

The filter can be used in a magnitude independent (MI) or magnitude dependent (MD) mode. The MI measure is a strict measure of radial symmetry, making it a direct measure of how round an anomaly is, irrespective of the magnitude of the gradients involved there. The MD measure is the MI measure scaled according to the magnitude of the gradients in the grid.

The filter looks for features with a radius between a base radius and two times that radius. It will not locate features that are significantly smaller than the range used. The filter will highlight the center of some features that are larger than the radius range.

References

Loy G., Zelinsky A., 2002, A Fast Radial Symmetry Transform for Detecting Points of Interest. In: Heyden A., Sparr G., Nielsen M., Johansen P. (eds) Computer Vision — ECCV 2002. ECCV 2002. Lecture Notes in Computer Science, vol 2350. Springer, Berlin, Heidelberg